TECHNISCHE UNIVERSITÄT MÜNCHEN

Fakultät für Medizin

Diffusion-Weighted Magnetic Resonance Techniques for Probing the Microstructure of Fat-Containing Tissues

Dominik Johannes Weidlich

Vollständiger Abdruck der von der Fakultät für Medizin der Technischen Universität München zur Erlangung des akademischen Grades eines

Doktors der Naturwissenschaften (Dr. rer. nat.)

genehmigten Dissertation.

Vorsitz: Prof. Dr. Gabriele Multhoff
Prüfer der Dissertation: 1. Prof. Dr. Dimitrios Karampinos
2. Prof. Dr. Björn Menze
3. Prof. Dr. Frederik B. Laun

Die Dissertation wurde am 16.11.2021 bei der Technischen Universität München eingereicht und durch die Fakultät für Medizin am 09.08.2022 angenommen.

Abstract

The characterization of tissue microstructure can reveal important information about disease status, progression and response to treatment. In the context of metabolic dysfunction, the assessment of adipose tissue cell size has been receiving increasing excitement. In obesity, the fat cell (adipocyte) size can increase severely when more lipids need to be stored in the human body. Patients with hypertrophic fat cells show a high prevalence of inflammatory processes in the adipose tissue and ectopic accumulation of fat. In type 2 diabetes, there is growing evidence that adipocyte size correlates with insulin sensitivity. Up to now the measurement of adipocyte size requires highly invasive biopsy procedures which are not compatible with screening protocols. An in vivo assessment of adipocyte size could serve as a potential early biomarker and target for therapy monitoring in patients with metabolic dysfunction.

Diffusion-weighted (DW) magnetic resonance (MR) is a powerful tool for the non-invasive assessment of tissue microstructure. Probing diffusion restriction effects allows the extraction of quantitative information like the estimation of mean restriction barrier sizes. The technique has been successfully applied in water-containing tissues and in small lipid droplets like in intramyocellular lipids and brown adipocytes. Measuring diffusion restriction effects in fat-containing tissues is challenging because fat has a diffusion coefficient approximately two orders of magnitude lower than water. The DW information can be obtained by DW-MR spectroscopy (MRS), which offers spectrally resolved information with only very limited spatial information. In contrast to that, DW MR imaging (MRI) aims at retrieving spatially resolved data but with limited information in the chemical shift dimension. Both techniques can be applied to acquire DW-MR data which can be used to retrieve microstructural information in a subsequent modeling step. Up to now, measuring adipocyte size with MR is limited to small adipocytes and has been performed using pre-clinical MR scanners with a strong gradient system.

The present cumulative thesis bundles three journal publications in the field of lipid DW MR aiming a) to show for the first time that it is feasible to measure lipid droplet size in large droplets using the gradient hardware of a clinical MR scanner based on DW-MRS sequence, b) to propose a method to reduce the effect of vibrational artifacts induced by the high b-values employed in lipid DW and c) to measure spatially resolved lipid droplet size maps based on a DW-MRI sequence.

In the first journal publication, it was shown for the first time that adipocyte size measurements are feasible using a clinical MR scanner in also adipocytes larger than a few micrometer in size. A DW-MRS sequence was employed in order to acquire spectroscopically resolved data with strong DW and long diffusion times. The obtained signal was subsequently fitted by an equation describing the signal evolution when the diffusion of particles is restricted. The presented methodology was validated in water-fat emulsion phantoms and applied in vivo to obtain the mean adipocyte size in the tibia bone marrow.

The second journal publication proposes a novel gradient pre-pulse applied before the DW module, called vibration matching gradient (VMG) in high b-value lipid DW measurements. The additional gradient aims to harmonize the vibration patterns during both DW time periods resulting in reduced artifacts. The proposed methodology was investigated by simulations

of a simplified mechanical model and validated by laser interferometer measurements of the actual displacements during a DW-MRS acquisition. The proposed method was found to give more accurate and robust diffusion constant quantifications in water-fat emulsion phantoms and in vivo in the bone marrow of the tibia.

Finally, the third journal publication presents a novel pulse sequence and modeling paradigm to extract spatially resolved adipocyte size maps. The presented method was again validated in water-fat emulsions and then applied in ex vivo human adipose tissue samples. The obtained values from the specimen study where compared to histology and a good agreement between the measurements was found.

All developed techniques were and are being used in ongoing research investigations in the field of metabolic dysfunction.

List of Included Journal Publications

The present dissertation is based on the following three journal publications:

JP-I **D. Weidlich**, J. Honecker, O. Gmach, M. Wu, R. Burgkart, S. Ruschke, D. Franz, B. H. Menze, T. Skurk, H. Hauner, U. Kulozik, and D. C. Karampinos, *"Measuring large lipid droplet sizes by probing restricted lipid diffusion effects with diffusion-weighted MRS at 3T"*, Magn Reson Med, vol. 81, no. 6, pp. 3427–3439, June 2019. DOI: 10.1002/mrm.27651

JP-II **D. Weidlich**, M. Zamskiy, M. Maeder, S. Ruschke, S. Marburg, and D. C. Karampinos, *"Reduction of vibration-induced signal loss by matching mechanical vibrational states: Application in high b-value diffusion-weighted MRS"*, Magn Reson Med, vol. 84, no. 1, pp. 39–51, Jul. 2020. DOI: 10.1002/mrm.28128.

JP-III **D. Weidlich**, J. Honecker, C. Boehm, S. Ruschke, D. Junker, A. T. Van, M. R. Makowski, C. Holzapfel, M. Claussnitzer, H. Hauner and D. C. Karampinos, *"Lipid droplet size mapping in human adipose tissue using a clinical 3 T system"*, Magn Reson Med, vol. 86, no. 3, pp. 1256– 1270, April. 2021. DOI: 10.1002/mrm.28755.

The above three journal publications are referred to as JP-I, JP-II and JP-III, respectively. Please refer to Chapter 6 for publication abstracts.

List of Related Publications

The author contributed also to the following subject-related journal publications (ordered by year of appearance):

J1 J. Honecker, **D. Weidlich**, S. Heisz, C.M. Lindgren, D.C. Karampinos, M. Claussnitzer, H. Hauner, "A distribution-centered approach for analyzing human adipocyte size estimates and their association with obesity-related traits and mitochondrial function", International Journal of Obesity 45, 2108–2117. (2021)

J2 P. Giesler, F.A. Baumann, **D. Weidlich**, D.C. Karampinos, M. Jung, C. Holwein, J. Schneider, A.S. Gersing, A.B. Imhoff, F. Bamberg, P.M. Jungmann, "Patellar instability MRI measurements are associated with knee joint degeneration after reconstruction of the medial patellofemoral ligament", Skeletal Radiology epub. (2021)

J3 M. Probst, E. Burian, T. Robl, **D. Weidlich**, D.C. Karampinos, T. Brunner, C. Zimmer, F.A. Probst, M. Folwaczny, "Magnetic Resonance Imaging as a Diagnostic Tool for Periodontal Disease: a prospective study with correlation to standard clinical findings – is there added value?", Journal of Clinical Periodontology 7, 929–948. (2021)

J4 N. Sollmann, P. Schandelmaier, **D. Weidlich**, C. Börner, G. Urban, M. Lang, C. Zimmer, D.C. Karampinos, M.N. Landgraf, F. Heinen, T. Baum, M.V. Bonfert, "Patients with episodic migraine show increased T2 values of the trapezius muscles – an investigation by quantitative high-resolution magnetic resonance imaging", Cephalalgia 8, 934–942. (2021)

J5 S. Schlaeger, N. Sollmann, A. Zoffl, E.A. Becherucci, **D. Weidlich**, E. Kottmaier, I. Riederer, T. Greve, F. Montagnese, M. Deschauer, B. Schoser, C. Zimmer, D.C. Karampinos, J.S. Kirschke, T. Baum, "Quantitative Muscle MRI in Patients with Neuromuscular Diseases—Association of Muscle Proton Density Fat Fraction with Semi-Quantitative Grading of Fatty Infiltration and Muscle Strength at the Thigh Region", Diagnostics 11, 1056. (2021)

J6 T. Greve, E. Burian, A. Zoffl, G. Feuerriegel, S. Schlaeger, M. Dieckmeyer, N. Sollmann, E. Klupp, **D. Weidlich**, S. Inhuber, M. Loeffler, F. Montagnese, M. Deschauer, B. Schoser, S. Bublitz, C. Zimmer, D.C. Karampinos, J.S. Kirschke, T. Baum, Regional variation of thigh muscle fat infiltration in patients with neuromuscular diseases compared to healthy controls. Quantitative Imaging in Medicine and Surgery 11, 2610–2621. (2021)

J7 M. Dieckmeyer, S. Inhuber, S. Schlaeger, **D. Weidlich**, M.R.K. Mookiah, K. Subburaj, E. Burian, N. Sollmann, J.S. Kirschke, D.C. Karampinos, T. Baum, "Association of Thigh Muscle Strength with Texture Features Based on Proton Density Fat Fraction Maps Derived from Chemical Shift Encoding-Based Water–Fat MRI", Diagnostics 11, 302. (2021)

J8 M. Dieckmeyer, S. Inhuber, S. Schlaeger, **D. Weidlich**, M.R.K. Mookiah, K. Subburaj, E. Burian, N. Sollmann, J.S. Kirschke, D.C. Karampinos, T. Baum, "Texture Features of Proton Density Fat Fraction Maps from Chemical Shift Encoding-Based MRI Predict Paraspinal Muscle Strength". Diagnostics 11, 239. (2021)

J9 D. Junker, J. Syvaeri, **D. Weidlich**, C. Holzapfel, T. Drabsch, B. Waschulzik, E.J. Rummeny, H. Hauner, D.C. Karampinos, "Investigation of the Relationship between MR-Based Supraclavicular Fat Fraction and Thyroid Hormones", Obesity Facts 1–13. (2020)

J10 N. Sollmann, **D. Weidlich**, E. Klupp, B. Cervantes, C. Ganter, C. Zimmer, E.J. Rummeny, T. Baum, J.S. Kirschke, D.C. Karampinos, "T2 mapping of the distal sciatic nerve in healthy subjects and patients suffering from lumbar disc herniation with nerve compression". Magnetic Resonance Materials in Physics, Biology and Medicine 33, 713–724. (2020)

J11 N. Sollmann, B. Cervantes, E. Klupp, **D. Weidlich**, M.R. Makowksi, J.S. Kirschke, H.H Hu, D.C. Karampinos, "Magnetic resonance neurography of the lumbosacral plexus at 3 Tesla – CSF-suppressed imaging with submillimeter resolution by a three-dimensional turbo spin echo sequence", Magnetic Resonance Imaging 71, 132–139. (2020)

J12 A.S. Gersing, B. Cervantes, C. Knebel, B.J. Schwaiger, J.S. Kirschke, **D. Weidlich**, C. Claudi, J.M. Peeters, D. Pfeiffer, E.J. Rummeny, D.C. Karampinos, K. Woertler, "Diffusion tensor imaging and tractography for preoperative assessment of benign peripheral nerve sheath tumors", European Journal of Radiology 129, 109110. (2020)

J13 S. Schlaeger, **D. Weidlich**, E. Klupp, F. Montagnese, M. Deschauer, B. Schoser, S. Bublitz, S. Ruschke, C. Zimmer, E.J. Rummeny, J.S. Kirschke, D.C. Karampinos, "Water T2 Mapping in Fatty Infiltrated Thigh Muscles of Patients With Neuromuscular Diseases Using a T2-Prepared 3D Turbo Spin Echo With SPAIR", Journal of Magnetic Resonance Imaging 51, 1727–1736. (2020)

J14 E. Burian, S. Inhuber, S. Schlaeger, M. Dieckmeyer, E. Klupp, D. Franz, **D. Weidlich**, N. Sollmann, M. Loeffler, A. Schwirtz, E.J. Rummeny, C. Zimmer, J.S. Kirschke, D.C. Karampinos, T. Baum, "Association of thigh and paraspinal muscle composition in young adults using chemical shift encoding-based water–fat MRI", Quantitative Imaging in Medicine and Surgery 10, 128–136. (2020)

J15 E. Klupp, B. Cervantes, N. Sollmann, F. Treibel, **D. Weidlich**, T. Baum, E.J. Rummeny, C. Zimmer, J.S. Kirschke, D.C. Karampinos, "Improved Brachial Plexus Visualization Using an Adiabatic iMSDE-Prepared STIR 3D TSE", Clinical Neuroradiology 29, 631–638. (2019)

J16 E. Burian, F.A. Probst, **D. Weidlich**, C.P. Cornelius, L. Maier, T. Robl, C. Zimmer, D.C. Karampinos, L.M. Ritschl, M. Probst, "MRI of the inferior alveolar nerve and lingual nerve—anatomical variation and morphometric benchmark values of nerve diameters in healthy subjects". Clinical Oral Investigations 24, 1-10. (2019)

J17 E. Burian, A. Rohrmeier, S. Schlaeger, M. Dieckmeyer, M.N. Diefenbach, J. Syvaeri, E. Klupp, **D. Weidlich**, C. Zimmer, E.J. Rummeny, D.C. Karampinos, J.S. Kirschke, T.

Baum, "Lumbar muscle and vertebral bodies segmentation of chemical shift encoding-based water-fat MRI: the reference database MyoSegmenTUM spine", BMC Musculoskeletal Disorders 20, 152. (2019)

J18 L. Schlaffke, R. Rehmann, M. Rohm, L.A.M. Otto, A. Luca, J. Burakiewicz, C. Baligand, J. Monte, C. Harder, M.T. Hooijmans, A. Nederveen, S. Schlaeger, **D. Weidlich**, D.C. Karampinos, A. Stouge, M. Vaeggemose, M.G. D'Angelo, F. Arrigoni, H.E. Kan, M. Froeling, "Multi-center evaluation of stability and reproducibility of quantitative MRI measures in healthy calf muscles". NMR in Biomedicine 32, 9. (2019)

J19 S. Schlaeger, **D. Weidlich**, E. Klupp, F. Montagnese, M. Deschauer, B. Schoser, S. Bublitz, S. Ruschke, C. Zimmer, E.J. Rummeny, J.S. Kirschke, D.C. Karampinos, "Decreased water T2 in fatty infiltrated skeletal muscles of patients with neuromuscular diseases", NMR in Biomedicine 32, 8. (2019)

J20 N. Sollmann, **D. Weidlich**, B. Cervantes, E. Klupp, C. Ganter, H. Kooijman, C. Zimmer, E.J. Rummeny, B. Meyer, T. Baum, J.S. Kirschke, D.C. Karampinos, "T2 mapping of lumbosacral nerves in patients suffering from unilateral radicular pain due to degenerative disc disease". Journal of Neurosurgery: Spine 22,1-9. (2019)

J21 D. Franz, M.N. Diefenbach, F. Treibel, **D. Weidlich**, J. Syvaeri, S. Ruschke, M. Wu, C. Holzapfel, T. Drabsch, T. Baum, H. Eggers, E.J. Rummeny, H. Hauner, D.C. Karampinos, "Differentiating supraclavicular from gluteal adipose tissue based on simultaneous PDFF and T2* mapping using a 20-echo gradient-echo acquisition", Journal of Magnetic Resonance Imaging 50:424-434. (2019)

J22 N. Sollmann, **D. Weidlich**, B. Cervantes, E. Klupp, C. Ganter, H. Kooijman, E.J. Rummeny, C. Zimmer, J.S. Kirschke, D.C. Karampinos, "High Isotropic Resolution T2 Mapping of the Lumbosacral Plexus with T2-Prepared 3D Turbo Spin Echo", Clinical Neuroradiology 29:223-230. (2019)

J23 N. Sollmann, N. Mathonia, **D. Weidlich**, M.V. Bonfert, S.A. Schroeder, K.A. Badura, T. Renner, F. Trepte-Freisleder, C. Ganter, S.M. Krieg, C. Zimmer, E.J. Rummeny, D.C. Karampinos, T. Baum, M.N. Landgraf, Heinen, F., "Quantitative magnetic resonance imaging of the upper trapezius muscles – assessment of myofascial trigger points in patients with migraine", The Journal of Headache and Pain 20, 8. (2019)

J24 S. Schlaeger, S. Inhuber, A. Rohrmeier, M. Dieckmeyer, F. Freitag, E. Klupp, **D. Weidlich**, G. Feuerriegel, F. Kreuzpointner, A. Schwirtz, E.J. Rummeny, C. Zimmer, J.S. Kirschke, D.C. Karampinos, T. Baum, "Association of paraspinal muscle water–fat MRI-based measurements with isometric strength measurements", European Radiology 29, 599–608. (2019)

J25 B. Cervantes, A.T. Van, **D. Weidlich**, H. Kooijman, A. Hock, E.J. Rummeny, A. Gersing, J. S. Kirschke, D.C. Karampinos, "Isotropic resolution diffusion tensor imaging of lumbosacral and sciatic nerves using a phase-corrected diffusion-prepared 3D turbo spin echo", Magn. Reson. Med., 80: 609-618. (2019)

J26 D. Franz, J. Syvaeri, **D. Weidlich**, T. Baum, E.J. Rummeny, D.C. Karampinos, "Magnetic Resonance Imaging of Adipose Tissue in Metabolic Dysfunction", Rofo 190:1121-1130. (2019)

J27 N. Sollmann*, **D. Weidlich***, B. Cervantes, E. Klupp, C. Ganter, H. Kooijman, C. Zimmer, E.J. Rummeny, J.S. Kirschke, D.C. Karampinos, "High Isotropic Resolution T2 Mapping of the Lumbosacral Plexus with T2-Prepared 3D Turbo Spin Echo", Clinical Neuroradiology 29:223-230. (2019) * These authors contributed equally

J28 N. Sollmann, M. Dieckmeyer, S. Schlaeger, A. Rohrmeier, J. Syvaeri, M.N. Diefenbach, **D. Weidlich**, S. Ruschke, E. Klupp, D. Franz, E.J. Rummeny, C. Zimmer, J.S. Kirschke, D.C. Karampinos, T. Baum, "Associations Between Lumbar Vertebral Bone Marrow and Paraspinal Muscle Fat Compositions—An Investigation by Chemical Shift Encoding-Based Water-Fat MRI", Frontiers in Endocrinology 9, 563. (2018)

J29 D. Franz, **D. Weidlich**, F. Freitag, Holzapfel C., T. Drabsch, T. Baum, H. Eggers, A. Witte, E.J. Rummeny, H. Hauner, D.C. Karampinos, "Association of proton density fat fraction in adipose tissue with imaging-based and anthropometric obesity markers in adults" International Journal of Obesity. 42:175-182 (2018)

J30 S. Schlaeger, F. Freitag, E. Klupp, M. Dieckmeyer, **D. Weidlich**, S. Inhuber, M. Deschauer, B. Schoser, S. Bublitz, F. Montagnese, C. Zimmer, E.J. Rummeny, D.C. Karampinos, J.S. Kirschke, T. Baum, "Thigh muscle segmentation of chemical shift encoding-based water-fat magnetic resonance images: The reference database MyoSegmenTUM", PLOS ONE 13:6. (2018)

J31 S. Schlaeger, E. Klupp, **D. Weidlich**, B. Cervantes, S.C. Foreman, M. Deschauer, B. Schoser, C. Katemann, H. Kooijman, E.J. Rummeny, C. Zimmer, J.S. Kirschke, D.C. Karampinos, "T2-Weighted Dixon Turbo Spin Echo for Accelerated Simultaneous Grading of Whole- Body Skeletal Muscle Fat Infiltration and Edema in Patients With Neuromuscular Diseases", Journal of Computer Assisted Tomography 42:497-501. (2018)

J32 **D. Weidlich**, S. Schlaeger, H. Kooijman, P. Börnert, J. S. Kirschke, E.J. Rummeny, A. Haase, D.C. Karampinos, "T2 mapping with magnetization-prepared 3D TSE based on a modified BIR-4 T2 preparation", NMR in Biomedicine, 30(11). (2017)

J33 E. Klupp, **D. Weidlich**, S. Schlaeger, T. Baum, B. Cervantes, M. Deschauer, H. Koojiman, E.J. Rummeny, C. Zimmer, J.S. Kirschke, D.C. Karampinos, "B1-insensitive T2 Mapping of Healthy Thigh Muscles Using a T2-prepared 3D TSE Sequence". PLOS ONE, 12:2. (2017)

The author contributed also to the following book chapter:

B1 D.C. Karampinos, **D. Weidlich**, M. Wu, H.H. Hu, D. Franz "Techniques and Applications of Magnetic Resonance Imaging for Studying Brown Adipose Tissue Morphometry and Function". In: Handbook of Experimental Pharmacology. Springer, Berlin, Heidelberg (2019)

The author contributed also to the following patent applications:

P1 **D. Weidlich**, S. Ruschke, D.C. Karampinos, A. Hock, "MRI With Matching Vibrational States", Patent Application Number: EP3959532A1 (pending)

P2 **D. Weidlich**, S. Ruschke, E. Huaroc, M. Doneva, D.C. Karampinos, "Quantitative Magnetic Resonance Imaging in the Presence of Fat", Patent Application Number: EP4057021A1 (pending)

The author contributed also to the following conference abstracts (ordered by year of appearance):

C1 **D. Weidlich**, J. Honecker, C. Boehm, S. Ruschke, D. Junker, A.T. Van, M.R. Makowski, C. Holzapfel, M. Claussnitzer, H. Hauner, D.C. Karampinos, "Lipid droplet size mapping in human adipose tissue using a clinical 3 T system", 29th Annual Meeting of ISMRM (p. 752), Virtual Meeting (oral), **ISMRM Magna Cum Laude Award** (2021)

C2 **D. Weidlich**, J. Honecker, C. Seeliger, D. Junker, M.R. Makowski, H. Hauner, D.C. Karampinos, S. Ruschke, "Feasibility of model-based omega-3 fatty acid fraction mapping using multi-echo gradient-echo imaging at 3T", 29th Annual Meeting of ISMRM (p. 1271), Virtual Meeting (digital poster) (2021)

C3 M. Zamskiy, **D. Weidlich**, K. Weiss, M.R. Makowski, R.F. Braren, D.C. Karampinos, "Isotropic resolution volumetric liver T2 weighted imaging and T2 mapping using a navigator-gated radial stack-of-stars T2 prepared acquisition", 29th Annual Meeting of ISMRM (p. 1875), Virtual Meeting (digital poster) (2021)

C4 E. Huaroc, **D. Weidlich**, T. Amthor, P. Koken, M. Baumann, K. Weiss, M.R. Makowski, B. Schwaiger, M. Doneva, D.C. Karampinos, "On the effect of fat spectrum complexity in Dixon MR Fingerprinting", 29th Annual Meeting of ISMRM (p. 3846), Virtual Meeting (digital poster) (2021)

C5 S. Ruschke, J. Honecker, **D. Weidlich**, C. Seeliger, O. Prokopchuk, J. Ecker, M.R. Makowski, H. Hauner, D.C. Karampinos, "Characterization of the triglyceride fatty acid composition and adipocyte size in human adipose tissue using SHORTIE STEAM: in vitro validation", 29th Annual Meeting of ISMRM (p. 3837), Virtual Meeting (digital poster) (2021)

C6 **D. Weidlich**, M. Zamskiy, M. Maeder, S. Ruschke, S. Marburg, D.C. Karampinos, "Reduction of vibration-induced signal loss by matching mechanical vibrational states: application in high b-value diffusion weighted MRS", 28th Annual Meeting of ISMRM (p. 659), Virtual Meeting (oral) (2020)

C7 **D. Weidlich**, J. Honecker, S. Ruschke, L. Patzelt, C. Held., M. Wu, D. Franz, S. Winkler, H. Hauner, D.C. Karampinos, "Comparison of adipocyte size measurements with histology and high b-value diffusion-weighted spectroscopy in human white adipose tissue at 3 T", 28th Annual Meeting of ISMRM (p. 4680), Virtual Meeting (digital poster), **ISMRM Magna Cum Laude Award** (2020)

C8 S. Kronthaler, C. Boehm, **D. Weidlich**, M.N. Diefenbach, H. Hauner, D.C. Karampinos, "Simultaneous imaging of trabecular and cortical bone by analyzing the multi-echo signal decay at UTEs and conventional TEs", 28th Annual Meeting of ISMRM (p. 4945), Virtual Meeting (digital poster) (2020)

C9 S. Ruschke, **D. Weidlich**, J. Honecker, C. Seelinger, J. Ecker, O. Prokopchuk, H. Hauner, D.C. Karampinos, "Estimation of the triglyceride fatty acid composition in human adipose tissue using multi-TE and SHORTIE STEAM: in vitro validation using GC-MS", 28th Annual Meeting of ISMRM (p. 4882), Virtual Meeting (digital poster) (2020)

C10 C. Boehm, **D. Weidlich**, S. Kronthaler, D.C. Karampinos, "On the Carbon Footprint of ISMRM's Annual Meeting: Analysis and Implications", 28th Annual Meeting of ISMRM (p. 5379), Virtual Meeting (digital poster) (2020)

C11 M.V. Bonfert, P. Schandelmaier, **D. Weidlich**, D.C. Karampinos, C. Boerner , G. Urban, H. Koenig, M.N. Landgraf,T. Baum, F. Heinen, N. Sollmann, "Alterations in the upper trapezius muscle in migraine patients assessed by quantitative magnetic resonance imaging using T2 mapping", 14th European Headache Federation Congress (p. 205), Berlin, Germany (poster) (2020)

C12 **D. Weidlich**, S. Ruschke, M. Wu, R. Burgkart, A. Hock, D.C. Karampinos, "Reduction of signal loss induced by scanner table vibrations in high b-value diffusion weighted MRS of lipids", ISMRM Workshop on MRI of Obesity and Metabolic Disorders (p. 19), Singapore, (power pitch presentation) (2019)

C13 **D. Weidlich**, M. Zamskiy, S. Ruschke, J. Honecker, T. Skurk, M. Wu, H. Hauner, D.C. Karampinos, "Spatially resolved lipid droplet size mapping with a high b-value diffusion weighted 2D TSE sequence in phantoms, human adipose tissue samples and in vivo" ISMRM Workshop on MRI of Obesity and Metabolic Disorders. Singapore. (oral) (2019)

C14 M. Wu, C. Held, L. Patzelt, **D. Weidlich**, S. Ruschke, L. Mengel, H. Hauner, D. Franz, D.C. Karampinos, "Brown adipose tissue water ADC quantification with Diffusion-Weighted MR Spectroscopy in the human supraclavicular fat", ISMRM Workshop on MRI of Obesity and Metabolic Disorders, Singapore. (oral) (2019)

C15 **D. Weidlich**, J. Honecker, O. Gmach, M. Wu, R. Burgkart, S. Ruschke, D. Franz, B. Menze, T. Skurk, H. Hauner, U. Kulozik, D.C. Karampinos, "Measuring large lipid droplet sizes by probing restricted lipid diffusion effects with Diffusion-Weighted Magnetic Resonance Spectroscopy at 3 T", 27th Annual Meeting of ISMRM (p. 373), Montreal, Canada (oral) **ISMRM Magna Cum Laude Award** (2019)

C16 **D. Weidlich**, M. Wu, S. Ruschke, D. Franz, J. Honecker, O. Gmach, T. Skurk, H. Hauner, U. Kulozik, D.C. Karampinos, "Spatially resolved measurement of lipid droplet size in white adipose tissue with high b-value stimulated echo-prepared diffusion-weighted 2D single shot TSE", 27th Annual Meeting of ISMRM (p. 1927), Montreal, Canada (digital poster) (2019)

C17 **D. Weidlich**, S. Ruschke, M. Wu, A. Hock, R. Burgkart, D.C. Karampinos, "Compensation of signal loss induced by scanner table vibrations in high b-value DW-TSE for measuring lipids ADC", 27th Annual Meeting of ISMRM (p. 3390), Montreal, Canada (digital poster) (2019)

C18 M. Loeffler, S. Schlaeger, S. Inhuber, M. Dieckmeyer, **D. Weidlich**, A. Schwirtz, E. Rummeny, C. Zimmer, J.S. Kirschke, D.C. Karampinos, T. Baum, "Regional thigh muscle composition based on chemical shift encoding-based water-fat MRI and its association with muscle strength", 27th Annual Meeting of ISMRM (p. 1261), Montreal, Canada (digital poster) (2019)

C19 M. Wu, **D. Weidlich**, S. Ruschke, D. Franz, D.C. Karampinos, "On the Technical Challenges of Diffusion-Weighted MR Spectroscopy for Water ADC Quantification in

Human Supraclavicular Fat", 27th Annual Meeting of ISMRM (p. 1930), Montreal, Canada (digital poster) (2019)

C20 D. Franz, **D. Weidlich**, J. Syvaeri, S. Ruschke, M. Wu, C. Holzapfel, T. Drabsch, E. Rummeny, H. Hauner, D.C. Karampinos, "MRS-based water T2 relaxation time in the supraclavicular fossa relates to anthropometric and imaging obesity markers", 27th Annual Meeting of ISMRM (p. 1942), Montreal, Canada (digital poster) (2019)

C21 N. Sollmann, **D. Weidlich**, B. Cervantes, E. Klupp, C. Ganter, H. Kooijman, C. Zimmer, E. Rummeny, B. Meyer, T. Baum, J.S. Kirschke,D.C. Karampinos, "T2 mapping of lumbosacral nerves in patients suffering from unilateral radicular pain due to degenerative disc disease", 27th Annual Meeting of ISMRM (p. 2874), Montreal, Canada (digital poster) (2019)

C22 S. Ruschke, **D. Weidlich**, M. Wu, A. Hock, D.C. Karampinos, "Single-voxel short-TR multi- TI multi-TE (SHORTIE) STEAM for water–fat magnetic resonance spectroscopy", 27th Annual Meeting of ISMRM (p. 4230), Montreal, Canada (digital poster) (2019)

C23 M. Hauke, **D. Weidlich**, C. Ganter, A. Haase, D.C. Karampinos, "Insights from the Configuration Model theory accelerate Bloch simulations for dictionary-based T2 mapping", 27th Annual Meeting of ISMRM (p. 4985), Montreal, Canada (digital poster) (2019)

C24 M. Loeffler, S. Schlaeger, S. Inhuber, M. Dieckmeyer, **D. Weidlich**, A. Schwirtz, E.J. Rummeny, C. Zimmer, J. S. Kirschke, D.C. Karampinos, T. Baum "Regional thigh muscle composition based on chemical shift encoding-based water-fat MRI and its association with muscle strength". In: Proceedings 27. Annual Meeting International Society for Magnetic Resonance in Medicine (p. 1261), Montreal, Canada (e-poster) (2019)

C25 **D. Weidlich**, M. Wu, S. Ruschke, D. Franz, J. Honecker, O. Gmach, T. Skurk, H. Hauner, U. Kulozik, D.C. Karampinos, "Spatially resolved measurement of lipid droplet size in white adipose tissue with high b-value stimulated echo-prepared diffusion-weighted 2D single shot TSE", Minerva-Gentner Symposia on MR Spectroscopy and Molecular Imaging. Weizmann Institute, Israel. (oral) (2019)

C26 **D. Weidlich**, S. Ruschke, B. Cervantes, A. Hock, D.C. Karampinos, "ADC quantification of lipids with high b-value stimulated echo-prepared diffusion-weighted 2D single shot TSE", 26th Annual Meeting of ISMRM (p. 2511), France, Paris (poster) **ISMRM Magna Cum Laude Award** (2018)

C27 **D. Weidlich**, M.N. Diefenbach, S. Schlaeger, A. Hock, S. Ruschke, D.C. Karampinos, "In-vivo water T2 mapping in tissues containing water and fat using a T2-prepared 3D Dixon TSE sequence and a pre-calibrated fat spectrum model", 26th Annual Meeting of ISMRM (p. 4223), France, Paris (e-poster) (2018)

C28 B. Cervantes, A.T. Van, **D. Weidlich**, H. Kooijman, A. Hock, E.J. Rummeny, A. Gersing, J.S. Kirschke, D.C. Karampinos, "Isotropic resolution DTI of lower back nerves using a phase-corrected diffusion-prepared 3D TSE", 26th Annual Meeting of ISMRM, France (p. 1045), Paris (oral presentation) (2018)

C29 D. Franz, **D. Weidlich**, S. Syvaeri, M.N. Diefenbach, C. Holzapfel, T. Drabsch, T. Baum, H. Eggers, E.J. Rummeny, H. Hauner, D.C. Karampinos, "The presence of brown adipose tissue is associated with thyroid function in subjects with low and normal BMI", 26th Annual Meeting of ISMRM (p. 1266), France, Paris (oral presentation) (2018)

C30 D. Franz, M.N. Diefenbach, J. Syvaeri, **D. Weidlich**, E.J. Rummeny, H. Hauner, S. Ruschke, D.C. Karampinos, "Differentiating supraclavicular from gluteal adipose tissue based on simultaneous PDFF and T2* mapping using a twenty-echo gradient echo acquisition", 26th Annual Meeting of ISMRM (p. 2498), France, Paris (poster) (2018)

C31 S. Schlaeger, **D. Weidlich**, E. Klupp, F. Montagnese, M. Deschauer, B. Schoser, S. Bublitz, C. Zimmer, E.J. Rummeny, J.S. Kirschke, D.C. Karampinos, "Decreasing Water T2 based on multi-TE single-voxel MRS in fatty infiltrated skeletal muscles of patients with neuromuscular diseases", 26th Annual Meeting of ISMRM (p. 5059), France, Paris (e-poster) (2018)

C32 S. Schlaeger, **D. Weidlich**, E. Klupp, F. Montagnese, M. Deschauer, B. Schoser, S. Bublitz, C. Zimmer, E.J. Rummeny, J.S. Kirschke, D.C. Karampinos, "Water T2 mapping in fatty infiltrated thigh muscles of patients with neuromuscular diseases using a T2-prepared 3D TSE with SPAIR", 26th Annual Meeting of ISMRM (p. 0815), France, Paris (oral presentation) **ISMRM Magna Cum Laude Award** (2018)

C33 E. Klupp, B. Cervantes, N. Sollmann, F. Treibel, **D. Weidlich**, T. Baum, E.J. Rummeny, C. Zimmer, J.S. Kirschke, D.C. Karampinos "Improved brachial plexus visualization using an adiabatic iMSDE-prepared STIR 3D TSE", 26th Annual Meeting of ISMRM (p. 5392), France, Paris (e-poster) (2018)

C34 N. Sollmann, M. Dieckmeyer, S. Schlaeger, R. Rohrmeier, J. Syvaeri, M.N. Diefenbach, **D. Weidlich**, S. Ruschke, E. Klupp, D. Franz, E.J. Rummeny, C. Zimmer, J.S. Kirschke, D.C. Karampinos, T. Baum "Associations between lumbar vertebral bone marrow and paraspinal muscle fat compositions—an in- vestigation by chemical shift encoding-based water-fat MRI". Proceedings of 4th International Meeting on Bone Marrow Adiposity. Lille, France (oral presentation) (2018)

C35 **D. Weidlich**, A. Hock, S. Ruschke, D. Franz, H. Hauner, E.J. Rummeny, D.C. Karampinos, "Improving the quality of DW spectra in the supraclavicular fossa with a navigator-gated and cardiac-triggered flow-compensated diffusion-weighted STEAM MRS acquisition", 25th Annual Meeting of ISMRM (p. 5490), USA, Hawaii, Honolulu (e-poster) (2017)

C36 **D. Weidlich**, A. Hock, S. Ruschke, D. Franz, K. Steiger, T. Skurk, H. Hauner, E.J. Rummeny, D.C. Karampinos, "Probing bone marrow adipocyte cell size in vivo at a clinical 3 T scanner using high b-value DW-MRS at long diffusion times", 25th Annual Meeting of ISMRM (p. 1227), USA, Hawaii, Honolulu (oral presentation). **ISMRM Summa Cum Laude Award** (2017)

C37 D. Franz, **D. Weidlich**, F. Freitag, C. Holzapfel, T. Baum, H. Eggers, E.J. Rummeny, H. Hauner, D.C. Karampinos "Supraclavicular and gluteal adipose tissue PDFF is associated to volumes of VAT and SAT and to anthropometric obesity markers in healthy adults", 25th Annual Meeting of ISMRM (p. 3432), USA, Hawaii, Honolulu (e-poster) (2017)

C38 S. Ruschke, A. Hock, **D. Weidlich**, E.J. Rummeny, J.S. Kirschke, T. Baum, R. Krug, D.C. Karampinos "Measuring fat unsaturation and polyunsaturation in vertebral bone marrow using dynamic inversion-recovery single-voxel spectroscopy", 25th Annual Meeting of ISMRM (p. 5115), USA, Hawaii, Honolulu (e-poster) (2017)

C39 S. Schlaeger, E. Klupp, **D. Weidlich**, B. Cervantes, M. Deschauer, B. Schoser, S. Bublitz, F. Montagnese, C. Katemann, H. Kooijman, E.J. Rummeny, C. Zimmer, J.S. Kirschke, D.C. Karampinos "T2-weighted Dixon TSE for accelerated simultaneous grading of whole body skeletal muscle fat infiltration and edema in patients with neuromuscular diseases", 25th Annual Meeting of ISMRM (p. 5011), USA, Hawaii, Honolulu (e-poster) (2017)

C40 S. Schlaeger, **D. Weidlich**, E. Klupp, F. Montagnese, B. Schoser, S. Bublitz, M. Deschauer, C. Zimmer, D.C. Karampinos, J.S. Kirschke, "Robuste Oedemquantifizierung bei Patienten mit neuromuskulaeren Erkrankungen mittels einer neuen T2 mapping-Sequenz", Proceedings of 52. Jahrestagung der Deutschen Gesellschaft fuer Neuroradiologie e. V. Cologne, Germany (oral presentation) (2017)

C41 S. Schlaeger, **D. Weidlich**, E. Klupp, M. Deschauer, B. Schoser, S. Bublitz, F. Montagnese, E.J. Rummeny, C. Zimmer, J.S. Kirschke, D.C. Karampinos "Water T2 mapping of the fatty infiltrated thigh musculature using a T2-prepared 3D TSE sequence combined with SPAIR". Imaging in Neuromuscular Disease. (traditional poster). Berlin, Germany (2017)

C42 S. Schlaeger, E. Klupp, **D. Weidlich**, S. Bublitz, F. Montagnese, C. Zimmer, M. Deschauer, B. Schoser, D.C. Karampinos, Kirschke. J. S., "Vergleich von T2W STIR und Dixon FFE mit T2W Dixon anhand von Rating- Skalen fuer oedematoese und fettige Veraenderungen in der Oberschenkelmuskulatur von Patienten mit neuromuskulaeren Erkrankungen". In: 23. Kongress des Wissenschaftlichen Beirates der Deutschen Gesellschaft fuer Muskelkranke e.V. (oral presentation). Munich, Germany (2017)

C43 **D. Weidlich**, H. Kooijman, P. Börnert, J. S. Kirschke, E.J. Rummeny, A. Haase, D.C. Karampinos, "Quantitative T2 mapping using a modified BIR-4 T2 preparation in the presence of large B0 offsets", 24th Annual Meeting of ISMRM (p. 2824), Singapore, Singapore (e-poster) (2016)

C44 **D. Weidlich**, B. Cervantes, N. Sollmann, H. Kooijman, J. S. Kirschke, E.J. Rummeny, A. Haase, D.C. Karampinos, "B1-insensitive high-resolution isotropic T2 mapping of the lumbar plexus with a T2-prepared 3D TSE", 24th Annual Meeting of ISMRM (p. 4469), Singapore, Singapore (e-poster) (2016)

C45 S. Ruschke, **D. Weidlich**, M.N. Diefenbach, H. Eggers, H. Kooijman, H.H. Hu, E.J. Rummeny, A. Haase, J. S. Kirschke, T. Baum, D.C. Karampinos, "Simultaneous T2, T2' and PDFF mapping in the spine using an adiabatic T2-prepared time-interleaved multi-echo gradient echo acquisition", 24th Annual Meeting of ISMRM (p. 0568), Singapore, Singapore (oral presentation). **ISMRM Magna Cum Laude Award** (2016)

C46 E. Klupp, **D. Weidlich**, T. Baum, B. Cervantes, M. Deschauer, H. Kooijman, E.J. Rummeny, C. Zimmer, J.S. Kirschke, D.C. Karampinos, "Comparison of T2-prepared 3D TSE with multi- echo spin echo sequences for T2 mapping of thigh muscles in healthy

volunteers", 24th Annual Meeting of ISMRM (p. 4511), Singapore, Singapore (e-poster) (2016)

C47 B. Cervantes, **D. Weidlich**, H. Kooijman, E.J. Rummeny, A. Haase, J. S. Kirschke, D.C. Karampinos, "High-Resolution DWI of the Lumbar Plexus using B1-insensitive Velocity-Compensated Diffusion-Prepared 3D TSE", 24th Annual Meeting of ISMRM (p. 4474), Singapore, Singapore (e-poster) (2016)

C48 B. Cervantes, H.H. Hu, A. Pokorney, **D. Weidlich**, H. Kooijman, E.J. Rummeny, A. Haase, J. S. Kirschke, D.C. Karampinos, "CSF-Free Imaging of the Lumbar Plexus using Sub-Millimeter Resolutions with 3D TSE", 24th Annual Meeting of ISMRM (p. 2250), Singapore, Singapore (poster). **ISMRM Magna Cum Laude Award** (2016)

C49 S. Ruschke, **D. Weidlich**, M.N. Diefenbach, H. Eggers, H. Kooijman, H.H. Hu, E.J. Rummeny, A. Haase, J. S. Kirschke, T. Baum, D.C. Karampinos, "Simultaneous T2, T2* and PDFF mapping using an adiabatic T2-prepared time-interleaved multi-echo gradient echo acquisition", ISMRM Workshop on Data Sampling and Image Reconstruction (p. 36), USA, Arizona, Sedona (poster) (2016)

Contents

1 Introduction

Tomographic imaging techniques are an integral part of modern medicine because they allow to investigate the anatomy of the human body. Magnetic resonance (MR) imaging with its high soft-tissue contrast and the absence of ionizing radiation is a particularly valuable tool in both clinical and research settings. The possibility to acquire images with multiple tissue contrasts allows the extraction of a variety of different information. With the help of diffusion weighted (DW) MR measurements and appropriate signal modeling, information about the tissue microstructure can be revealed.

1.1 Clinical Relevance

Globally and in the past decades, the prevalence of obesity is rapidly increasing. The associated negative effects on the individual health as well as comorbidities like diabetes type 2 constitute a big social economical burden on society. [1–3] The microstructure of adipose tissue (AT) could potentially reveal information about the underlying pathophysiological processes in obesity and diabetes [4]. In white AT, the adipocyte size has long been known to relate to the obese phenotype. An increase in adipocyte size in subcutaneous and visceral white AT can be observed in adults with the onset of obesity predominately due to enlargement of the fat cell volume [5]. This increase in the adipocyte size is also related to inflammatory processes being present in the tissue [6]. The adipocyte size in white AT is associated with prevalence of type 2 diabetes, dyslipidemia and the cardiometabolic risk [4, 7, 8]. Therefore, the assessment of adipocyte size is highly desirable to improve the metabolic phenotyping of patients, especially as they undergo interventions. However, the measurement of lipid droplet size in tissue normally requires a highly invasive biopsy procedure.

1.2 Thesis Purpose

DW-MR is a powerful tool for the non-invasive assessment of tissue microstructure. The reduction of the apparent diffusion coefficient with increasing diffusion times due to diffusion restriction effects has been previously applied to extract cell size in vivo in water-containing tissues such as axon diameters in the brain [9–11] or cell size of tumors in breast cancer [12]. Measuring the diffusion properties of lipids has been proven to be more challenging because fat has a diffusion coefficient approximately two orders of magnitude lower than water due to the large molecular size of fatty acids [13]. A low lipid diffusion coefficient increases the required diffusion encoding strength and diffusion time. This creates additional technical challenges related to eddy currents and increased sensitivity to any type of physiological tissue motion (respiratory motion and cardiac-induced blood pulsation) as well as involuntary movement. Extracting microstructural information from AT was shown to be possible in the size estimation of intramyocellular lipids [14] and brown adipocytes [15]. However, these measurements were mostly performed ex vivo on a pre-clinical scanner with a strong gradient system in relatively small adipocytes (diameter smaller than 10 μm). The lipid droplet

diameter in white AT is between 50 μm to 150 μm and the associated diffusion restriction effects are much smaller and more challenging to measure [16]. This thesis aims to develop techniques to probe the size of large adipocytes on a clinical scanner. Moreover, a technique is presented to reduce the effect of hardware vibrations on the measurements.

1.3 Thesis Structure

In chapter 2, the importance of adipose tissue microstructure in the context of the metabolic syndrome is given. The methodological foundation in the context of the embedded journal publications is given in chapter 3. A short overview of the physical background and employed techniques in DW-MR measurement techniques and the modeling of restricted diffusion is given in chapter 4. A description of the employed MR spectroscopy and imaging sequences is given at the end of chapter 4. Summaries of the three embedded journal publications can be found in chapter 6 followed by the original manuscripts. Finally, an overall discussion on the implications of the present work and its literature context is given in chapter 7.

2 Importance of Adipose Tissue Microstructure in the Context of the Metabolic Syndrome

2.1 The Metabolic Syndrome

According to International Diabetes Federation (IDF) the metabolic syndrome is a cluster of the most dangerous heart attack risk factors: diabetes and raised fasting plasma glucose, abdominal obesity, high cholesterol and high blood pressure [17]. Although the presence of the metabolic syndrome is described as early as in the 1920s [18], a uniform definition is still lacking [19]. Besides the definition from the IDF, there are official definitions from the World Health Organization (WHO) [20], the European Group for the Study of Insulin Resistance [21] and the National Cholesterol Education Program-Third Adult Treatment Panel [22]. Despite, the controversy about the exact definition of the syndrome and the guidelines that should be used in the clinical routine, its importance is indisputable.

The prevalence ranges depending on the investigated population and employed syndrome definition from single digit percentage to a quarter or third of the whole population [23]. The effects of this cluster of conditions are striking: People with metabolic syndrome are twice as likely to die from and three times as likely to have a heart attack or stroke compared to people without the syndrome [24].

While the exact interaction and causal relation of the different components of the metabolic syndrome are poorly understood, insulin resistance and obesity are considered to have significant impact [25–27].

2.2 Obesity

Obesity is defined a positive energy balance with energy intake overriding energy expenditure resulting in negative effects on the individual's health condition [28]. According to the WHO overweight is defined as a Body Mass Index (BMI) greater than or equal to 25 kg/m^2, whereas obesity is a BMI greater than or equal to 30 kg/m^2 [29]. Globally, the prevalence of obesity has nearly doubled between 1980 and 2008 [1]. Based on the latest estimates in the European Union, overweight affects 30-70% and obesity affects up to 30% of adults [2, 3]. Overweight and obesity are responsible for about 80% of cases of type 2 diabetes, 35% of cases of ischemic heart disease and 55% of cases of high blood pressure among adults in most European Union countries [1]. Obesity causes dysfunction of the adipose tissue and is tightly linked to severe metabolic disorders [30]. Despite the great clinical relevance of obesity, the patient management remains a major challenge: Although, clinical procedures for diagnosis based on anthropometric biomarkers are available, the identification of phenotypes at risk for developing obesity-related complications is challenging [31–33]. There is evidence that also individuals that are considered as highly obese with traditional measures (like BMI), can

be metabolically healthy [31]. The term "metabolically healthy obese" (MHO) is frequently used for this phenomenon. However, it is worth mentioning that MHO often suffer from other diseases besides their reduced cardiometabolic risk and MHO is also believed to be a transient state and the longer those formerly "healthy" individuals stay obese, the more co-morbidities they are developing. [34, 35]

These observations lead to a rethinking of the traditional phenotyping in obesity. Concepts like the "Adipose Tissue Expandability Hypothesis" according to which the AT has a certain capacity of storing lipids become more popular. Above the storage limit any additional nutrition must be stored as ectopic fat in muscle tissue, liver tissue and visceral tissue with negative metabolic consequences [36].

In the clinical routine most physicians aim to archive weight loss of obese patients with life style interventions such as dietary change and increased physical activity. Medication and bariatric surgery is recommended in severe cases [37]. However, a clear definition of different risk phenotypes in obesity is lacking and without a more compartmentalized classification of obesity the options for personalized treatment approaches are limited [38]. The current approach does not capture differences in the large group of obese patients that could potentially lead to an identification of patients at higher risk and consequently a more effective treatment.

2.3 Diabetes

Worldwide, an estimate of 415 million people are diagnosed with diabetes and an approximate of 193 million people are living with undiagnosed diabetes. Approximately 90% of the patients have type 2 diabetes, which is characterized by a reduced sensitivity and eventually resistance of the cells in the body to insulin [39]. The hormone insulin plays a key role in the body's energy balance by facilitating glucose uptake in the cell and regulating metabolic processes [40]. Recent data suggests that the number of people with diabetes will increase from 415 million in 2015 to 642 million in 2040 [41]. Type 2 diabetes is a leading cause of cardiovascular disorders, blindness, amputations, and hospitalizations and is associated with an increased risk of cancer, mental illness, chronic liver disease or arthritis [42, 43]. In 2003, the total direct healthcare costs of all diabetes patients in the age group 20–79 years in 25 European Union countries was around 64.9 billion international dollars (7.2% of the total health expenditure) [44].

The main characteristic of diabetes is hyperglycemia, which refers to high levels of glucose in the blood, which is strongly related to a risk of microvascular and macrovascular complications [45]. Chronic hyperglycemia is associated with long-term damage and dysfunction of various organs, especially the eyes, kidneys, nerves, heart, and blood vessels [46].

Diabetes can eventually be diagnosed by this increased glucose levels in the blood [46]. Due to the negative effects of hyperglycemia, reducing the glucose levels in the blood is the main target in therapy. Current therapeutic options include a wide range of pharmacological agents up to insulin substitution as well as life style interventions such as weight loss, dietary intervention or physical activity. [47].

However, an increased risk for cardio-vascular diseases can be observed in patients even before levels of blood glucose are high enough to indicate diabetes [48]. There is evidence that a more detailed phenotyping of diabetic patients could improve patient management [49]. An earlier detection of signs indicating the development of diabetes would therefore greatly enhance the novel phenotyping approach and could improve patient treatment.

2.4 Role of Adipose Tissue Microstructure in Obesity and Diabetes

In both obesity and diabetes type 2, AT plays a major role during the development and the progression of the diseases. AT is a unique organ with high plasticity that can reduce and increase in size depending on the relation between calorie intake and energy consumption [50]. This dynamic change of the tissue size can be archived in two ways: Either by changing the number or the size of the fat cells (adipocytes). Therefore, plasticity of AT can particularly be observed in the tissue microstructure.

In the context of obesity, an increased number of adipocytes (hyperplasia) only seems to play a minor role compared to the increase of adipocyte size (hypertrophy) [51]. It is well known that the adipocyte size is related to the obese phenotype [5]. It also makes sense, according to the "Adipose Tissue Expandability Hypothesis", that the adipocytes' volume need to increase in case of a positive energy balance because more and more lipids need to be stored in the body. Eventually after reaching the maximum capacity, ectopic accumulation of fat will occur with associated negative impacts [52]. Patients with hypertrophic fat cells also show a larger prevalence of inflammatory processes in the adipose tissue [6]. This internal processes can not be evaluated from the outside or by anthropometric markers although they could potentially carry important information for risk phenotyping. Adipocyte size could help identify the MHOs, who are more likely to develop diabetes [53]. In type 2 diabetes, there is growing evidence that adipocyte size correlates with insulin sensitivity: Multiple studies investigating biopsy samples report a positive correlation between the mean adipocyte size and markers for diabetes [4, 7, 8]. However, also an enhanced proportion of small adipocytes were found in insulin resistant individuals indicating a disturbance of hyperplasia processes in the tissue [54]. Changes in AT microstructure could be seen as an indirect measurement of the pathophysiological processes accompanying the development of diabetes. This is particular interesting because the adipocyte size could therefore serve as a potential novel early-onset biomarker for the development of diabetes [55]. Identifying individuals at an early stage could improve patient management and eventually reduce the burden on the health care system.

Consequently, an in vivo assessment of adipocyte size could serve as a potential early biomarker for therapy monitoring in obese as well as diabetic patient groups. Up to now the measurement of adipocyte size requires highly invasive biopsies. Subsequently, the obtained adipose tissue samples are investigated in a laboratory setting with collogenese digestion, osmium tetroxide fixation or histological analysis. All three methods show differences in their absolute obtained quantitative values but correlate well with each other [16]. However, the need for an invasive procedure disqualifies the proposed method for screening protocols or longitudinal studies assessing disease progression or monitoring therapeutic intervention.

The non-invasive probing of white AT microstructure could provide ground-breaking solutions for overcoming the existing challenges in the assessment of the risk for developing associated metabolic complications. It could not only help to understand the pathophysiological processes in obesity and diabetes in more detail, but could also be used in other diseases which are associated with microstructural changes of AT such as oncological settings, non-alcoholic fatty liver disease or the investigation of lipid metabolism [4]. However, up to now no technology for an in vivo and non-invasive assessment of the cell size in AT exists. This dissertation presents two different methods for a non-invasive measurement of adipocyte size and an additional method to reduce artifacts from which both presented adipocyte size measurements could potentially benefit.

3 Magnetic Resonance in Medicine

The physical background provided here, lays the foundation for the technical developments in the present dissertation. Part of the theory part was also used in the unpublished master thesis "Development of a B_1- and B_0-insensitive T_2 mapping method based on a modified BIR-4 T_2 prepared 3D TSE" by Dominik Weidlich.

3.1 Nuclear Magnetic Resonance

Nuclear magnetic resonance (NMR) was independently discovered by Bloch [56] and by Purcell [57] in 1946. The two scientists observed a detectable signal after placing a sample in a magnetic field and irradiating it with radio frequency (RF) energy at a certain frequency. Hence, they observed a signal that was created by the interaction of the sample and the magnetic field which is the basis of NMR. Magnetic Resonance Imaging (MRI) and Magnetic Resonance Spectroscopy (MRS) both employ the mechanism of NMR and measure the signal of hydrogen atoms (^1H) or other nuclei with non-zero spin in the human body.

3.1.1 Nuclear Spin and Magnetic Moment

The nuclear spin is a quantum mechanical property that is the basis of the NMR effect. The nuclear spin is an intrinsic property of particles and is associated with an inherent angular momentum ($\vec{J}$). In a clinical MR scanner, predominantly the signal of hydrogen atoms is measured. However, NMR measurements are possible with all atoms possessing a non-zero spin [58]. In 1922, O. Stern and W. Gerlach discovered in their famous experiment the presence of a quantized angular moment in silver atoms [59]. This was the first experimental proof for existence of the nuclear spin. A fundamental relationship connects the spin angular momentum ($\vec{J}$) with the nuclear magnetic moment ($\vec{\mu}$) :

$$\vec{\mu} = \gamma \vec{J} \tag{3.1}$$

where γ is the gyromagnetic ratio and is characteristic for every nucleus (equal to 2.675 $10^8 \frac{rad}{Ts}$ for the hydrogen atom). Since the magnetic moment is a vector, it has two distinct properties: a magnitude and a direction. Although the magnitude of the magnetic moment is known, the direction of the vector is random due to thermal motion. However, in the presence of a static magnetic field (B_0), the component in the direction of the field gets determined and is characterized by a discrete set of possible eigenstates. The magnetic moment perpendicular to the magnetic field (in the transverse plane) stays undetermined.

3.1.2 Spin System in the Presence of a Static External Magnetic Field

Because of the very small magnetic moment of a single spin, it makes sense to consider an ensemble of magnetic spins and utilize statistical measures to obtain a net magnetization. The bulk magnetization $\vec{M}$ is defined as:

$$\overrightarrow{M} = \sum_{n=1}^{N} \overrightarrow{\mu} \qquad (3.2)$$

With a sufficient large number of spins and without an external magnetic field, the net magnetization is zero, due to the random orientation of the spins. In a static external magnetic field, the total population of spins splits in subsets with different energy because the nuclear magnetic moment within the direction of the field is quantized. In a spin-1/2 system (like the hydrogen atom) this so-called Zeemann splitting leads to two energy levels. [60] The energy difference (ΔE) is given by the following equation:

$$\Delta E = E_\downarrow - E_\uparrow = \gamma \frac{h}{2\pi} B_0 \qquad (3.3)$$

Hereby $E_\downarrow$ is the energy of the spin-down energy level, $E_\uparrow$ is the energy of the spin-up energy level, h is the Planck constant and B_0 is the strength of the main magnetic field. According to the fundamental law of thermodynamics of statistical mechanics [61] and some approximations the magnitude of the magnetization can be described with the following equation:

$$|\overrightarrow{M}| \approx \frac{(\gamma \frac{h}{2\pi})^2 B_0 N}{4 k_B T} \qquad (3.4)$$

In this equation N is the number of spins, k_b is Boltzmann's constant and T is the temperature in Kelvin.

Equation 3.4 indicate that a net magnetization will be formed in the direction of the magnetic field when a substance with non-zero spin is placed in a static magnetic field. The magnitude of the magnetization is proportional to the amplitude of the magnetic field and the number of spins present in the sample and inversely proportional to the temperature of the system.

However, the induced magnetization is static and in the direction of an usually strong magnetic field. Therefore, it is not possible to induce a current in a receiver coil to produce a measurable signal. Consequently, it was proposed to utilize additional time-varying magnetic fields to rotate the magnetization away from the main magnetic field axis. [58]

3.1.3 Interaction between Magnetization and Time-varying Magnetic Field

According to the classical theory of electromagnetism a magnetization within a magnetic field will experience a torque [62]:

$$\frac{d\overrightarrow{M}}{dt} = \gamma (\overrightarrow{M} \times \overrightarrow{B}) \qquad (3.5)$$

That implies that the magnetization will rotate around the main magnetic field ($\overrightarrow{B_0}$) with the characteristic Lamor frequency (ω_0):

$$\overrightarrow{\omega}_0 = \gamma \overrightarrow{B} \qquad (3.6)$$

Without loss of generality it is assumed that the static main magnetic field is in the z-direction whereas the time-varying magnetic field ($\overrightarrow{B}_1(t)$) is in the transverse plane perpendicular to the main magnetic field:

$$\frac{d\vec{M}}{dt} = \gamma(\vec{M} \times (B_0\hat{z} + B_1(t)\hat{xy})) \tag{3.7}$$

Usually the time-varying field $\vec{B}_1(t)$ is realized by a sinusoidal modulation function with a certain frequency ω and a constant amplitude. By using a coordination transform, the time dependency $\vec{B}_1(t)$ can be eliminated. Also an effective field ($\vec{B}_{eff}$) can be introduced to increase readability. With these adjustments, the previous equation reads as follows:

$$\frac{d\vec{M}}{dt} = \gamma(\vec{M} \times ((B_0 - \frac{\omega}{\gamma})\hat{z} + B_1\hat{xy})) = \gamma(\vec{M} \times \vec{B}_{eff}) \tag{3.8}$$

If the frequency of $\vec{B}_1(t)$ is equal to the Lamor frequency, the spins can be excited on resonance. According to this equation, the magnetization can be manipulated by a time-varying magnetic field in the transverse plane with the appropriate frequency. [63]

3.1.4 Relaxation Times

As described in the previous section, the magnetization can be disturbed from its equilibrium state due to time-varying magnetic fields. After the excitation, the spin ensemble tends to relax back to the state of lowest possible energy. Such a relaxation process was first described by Bloch in 1946 [56]. In his publication, Bloch distinguished between two possible relaxation mechanism. In the first process, the spins are interacting with their environment, the lattice. By the so-called spin-lattice relaxation (or T_1 relaxation), the total energy of the spin ensemble changes. This is the essential process for the spins to return to their equilibrium magnetization and is therefore affecting the longitudinal magnetization component. The relaxation process of the spins can be described with the following equation:

$$M_z(t) = M_0(1 - e^{-t/T_1}) \tag{3.9}$$

with M_0 as the equilibrium magnetization and T_1 as the longitudinal or spin-lattice relaxation time.

The second process is the loss of coherence between single spins refered to as dephasing. During this relaxation phenomenon, energy is exchanged between spins whereas the total energy of the spin system does not change. The so-called spin-spin relaxation (or T_2 relaxation) will lead to a decay of the magnetization vector in the transverse plane and can be described with the following equation:

$$M_{xy}(t) = M_{ex}e^{-t/T_2} \tag{3.10}$$

here M_{ex} is the magnetization that is present in the transverse plane right after the excitation and T_2 is the transverse or spin-spin relaxation time.

In a real life scenario local field inhomogeneities within the sample exist, that lead to slightly different rotation frequencies of the spins within a volume of interest. The different rotation frequencies represent an additional source of dephasing and lead to a faster decay of the signal. The effective observed decay can be described with the parameter T_2^* and is the combination of the spin-spin relaxation and the additional reversible dephasing effect due to local field inhomogeneities. T_2 and T_2^* can be connected with the additional parameter T_2' (representing the local field inhomogenity term) according to the following equation:

$$\frac{1}{{T_2}^*} = \frac{1}{T_2} + \frac{1}{T_2'} \tag{3.11}$$

with

$$\frac{1}{T_2'} = \gamma \Delta B_{inhom} \tag{3.12}$$

In this equation ΔB_{inhom} is the field inhomogenity across the acquisition voxel. In contrast to the statistical energy exchange process of the spin-spin relaxation, the signal decay due to T_2' is reversible.

The discovery of different relaxation constants in different types of tissues is key to the success story of MR in modern medicine [64]. Due to these phenomena, different tissue types can be discriminated leading to the high soft-tissue contrast provided by MR measurements.

3.1.5 Bloch Equations

Combining the electromagnetic description of the interaction of the magnetization with the effect of relaxation, Bloch introduced his famous description of temporal evolution of the magnetization vector in 1946 [56]:

$$\frac{dM_x}{dt} = \gamma(\vec{M} \times \vec{B}_{eff})_x - \frac{M_x}{T_2} \tag{3.13}$$

$$\frac{dM_y}{dt} = \gamma(\vec{M} \times \vec{B}_{eff})_y - \frac{M_y}{T_2} \tag{3.14}$$

$$\frac{dM_z}{dt} = \gamma(\vec{M} \times \vec{B}_{eff})_z - \frac{M_0 - M_z}{T_1} \tag{3.15}$$

The three equations allow a simple classical description of the net magnetization vector. It is a useful framework that does not rely on complex quantum mechanical calculations. In a standard MR experiment the magnetization in the transverse plane is measured. Thereby, first of all, the magnetization vector needs to be excited by a time varying magnetic field, the so-called radiofrequency (RF) pulse. Afterwards, the magnetization is manipulated to achieve a distinct weighting of the signal. The weighting of the signal eventually leads to a perceptible contrast in the obtained imaging data between structures of interest. In the clinical routine e.g. T_1-weighted or T_2-weighted acquisitions are often employed. As a last step the signal is obtained by measuring the electric current induced in a nearby coil due to Faraday's law. In the following section basic elements for the signal generation as well as the reconstruction of the data will be presented.

3.2 Generation of a Magnetic Resonance Signal

The MR signal is generated by a combination of RF pulses and gradients. The assembly, properties and timings are defined in a so-called pulse sequence. A variety of different pulse sequences tailored to research and clinical questions exist. Although the exact appearance of the different pulse sequences may differ, they all share basic elements to generate a measurable signal. In the subsequent section these basic pulse sequence building modules will be described.

3.2.1 Free Induction Decay

The simplest way to measure the signal from an MR experiment is the utilization of a 90° RF pulse with a subsequent acquisition period (shown in Figure 3.1). With the 90° RF pulse, the magnetization that was previous aligned on the longitudinal axis is flipped to the transverse plane. This will lead to a magnetization vector that is precessing in the transverse plane and will induce a measurable electric current in the receiver coil elements that are arranged perpendicular to the main magnetic field.
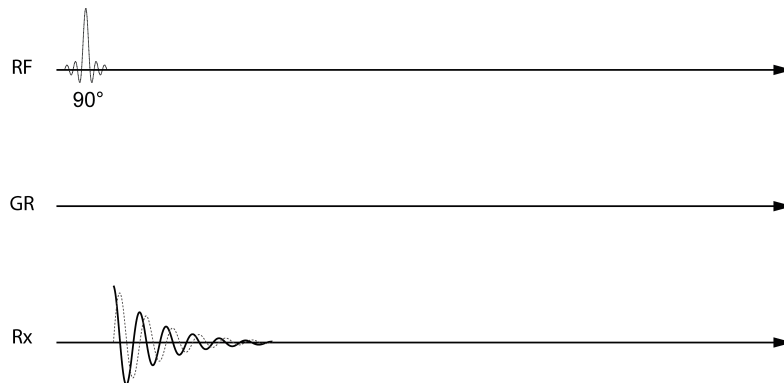
Figure 3.1: Free Induction Decay (FID): After the excitation RF pulse, the spins are dephasing and the magnetization is rotating in the transverse plane. The FID shows the rotation in the transverse plane with a simultaneous reduction of amplitude. The real and imaginary part are shown as a solid black and dotted gray line, respectively. RF: Radiofrequency pulse; GR: Gradient axis; Rx: Receiver channel

The amplitude of the magnetization vector will decay without the influence of other elements in the pulse sequence (with the relaxation time T_2^*) and therefore the experiment is called free induction decay (FID). The FID constitutes the most basic principle to acquire an MR signal. [65]

3.2.2 Gradient Echo

Another possibility to acquire an MR signal is the so-called gradient echo. In the simplest form it consists of an RF pulse and two gradients (shown in Figure 3.2).

Directly after the excitation, the magnetization is dephased by the first applied gradient. The second gradient has an area twice as large as the first gradient, an opposite polarity and will be applied afterwards. At the time point when the area of the first gradient is equal to the area of the second gradient, the magnetization is rephased. This time point is denoted as the echo time (TE) and the gradient echo is formed. After the formation of the echo, the magnetization is dephased again. The maximum amplitude of the formed echo acquired at different TEs decays with T_2^*. The presence of the gradient during echo formation has the advantage that it can be used for spatial encoding (please refer to chapter 3.4.2 for more details). [58]
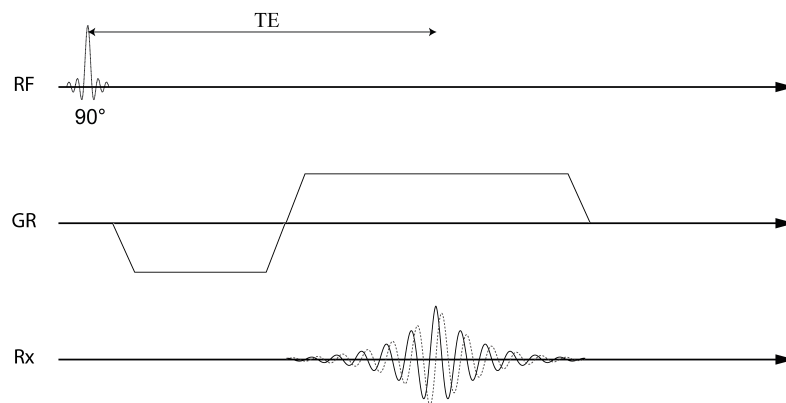
Figure 3.2: Gradient Echo: The first gradient with negative polarity after the excitation RF pulse causes a dephasing of the spins. The additional dephasing is recovered with the second gradient with opposite polarity, when the time integral of both gradient match. At this time point (TE) the echo is generated. The dephasing free induction decay after the excitation pulse is not shown. The real and imaginary part are shown as a solid black and dotted gray line, respectively. RF: Radiofrequency pulse; GR: Gradient axis; Rx: Receiver channel

3.2.3 Spin Echo

Another way to generate an echo, is via an additional RF pulse added after the 90° RF pulse. In this experiment a 90° excitation and a subsequent 180° refocusing RF pulse are applied. After being flipped in the transverse plane the spins will dephase due to energy exchange with each other and due to static local field inhomogeneities. After a certain time period (denoted with $\frac{TE}{2}$) the refocusing RF pulse is applied leading to an inversion of the acquired phase. Due to the static nature of the local field inhomogeneities, the acquired phase due to field inhomogeneities will reduce after the phase inversion. At TE, the net phase accumulated due to field inhomogeneities is zero and a spin echo forms. The phase difference due to energy exchange between the spins cannot be resolved and therefore the amplitude of the echo is reduced by T_2 relaxation. [56]

A schematic representation of the spin echo is shown in Figure 3.3. The advantage of a spin echo in comparison to gradient echoes is the insensitivity towards local field inhomogenieties and the reduced signal attenuation due to relaxation effects. However, the necessity for more RF pulses can increase the RF energy and also the minimum TE of the sequence.

3.2.4 Stimulated Echo

With three 90° RF pulses a so-called stimulated echo can be formed. The echo formation process is similar to the one described for spin echoes but one more additional RF pulse is employed. After the first excitation 90° RF pulse the magnetization dephases in the transverse plane. After $\frac{TE}{2}$ the second 90° RF pulse is utilized to flip the magnetization back on the longitudinal axis. After a certain period of time, also referred as mixing time (TM), the last 90° RF pulse is employed and the magnetization is flipped back in the transverse plane. The
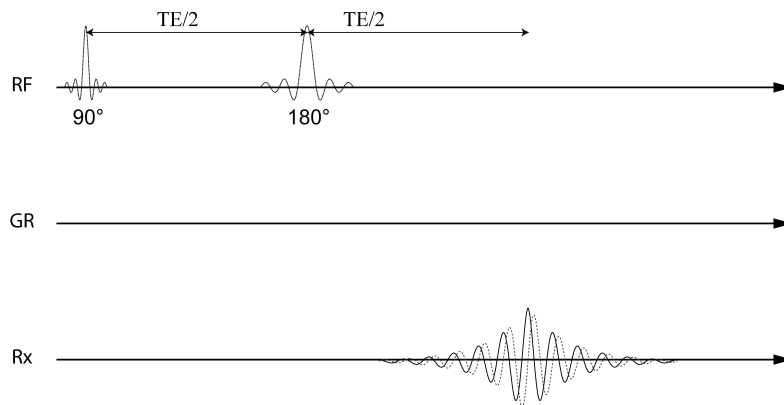
Figure 3.3: Spin Echo: The magnetization is flipped to the transverse plane. Afterwards, local field inhomogeneities induce a reversible dephasing of the spins. The dephasing can be recovered by an additional 180° RF pulse. The echo is formed at the time point TE after the spins are rephased. The free induction decay after the excitation pulse is not shown. The real and imaginary part are shown as a solid black and dotted gray line, respectively. RF: Radio-frequency pulse; GR: Gradient axis; Rx: Receiver channel

stimulated echo is formed after $\frac{TE}{2}$ (schematic overview of a stimulated echo is shown in Figure 3.4).

An unique characteristics of the stimulated echo formation process is that the amplitude of echo is weighted by T_1 as well as T_2 decay. Due to the special formation process half of the magnetization is lost. [66]

3.3 Chemical Shift in MR

Protons will experience differences in their electronic shielding depending on their chemical environment and consequently different local magnetic fields. Differences in the magnetic field can be directly mapped to different Lamor frequencies (compare equation 3.6). With this chemical shift property different moleculs can be distinguished with MR when the Lamor frequency in investigated.

3.4 MR Pulse Sequences

The basic elements described in the previous sections can be combined with one another and with additional RF pulses, gradients and acquisition periods to acquire the MR data. The acquired signals are then reconstructed and when applicable post-processed to give valuable clinical or research information. In general, two different types of MR pulse sequences are presently considered: the frequency resolved single-voxel MR spectroscopy which can be used to encode chemical shift information and the spatially resolved MR imaging sequence which can be used to encode spatial information in 2D or 3D.
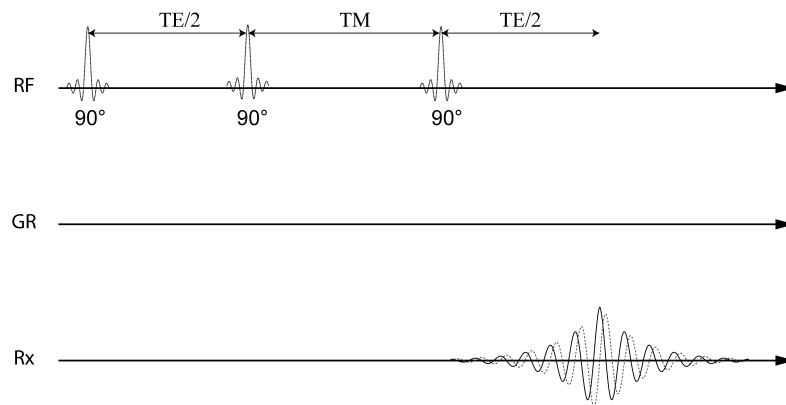
Figure 3.4: Stimulated Echo: After the application of three 90° RF pulses a stimulated echo is formed. The timing between the first and second, as well as the third RF pulse and the echo formation is denoted with $\frac{TE}{2}$. The timing between the second and the third RF pulse is called mixing time (TM). The free induction decay after the excitation pulses and possible occurring spin echoes due to imperfect RF pulses are not shown. The real and imaginary part are shown as a solid black and dotted gray line, respectively. RF: Radiofrequency pulse; GR: Gradient axis; Rx: Receiver channel

3.4.1 MR Spectroscopy

NMR offers the unique possibility to distinguish chemical species based on their chemical shift property. The acquired time-domain MR signal contains the contribution of all spins within the excited volume and can be directly translated via the Fourier transform to a spectrum in the frequency domain. In the spectral domain, different metabolites can be separated and their relative amplitude can be extracted. In simple molecules (like water), the resulting spectrum only consists of an unimodal distribution of resonances frequencies (one peak in the spectral representation). In larger molecules (like fatty acids), the spectrum is more complex, consisting of multiple spectral peaks. In such complex molecules, the protons can be located in different parts of the molecules resulting in different chemical environments. Pools of protons can be coupled (so-called J-couplings) which make a theoretical description rather difficult. However, the appearance of the acquired spectrum can be directly related to the chemical structure and offers therefore a high degree of information.

On a clinical MR system, spectroscopy is mostly acquired from a single volume of interest, the so-called voxel. The most frequently used single-voxel MRS techniques are point-resolved spectroscopy (PRESS) [67] and stimulated echo acquisition mode (STEAM) [68].

A PRESS sequence consist of a slice selective 90° excitation pulse and two additional slice selective 180° refocusing RF pulses. By employing three slice selective RF pulses a three dimensional localization of the voxel can be achieved. With this setup a twice refocused spin echo is generated and spoiler gradients can be employed to prevent undesirable alternative magnetization pathways due to imperfections of the employed RF pulses. In between the RF pulses the magnetization will decay with the relaxation constant T_2.

A STEAM sequence on the other hand consists of three slice selective 90° RF pulses generating eventually a stimulated echo. Spoiler gradients can be employed to prevent undesirable magnetization pathways like FIDs or spin echoes. The principle for generating the echo is shown in Figure 3.4 (omitting slice selective gradients). Between the first and the second RF pulse as well as between the third RF pulse and the echo, the magnetization decays with T_2. Whereas, during TM (between the second and the third RF pulse) the magnetization decays with T_1. Due to the generation process of the stimulated echo, 50% of signal amplitude is lost. However, this design allows shorter echo times and longer extend of the mixing time (because $T_1 > T_2$ in most cases).

Before converting it to an interpretable spectrum, the acquired data from the MRS sequence need to be pre-processed in order to reduce artifacts and increase the signal to noise ratio (SNR). These pre-processing steps can include coil combination, phase correction, apodization, frequency correction and additional possible correction steps. After this usually a time- or frequency-domain fitting is employed to extract the relative peak amplitudes for further interpretation or processing. [69]

The limited spatial information, complex reconstruction and post-processing as well as the non-trivial interpretation of the results, limits the use of single voxel spectroscopy in the clinical routine. However, in research settings MRS offers the unique possibility to spectrally resolve the information at different chemical shift locations and measure MR properties of individual chemical species. Thereby, MRS can be utilized in many cases as a gold standard measurement technique.

3.4.2 MR Imaging

For the clinical routine, spatially resolved images are essential. In 1973, Lauterbur [70] introduced the idea to use magnetic gradient fields in order to encode spatial information. In the presence of a magnetic field gradient, the Lamor frequency of the spins becomes spatial dependent and can be used to localize the origin of the acquired signal. When a magnetic field gradient is present that alters the amplitude but not direction of the main magnetic field, the local magnetic field is defined as follows:

$$\overrightarrow{B_G}(x,y,z) = \overrightarrow{B_0} + G_x(x)\overrightarrow{x} + G_y(y)\overrightarrow{y} + G_z(z)\overrightarrow{z} = \overrightarrow{B_0} + \overrightarrow{G} \cdot \overrightarrow{r} \tag{3.16}$$

With local dependency of the magnetic field, also the frequency of the rotating spins becomes spatially dependent:

$$|\overrightarrow{w}(\overrightarrow{r})| = \gamma(|\overrightarrow{B_0}| + \overrightarrow{G} \cdot \overrightarrow{r}) \tag{3.17}$$

Without loss of generality and for simplicity it can be assumed that only a gradient in the x direction is present. Without relaxation effects, the incremental signal (dS) generated by spins within the interval x and $x + \Delta x$ is:

$$dS(x,t) \propto \rho(x) \ dx \ e^{-i\gamma(B+G_x x)t} \tag{3.18}$$

where $\rho(x)$ is the spin density (the target quantity that should be extracted from the MR experiment) and t is the time. The total signal can be retrieved by integrating over the x-dimension:

$$S(t) = \int_{-\infty}^{\infty} dS(x,t)dx \propto \int_{-\infty}^{\infty} \rho(x) \ e^{-i\gamma(B+G_x x)t}dx \tag{3.19}$$

As a next step, the Lamor frequency can be demodulated from the signal and a new constant k can be introduced:

$$k_x = \frac{\gamma}{2\pi} \int G_x(t)dt \tag{3.20}$$

The total signal now writes as follows:

$$S(t) \propto \int_{-\infty}^{\infty} \rho(x) \; e^{-i2\pi k_x x}dx \tag{3.21}$$

The structure of this equation is identical to a Fourier Transform and therefore the well-known calculation rules can be applied to retrieve the spin density $\rho(x)$:

$$\rho(x) \propto \int_{-\infty}^{\infty} S(k(t),t) \; e^{-i2\pi k_x x}dk_x \tag{3.22}$$

Based on this relation the spin density can be obtained by a Fourier Transform of the acquired signal. The newly introduced variable k is the Fourier conjugate variable of the image space variable x. Therefore, in order to spatially encode an MR image, data for different values of k is acquired and afterwards the acquired data is Fourier transformed.

Three dimensional image data can be either extracted by extending the spatial encoding process to more than one dimension or by utilizing slice selective RF pulses.

There is a large variety of possible pulse sequences for MRI differing in their mechanism for signal generation, additional elements to manipulate the magnetization and exact sequence parameters. The respective pulse sequence depends on the clinical or research questions and is resulting in MR images with different contrast weightings. Frequently used imaging sequences in the clinical routine are for example Echo Planar Imaging (EPI) [71] and Turbo Spin Echo (TSE) [72].

3.5 Hardware in Clinical MR Systems

A modern MR scanner is a technical complex and marvelous machine. It consists of a variety of hardware and software components and must be embedded in a modern infrastructure in order to ensure the acquisition of clinically useful data. Describing the setup of a MR scanner in detail would be beyond the scope of this dissertation. Therefore, only the three most important components will be described in the following.

3.5.1 Magnet

The main magnetic field ($\overrightarrow{B_0}$) needed to polarize the spins within the investigated object can be either obtained by a electromagnet or a permanent magnetic material. Modern clinically used whole body MR systems mostly rely on electromagnets with helium-cooled superconducting coils in order to generate a stable and high static magnetic field. Scanner with a main magnetic field strength of $1.5\,\text{T}$ and $3\,\text{T}$ are routinely used in the clinical environment. High field MR systems like $7\,\text{T}$ scanners are less common and mostly used in research settings. For high quality MR data, a homogeneous magnetic field is essential. This can be achieved by additional correcting magnetic fields called shimming gradients. Because the strong main magnetic field is permanently active, it causes a major danger in an MR facility. Restricted access, screening for metal and shielding can limit the occurrence of accidents. [73]

3.5.2 Radio Frequency Transmit and Receive Coils

As described earlier a time-varying magnetic field is necessary to manipulate the magnetization within the sample. The $\overrightarrow{B_1}$ RF field is generated by transmit RF coils with a frequency similar to the Lamor frequency of the investigated spins. Thereby, the field strength is orders of magnitude lower than the main magnetic field (on a clinical system in the order of 10th of µT). The measurable signal is generated within the subject itself and will be detected by receiver coils. Because of the relatively small amplitude of the $\overrightarrow{B_1}$ RF field and the irritated signal, the MR scanner is placed in a Faraday cage to prevent interaction of the system with surrounding electromagnetic fields. Specific transmit or receive coils can be constructed but it is also possible to produce combined receive and transmit coils. In most clinical MR scanners, a large body coil is built-in that is capable to receive and transmit RF signals. More dedicated RF receive coils are additionally used to increase the SNR and enable parallel imaging techniques. [58]

3.5.3 Gradient Coils

Gradients are an essential component in the MR system to manipulate the magnetization and enable spatial encoding. This is possible by applying additional magnetic fields that enforce a spatial variation of the amplitude (not the direction) of the main magnetic field. The magnetic gradient fields are produced by mostly built-in gradient coils and controlled by varying the strength of the electric current inside them. [70] Many pulse sequence designs require very fast and rapid changes of the gradient field amplitudes. Rapidly changing a current in strong magnetic field induces Lorentz forces on the gradient coil. Therefore, during an MR examination usually a loud tapping, clicking or high pitched beeping sound can be heard. [74] Increasing the strength of a gradient in general permits scanning with higher resolution, faster acquisition or stronger diffusion weighting. However, the acoustic noise increases with the increasing gradient strength and artifacts induced by hardware vibrations can mitigate the measurement quality.

3.5.4 Experimental Setup

All experiments of the present thesis were performed on clinical whole-body 3 T MRI scanners (Ingenia, Philips Healthcare, The Netherlands) at the University Hospital Klinikum rechts der Isar of the Technical University of Munich in Munich (Germany).

4 Assessment of Tissue Microstructure with Magnetic Resonance

DW-MR is a powerful tool for the non-invasive assessment of tissue microstructure. By investigating the movement of spins within a certain tissue, information about the particle mobility and the structural properties of biological systems can be extracted. Therefore, MR is a unique technique that is capable to extract next to the macroscopic anatomical information also information at the microstructural level. DW-MR is not only widely used in the clinical settings (most predominantly in oncology settings or to identify brain ischemia) [75, 76], but also in research settings as for example in assessing brain network connectivity [77].

4.1 Principles of Diffusion

According to Adolph Fick, diffusion can be defined as the microscopic flux of particles in a medium resulting from a gradient in the particle concentration [78]. In 1905, Albert Einstein proposed that also self-diffusion (without the necessity of a macroscopic concentration gradient) can lead to particle flux [79]. In his explanation, the movement of particles results from local concentration fluctuations caused by Brownian motion. This microscopical effect can be described with statistical measures. For 3D self diffusion Einstein's famous equation of diffusion reads as follows:

$$< X >^2 = 6D\Delta \tag{4.1}$$

where $< X >^2$ is the average squared distance traveled by an particle due to diffusion in a given period of time Δ, referred to as the diffusion time. D is the diffusion coefficient and represents the mobility of the particles.

4.2 Measuring Diffusion Effects with MR

DW-MR has the unique capability to non-invasively characterize the effect of the microscopic particle motion on the measured signal while employing large voxels at the macroscopic scale. The effect of diffusing spins can be made visible by applying magnetic field gradients in a special fashion.

In general an applied gradient will lead to a spatial dependency of the Larmor frequency (refer to equation 3.17). For a moving spin in a magnetic gradient field, the Larmor frequency becomes time dependent because the local magnetic field will change according to the position of the spin. Therefore, the overall accumulated phase (φ) excluding the contributions of the main magnetic field at time t can be described as follows:

$$\varphi(t) = \int_0^t \omega(t')dt' = \gamma \int_0^t \overrightarrow{G}(t') \cdot \overrightarrow{r}(t')dt' \tag{4.2}$$

The signal S of a macroscopic ensemble of spins is equal to the integral over the volume of interest with consideration of the phase of each single spin:

$$S(t) \propto \int e^{i\varphi(\vec{r},t)} d\vec{r} \tag{4.3}$$

Only if all spins have acquired exactly the same phase during the MR experiment, the magnitude of the signal will not be attenuated. When a magnetic field gradient with a sufficient strength is applied over the volume of interest, this is only possible when the spins are not moving or all moving with equal velocity and the time integral over the magnetic field gradient is zero. When the spins are diffusing, the statistical random motion induces a phase dispersion of the spin ensemble that is not recoverable and leads eventually to signal loss. Already in 1950, Hahn discovered in his initial works on echo formation that diffusion is an effect that leads to signal attenuation that cannot be resolved by rephasing of spins with an refocusing RF pulse [66]. In summary: Diffusion is a process that due to its random motion leads to signal attenuation. The applied pulse sequence needs to be sensitive towards the particle motion by applying magnetic field gradients. Eventually, regions with static spins will be brighter compared to regions with fast diffusing spins on a DW MR image.

There are various approaches to design a pulse sequence with appropriate DW gradient schemes. Most commonly used is the original proposal by Stejskal and Tanner, employing a spin echo with one diffusion sensitizing gradient after each RF pulses, the so-called Pulsed-Gradient Spin-Echo (PGSE) gradient waveform [80].
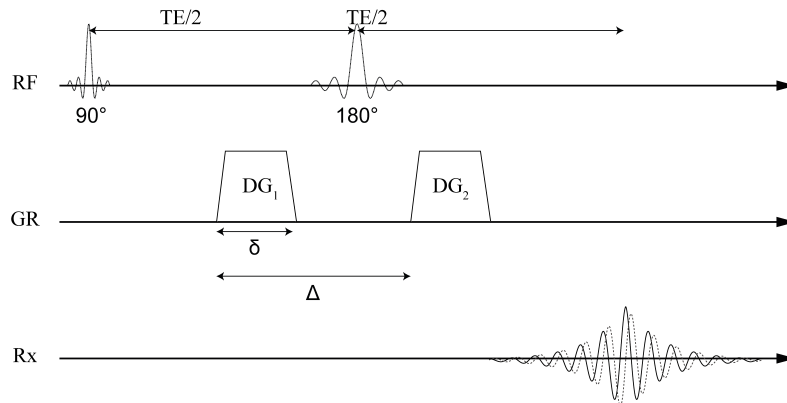

Figure 4.1: Pulsed-Gradient Spin-Echo: Diffusion sensitizing experiment proposed by Stejskal and Tanner [80]. The echo is generated by a spin echo and the applied gradients (DG_1 and DG_2) which sensitize the sequence towards diffusion. The time interval Δ is equal to the diffusion Time and δ is the length of the diffusion gradient. The free induction decay after the excitation pulse is not shown. The real and imaginary part are shown as a solid black and dotted gray line, respectively. RF: Radiofrequency pulse; GR: Gradient axis; Rx: Receiver channel; TE: echo time

Figure 4.1 shows a schematic view of the traditional PGSE sequence. After the excitation pulse the spins get dephased by the first diffusion gradient. Due to the refocusing RF pulse the acquired phase of the spins gets inverted and therefore the second diffusion gradient

serves as a rephasing element. For static spins, no additional signal decay except relaxation effects will attenuate the echo at time point TE. For diffusing spins, the arrangement of the gradient will lead to phase dispersion and eventually signal loss. The amount of attenuation depends on the diffusion gradient area (depending on the diffusion gradient length δ and strength), the diffusion time (Δ) and the mobility of the particles. More complex gradient waveforms and DW sequences have been proposed and tailored to specific problems. For example, motion compensated waveforms have been proposed to null the influence of specific movements of the spins [81]. Additionally, diffusion experiments based on a stimulated echo sequence were proposed allowing the acquisition of very long diffusion times [82]. On the other hand oscillating gradient schemes allow the realization of very short diffusion times [83].

The amount of DW can be summarized in a parameter called b-value [84, 85]. Utilizing the b-value formulation equation 4.3 can be written as follows:

$$S(b) = S_0 e^{-bD} \tag{4.4}$$

S is the measured signal, S_0 is the signal without diffusion attenuation, D is the diffusion constant and b is the b-value. The b-value is a mathematical construction to represent the degree of DW of a certain sequence and is defined as follows:

$$b = \gamma^2 \int_0^{TE} [\int_0^t G(t')dt']^2 dt \tag{4.5}$$

In this equation the gradient strength G is integrated twice over time. Here, only the one dimensional case is shown, although the applied gradient also has a certain direction. The diffusion sensitivity of the sequence is always in the direction of the applied gradient. By applying the DW in different directions, directional differences in the diffusivity of the particles can be investigated.

In a simple PGSE sequence equation 4.5 can be written in a simpler form [86]:

$$b = \gamma^2 G^2 (\delta^2(\Delta - \frac{\delta}{3}) + \frac{\epsilon^3}{30} - \frac{\delta\epsilon^2}{6}) \tag{4.6}$$

Hereby, ϵ represents the ramping time of the trapezoidal gradients. The b-value formulation simplifies the description and comparison of different DW MR pulse sequences. For that reason, this formulation is often used in clinical practice and research settings.

The unit of the b-value is commonly denoted in $\frac{s}{mm^2}$ and usually b-values up to 1000 $\frac{s}{mm^2}$ are applied in the clinical setting to investigate the diffusion of water.

In DW-MR, the measured diffusion constant is influenced by many different parameters. Therefore, often the term apparent diffusion constant (ADC) is used when diffusion properties are measured with MR.

4.3 Pulse Sequences for DW-MR Measurements

To encode the DW signal based on the principles described in the previous chapter, different specialized MR-pulse sequences are used. The upcoming chapter gives a brief overview of the most often applied sequences. Artifacts that arise from the diffusion enocding process are described in more detail in section 4.4.

4.3.1 EPI-based DW-MR Pulse Sequences

The most commonly applied DW-MR pulse sequence in the clinical setting is the single-shot DW-EPI sequence. Single-shot DW-EPI offers the possibility of a SNR efficient readout by acquiring the whole k-space after one acquisition. Thereby, the sequence does not suffer from phase errors that differ between each excitation and the measurement can be considered as rather insensitive to motion. However, due to the low bandwidth in the phase-encoding dimension, the spatial resolution and coverage is limited. Furthermore, the acquired images can suffer from distortions induced by off-resonance effects.[87] Besides the inherent problems and image artifacts, the sequence can be considered as the working horse sequence for clinical brain DW imaging.[88]

However, when higher resolutions/coverage is required or stronger B_0 inhomogeneities are present (common in multiple body applications), single-shot DW-EPI might not be suitable. Higher resolutions can be achieved by only acquiring part of the k-space with each excitation (called multi-shot acquisition) and combining the segmented k-space parts in the reconstruction. However, in the DW acquisition, shot-to-shot phase errors can occur which corrupt the overall image quality.[89] Therefore, the phase errors in each shot need to be detected and the data should be corrected before combination of the k-space. The bandwidth in the phase-encoding dimension can be also increased with multi-shot EPI acquisions (thereby reducing the geometrical distortions) but the acquisition is also slower compared to the single shot variant of DW-EPI.[88]

4.3.2 TSE-based DW-MR Pulse Sequences

An alternative to the EPI-based readout is a spin-echo based acquisition like TSE. It has the advantage of not suffering from geometrical distortions induced by susceptibility and chemical shift because the magnetization gets refocused at echo acquisition. However, this big advantage comes with the necessity to apply multiple refocusing pulses which decreases the SNR efficiency of the sequence compared to EPI. Therefore, longer acquisition times are necessary and also more RF energy (heat) is deposited in the patient. [88] Additional to that, TSE sequences need to fulfil the Carr-Purcell-Meiboom-Gill (CPMG) condition which states the phase of the refocusing pulses matches the phase of the rotating spins creating magnetization [90]. This can in general not be archieved easily in the context of DW, because the accumulated phase of the magnetization is unknown. This violation of the CPMG condition can be avoided when magnitude stabilizing gradients are introduced. With this technqiue a uniform phase distribution is generated over each voxel (independent of the signal phase) but also half of the signal is lost [91].

The TSE acquisition can also acquire the k-space of one slice in a complete or segmented fashion. With the single-shot acquisition (to reduce T_2 blurring effects), the sequence is again limited to lower resolution scans but does not suffer from shot-to-shot phase errors. Similar to DW-EPI, also DW-TSE sequences can be extended to a multi-shot acqisition, but then phase navigation of each shot is necessary [92].

4.3.3 Spectroscopy-based DW-MR Pulse Sequences

Acquiring DW-MRS data is nowadays mostly applied in research settings. Due to the capability of spectroscopy to spectrally resolve the acquired data, it is possible to investigate the diffusion properties of distinct chemical species. This offers great potential in the detailed

investigation of neurotransmitters in brain research [93] but can also be applied to investigate the properties of fat [94]. As already shown in section 3.4.1, the most dominant single voxel MRS sequences are PRESS and STEAM. In both sequences DW gradients can be introduced to allow DW of the spectrum. A DW-PRESS sequence has the advantage of allowing high SNR but also suffers from a large chemical shift displacement artifact. Also, the diffusion time of the signal can only be increased by increasing TE which will lead to a strong attenuation due to T_2 relaxation. With a DW-STEAM sequence half of the signal is lost due to echo generation process. However, this sequence allows shorter echo times and reduced chemical shift displacement artifacts. In this setup the diffusion time can be increased by changing the mixing time which will lead to a signal attenuation by T_1 relaxation. [69]

With a DW-MRS sequence very rich information can be obtained from one location and the diffusion properties can be investigated in great detail. However, the application of DW-MRS stays a niche application due to its limited availability on clinical MR scanners, the partly complex processing and interpretation in combination with inherent artifacts that are characteristic to the diffusion encoding process.

4.4 Artifacts Due to the Diffusion Encoding Process

Due to the specific mechanism to generate contrast in DW-MR measurements, there are several characteristic artifacts that can occur in these type of measurements. The upcoming chapter describes the most prominent sources for measurement errors in DW-MR. Avoiding these artifacts or mitigating the effect can improve data quality and lead to a more accurate and robust estimation of quantitative parameters extracted from DW measurements.

4.4.1 Eddy Currents

Artifacts due to eddy currents are common in DW measurements because of the necessity to have diffusion gradients with short duration and large gradient strength. The fast switching of the magnetic field gradients introduce additional undesired electric currents within nearby conducting structures that in turn produce their own magnetic fields. The additional magnetic fields distort the theoretical ideal gradient form and can lead to unwanted effect in the measurement. [95]

The effect of eddy currents on DW measurements is particularly visible in geometrical distortions of clinically often employed DW single-shot EPI sequences. Hereby, the remaining gradients due to eddy currents are still present during spatial encoding and lead to image distortions [96].

The geometrical distortions can be mitigated when instead a TSE readout is employed [91]. The eddy current induced deviation from the ideal gradient wave form can also lead to undesirable phase accumulation after diffusion encoding. When a diffusion preparation module (with a tip-up RF pulse after diffusion encoding) is used this can lead to spatial varying errors of the magnitude and phase of the DW signal. An elegant way of eliminating the effect of eddy current induced phase errors is the employment of magnitude stabilizers in the DW preparation and readout [97].

In DW-MRS sequences eddy currents from the DW gradients can lead to an additional eddy current phase distorting the spectral peaks. By acquiring a DW STEAM sequence with two polarities of the DW gradients, the eddy current phase can be estimated and removed in a post-processing step. [94]

4.4.2 Gradient Non-linearity

Deviations from the ideal gradient field can cause artifacts: The equations shown in chapter 4.2 assume a spatially constant slope of the magnetic field gradient. However, it was observed by studying the diffusion properties of ice water that this assumption is only true close to the gradient coil center [98]. Due to hardware limitations, the magnetic field gradient will deviate from the theoretical linear behavior in outer parts of the gradient coil center, resulting in lower or higher gradient strength compared to the nominal gradient strength. This can lead to a weaker or stronger DW and eventually to measurement errors when diffusion properties are quantified [99]. The effect of gradient non-linearities can be either mitigated by focusing the analysis on regions close to the iso-center, adjustments on the gradient hardware or by incorporating knowledge about the spatial variation of the DW due to gradient non-linearity effects in the processing of the acquired data [100].

4.4.3 Motion-induced Phase Errors

Especially when DW measurements are performed in vivo, tissue motion is mostly inevitable. The motion can be on the one hand physiological due to breathing or cardiac pulsation or on the other hand induced by voluntary or involuntary bulk motion of the subject. Any type of macroscopic motion during the diffusion encoding process can lead to signal cancellation also known as intravoxel dephasing. The additional motion during DW leads to accumulated phase of the spins. If a non-zero phase remains at signal acquisition and there is a spatial variation in the accumulated phase, this will eventually lead to signal loss. This strength of the signal cancellation scales with the DW strength and the acquisition voxel size. Intravoxel dephasing induced by macroscopic motion does not reflect the microscopic self-diffusion of the spins and therefore does not contain microstructural information. [101] There are several strategies proposed to mitigate the effect of the unwanted motion-induced phase: First the right selection of the pulse sequence and pulse sequence parameters can reduce the sensitivity towards motion [102]. Second, specific gradient waveforms can be designed to be insensitive towards specific types of motion (e.g. movement of spins with a constant velocity) [103, 104]. Third, as a last option, physiological triggering (e.g. respiratory or cardiac triggering) can help to identify phases in recurring motion patterns that are not characterized by large tissue movements. The acquisition of data can then be limited to these "quiet" time intervals. [105]

4.4.4 Vibration-induced Artifacts

Artifacts induced by vibrations can be considered as a specific case of motion-induced phase errors. As described in section 3.5.3, fast switching gradients can introduce acoustic noise and scanner hardware vibrations. Especially, DW gradients that usually have a high amplitude, were shown to yield large displacements of the MR scanner table [106]. The hereby observed vibrations are so strong, that they were even proposed as a driving force for MR elastography experiments [107]. In the context of DW measurements, it can be observed that these vibrations have an influence of the measured signal due to intra-voxel dephasing effects described in the previous chapter. In a standard DW sequence the following scenario can easily become reality: Vibrations induced by the first diffusion gradient have little influence during the first diffusion gradient but will change the displacements of the scanned object during the second diffusion gradient. Therefore, the accumulated phase in both DW periods is different which leads to the before mentioned phase dispersion. Larger voxel sizes and

also stronger diffusion gradients will increase the severity of the observed signal loss. [101] Vibrational artifacts on DW data, have already been reported in clinical data. In high b-value Diffusion Tensor Imaging (DTI) the artifact becomes visible in posterior brain regions that are close to the scanner table and lead to signal loss in the diffusion weighted raw data and quantification errors in the parameter maps extracted from the DTI processing [108, 109]. The severity of the artifacts could be reduced by hardware adjustments to reduce the amplitude of the vibrations or by finding a way to make the vibration pattern more similar during both diffusion weighting periods. In JP-II a method to mitigate signal loss induced by vibrations is described. Artifacts like this are especially severe if high order effects like diffusion restriction are measured because small changes on the signal can have large effects on the quantification process.

4.5 Diffusion Restriction Effects

Without any restricting barriers the observed particles can diffuse freely. This is reflected by a mono-exponential diffusion decay signal acquired at different b-values and a constant ADC value for different diffusion times. Within biological tissue, the free movement of the particles can be influenced by diffusion restriction barriers and consequently the DW signal behavior deviates from the free diffusing case.

4.5.1 Diffusion Regimes

Already in 1973, J. E. Tanner observed a dependency of the diffusion constant on the diffusion time. In his work, he investigated water diffusion in frog muscles acquired with different pulse sequences to achieve different diffusion times. An oscillating gradient scheme combined with a spin echo leads to a short diffusion time, a simple PGSE sequence to an intermediate diffusion time and a pulsed gradient scheme with stimulated echo to a long diffusion time. [110]

Essential for the observed diffusion behavior is the relation between the mean free path length during the diffusion experiment and the restriction barrier size. If the mean free path length is much smaller than the restriction barrier size, the spins will diffuse in the short diffusion time limit. Hereby, only the spins close to the barrier will experience restrictions in their movement, whereas the majority of the spins will diffusive freely. In this regime there is barely a deviation in the mono-exponential signal decay visible, but the free diffusion constant will decrease with increasing diffusion time [111]. In the long diffusion time limit, the mean free path length is much larger then the restriction barrier size. In this scenario most of the spins come into contact with the restriction barrier (also multiple interactions are possible) during the diffusion experiment and therefore the mobility of most of the spins is hindered. In this regime deviations from the mono-exponential signal decay can be observed and the diffusion constant approaches to a fixed value with increasing diffusion time [112]. In between these two extreme cases an intermediate regime can be observed. Consequently, the observed signal decay and diffusion constant behavior will be different in different diffusion time regimes.

4.5.2 Modeling Diffusion Restriction Effects

Observing deviations from the free diffusion behavior of particles offers interesting implications and is therefore a very fascinating effect to study. It allows to draw conclusions about tissue properties on a cellular scale that are way beyond the usual resolution of a MR experiment.

Only a brief overview of the most important concepts to describe restricted diffusion will be given as a review of all the different modeling approaches would be beyond the scope of the present dissertation.

Deviations from the unrestricted free diffusion behavior were first observed by Woessner in the year 1963 in a qualitative fashion [113]. One of the first researchers to investigate restriction effects in a more detail have been Murday and Cotts [114]. They investigated the diffusion of liquid lithium and proposed an equation to describe the theoretical signal evolution for diffusion within spherical boundaries building up on ideas from Neumann [115]:

$$ln(\frac{S}{S_0}) = -2\gamma^2 G^2 \sum_{m=1}^{\infty} \left[\alpha_m^2 \left(\alpha_m^2 R^2 - 2) \right) \right]^{-1}$$
$$\left(\frac{2\delta}{\alpha_m^2 D_{free}} - \frac{2 + e^{-\alpha_m^2 D_{free}(\Delta-\delta)} - 2e^{-\alpha_m^2 D_{free}\delta} - 2e^{-\alpha_m^2 D_{free}\Delta} + e^{-\alpha_m^2 D_{free}(\Delta+\delta)}}{(\alpha_m^2 D_{free})^2} \right) \tag{4.7}$$

where d is the diameter of the spherical restriction barrier, D_{free} is the free diffusion constant, and α_m are the roots obtained by the following differential equation of Bessel functions (J):

$$\left(\alpha_m \frac{d}{2} \right) J'_{\frac{3}{2}} \left(\alpha_m \frac{d}{2} \right) - \frac{1}{2} J_{\frac{3}{2}} \left(\alpha_m \frac{d}{2} \right) = 0 \tag{4.8}$$

Equation 4.7 offers a description of the evolution of the signal for restricted diffusion within spherical boundaries. In general, diffusion restriction effects will lead to a decrease of the diffusion constant for increasing diffusion time and to deviations from the exponential signal decay. Despite the generality, the formalism proposed by Murday and Cotts is complex and the extraction of parameters is challenging.

Under certain assumptions the description of restricted diffusion can be simplified. As described in the previous section, the diffusion time is a key element to distinguish different regimes and allows the usage of certain simplifications. In the short diffusion time limit, most of the particles will diffusive freely, whereas only a small fraction of the particles (in close proximity to the restriction barriers) will experience a limitation in their mobility. The amount of particles experiencing restriction will increase with increasing diffusion time. Therefore, Mitra proposed to treat the problem as having two different pools: One particle pool that can diffusive freely and another particle pool that will experience restricted diffusion. Mitra proposed to investigate the diffusion constant which is a mean quantity originating from the behavior of both particle pools at different diffusion times. The idea is that with increasing diffusion time, the movement of more particles will be restricted and the measured mean diffusion constant is consequently decreased. The proposed experiment is sensitive towards the surface-to-volume ratio (A/V) and can be described with the following equation [111]:

$$D(\Delta) = D_{free}(1 - \frac{4}{9\pi} \frac{A}{V} \sqrt{D_{free}\Delta}) \tag{4.9}$$

where A is the surface of the restriction barrier and V is the volume of the restriction barrier. This equation indicates that measuring the diffusion constant for different diffusions times offers information about the tissue microstructure. When also a special geometry is assumed (e.g. spherical restriction barriers) microstructural parameters like the diameter of the restricting barrier can be extracted. This idea was first verified experimentally using

DW-MRS on sedimentary rocks [116, 117] and on large size beads [118]. The hereby described simplifications of the diffusion behavior are only valid when the diffusion length is much smaller then the restriction barrier size. In most clinical applications (focusing on fast diffusing water in small biological cells), the diffusion length is much larger or comparable to the restriction barrier size.

Therefore, oscillating gradients with high frequency are sometimes applied to reduce the effective diffusion time and to probe diffusion in the short diffusion time limit [119–121].

Because in most clinical examples for restricted diffusion, diffusion tends to be in the long diffusion time limit, there is a large variety of different methods to describe the long diffusion time regime. In 2002, Garasanin et al. proposed an approximation for equation 4.7 that is valid in the long and intermediate diffusion time regime. The approximation was archived by only considering the first term of the Bessel equation and reads as follows [122]:

$$ln(\frac{S}{S_0}) = \frac{54G^2(\frac{d}{2})^4\gamma^2}{15379D_{free}^2}$$

$$(3(e^{-\frac{52D_{free}(\delta-\Delta)}{3d^2}} - 2e^{-\frac{52D_{free}\delta}{3d^2}} - 2e^{-\frac{52D_{free}\Delta}{3d^2}} + e^{-\frac{52D_{free}(\delta+\Delta)}{3d^2}} + 2)(\frac{d}{2})^2 - 26D_{free}\delta) \tag{4.10}$$

When the diffusion length is much larger then the restriction barrier size, the particles are diffusing in the so-called tortuosity limit. The measurable diffusion constant approaches a constant value and the diffusion time dependency of the diffusion constant is lost. There are various methods to describe diffusion in or close to the tortuosity limit as this regime is characteristic for water diffusion within nerve cells [112, 123].

By performing measurements in this regime, parameters like the axon diameter [9–11] or other microstructural parameters of the brain can be extracted [124]. It is beyond the scope of this work to present a review of the different models and algorithms used for microstructural assessment.

In general the assessment of diffusion restriction effects has been successfully applied in many different scenarios like the measurement of cell size in cancer [12] or the extraction of structural information from the brain [124]. Despite the great potential of this technique, there are still challenges and pitfalls. Due to the fact that restriction is a high order effect, the fitting for microstructural parameters is challenging and most measurements suffer from low accuracy and precision. Additionally, model mismatches and missing validation measurements can be constituted as major difficulties of the presented methods. [12]

In scenarios with very small effects of restriction (large restriction barrier sizes combined with slow diffusion), the probing of microstructural information can become extremly challenging. This is exactly the case when restriction effects of lipids in AT are investigated. Applying the general model proposed by Murday and Cotts [114] in this scenario would be beneficial because it is valid for a wide range of diffusion times and not limited to a specific regime.

4.5.3 Measuring Restriction Effects in Adipose Tissue

Measuring diffusion properties of lipids with a clinical MR system is challenging, because the diffusivity of lipids is around two orders of magnitude smaller compared to water [13]. This can be explained by the large molecular size of fatty acids in comparison to water molecules. A low lipid diffusion coefficient increases the required diffusion encoding strength and diffusion time. This creates technical challenges related to eddy currents and the increased sensitivity to any

type of physiological tissue motion including involuntary movement. To extract information about the microstructure, DW experiments at different diffusion times or with a wide range of b-values need to be acquired which increases the experimental complexity. In addition, the fat spectrum is much more complex than the water spectrum, consisting of multiple different peaks with different relaxation times [125] and potentially different diffusion constants [126].

Extracting microstructural information from AT was shown to be possible in the size estimation of intramyocellular lipids [14] and brown adipocytes [15]. However, these measurements were mostly performed ex-vivo on a preclinical scanner with a strong gradient system. This thesis aims to develop techniques to probe the size of large adipocytes on a clinical scanner.

Histology analysis of subcutaneous AT show that the shape of the adipocytes within a 2D slice can be approximated by a circle and that no internal restriction barriers within the cells are visible [16]. Therefore, the assumption of a spherical shape of the adipocytes with free diffusion within the restriction barrier is reasonable and the restricted diffusion behavior can be described by the model proposed by Murday and Cotts (please refer to section 4.5 for more details) [114]. To probe the diffusion of lipids and eventually the microstructure of fatty tissue with large lipid droplets, sequences that allow very strong DW and long diffusion times are necessary.

Therefore, a single-voxel DW STEAM MRS sequence according to Ruschke et al [94] was employed in JP-I and JP-II. The sequence diagram is shown in Figure 4.2.
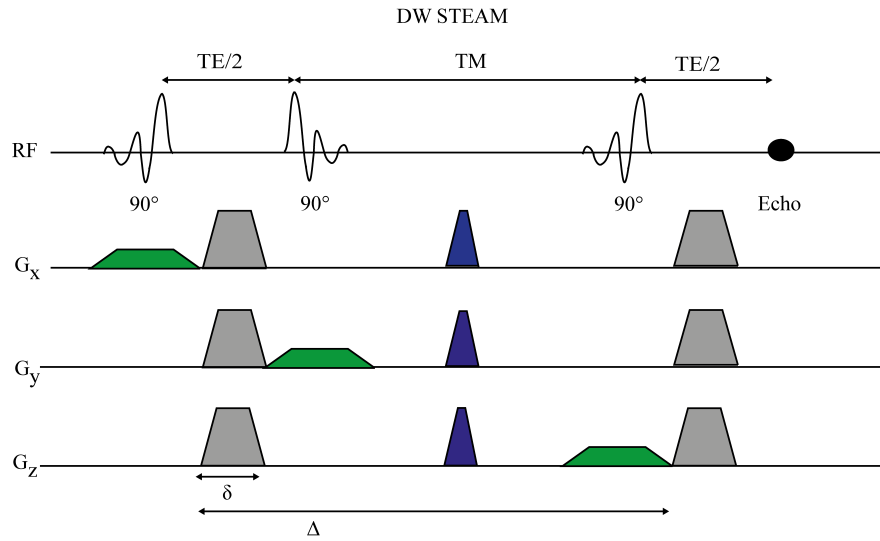
Figure 4.2: Sequence diagram of the DW-STEAM MRS sequence: The DW-STEAM magnetization preparation consists of 3 slice-selective 90° RF pulses and monopolar diffusion sensitizing gradients (in gray). Spoiler gradients (blue) and slice selective gradients (green) are also shown. To compensate for eddy currents, the sequence was repeated employing the diffusion gradient with different polarity. Δ, diffusion time; δ, time duration of the diffusion gradient; TE, echo time; TM, mixing time

The sequence is based on a standard single-voxel STEAM MRS sequence with diffusion gradients added after the first and third RF pulse to induce DW. The diffusion gradients also serve as spoiler gradients for unwanted magnetization pathways. Different diffusion times are

achieved by increasing TM while keeping TE constant. For eddy current compensation, the DW spectra are acquired with different polarity and the eddy current phase is subtracted in a post processing step. The described DW-MRS sequence enables the acquisition of high b-value DW measurements and simultaneously allows the acquisition of long diffusion times with moderate signal loss. The complexity of the fat spectrum can be resolved by separating the fat peaks in the frequency domain. The mean lipid droplet size can be extracted by modeling the DW signal acquired at different diffusion times and DW with equation 4.7. In JP-I, DW spectra in water-fat-emulsion phantoms and in vivo in the tibia bone marrow were acquired to extract a mean lipid droplet size. [127]

Motion-induced phase errors due to scanner table vibrations are especially severe when sequences with strong DW are used and limits the translation to a clinical application of the technique. In JP-II, an additional gradient was added before the DW-MRS sequence to mitigate signal loss induced by scanner table vibrations. The effect of this additional gradient was evaluated by laser interferometry and by ADC measurements in water-fat-emulsions phantoms and in vivo tibia bone marrow. [128].
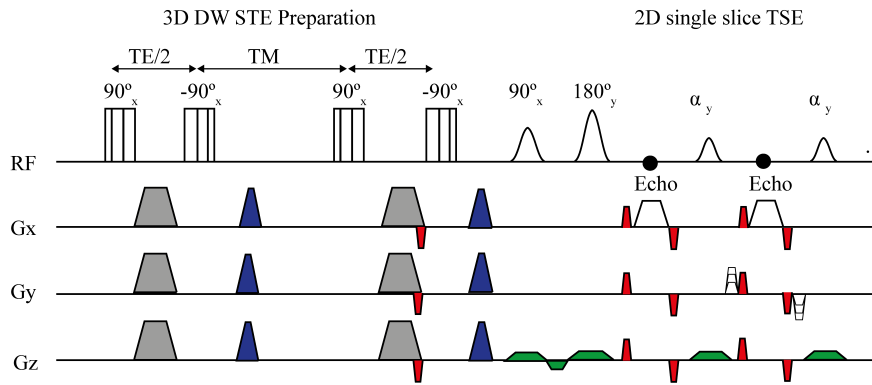
Figure 4.3: Sequence diagram of the STE-DW-prepared single shot 2D TSE. The diffusion weighted STE-DW magnetization preparation consists of four composite 90° RF pulses, mono-polar diffusion sensitizing gradients (gray) and spoiler gradient (blue). To eliminate motion-induced phase errors an additional pair of de-/rephasing gradients (indicated in red) denoted as magnitude stabilizers are introduced before the last tip-up pulse. Magnitude stabilizers are performed immediately before and after every spin echo formation. The slice selective gradients within the readout are indicated in green. TE, echo time; TM, mixing time

Single-voxel DW-MRS allows high SNR measurements but is associated with some limitations when clinically translating the lipid droplet size measurement: Due to the large voxel size, DW-MRS is sensitive to motion- and vibration-induced intra-voxel dephasing effects. The induced signal loss can lead to quantification errors which limits the in vivo applicability. Acquiring data with smaller voxel size would mitigate this effect. To allow the acquisition of data with smaller voxel size, a DW imaging approach is highly desirable. Therefore, a DW-TSE sequence was developed and it's performance was investigated in JP-III. Besides its reduced sensitivity towards intra-voxel dephasing effects, also the voxel's neighborhood

information could be incorporated into the droplet size fitting which would lead to a more robust fitting and spatially resolved droplet size data could be acquired. The corresponding sequence diagram is shown in Figure 4.3.

The proposed DW preparation is based on a stimulated echo (STE) preparation and consists of four non-selective 90° Malcolm-Levitt (MLEV) RF pulses. Mono-polar diffusion gradients are added similar to the DW-STEAM sequence described before. The preparation is combined with a single-shot 2D TSE readout. Magnitude stabilizing gradients following Alsop's method are introduced in the preparation and readout to eliminate eddy current induced phase errors [91, 97]. Again, different diffusion times can be achieved by changing TM of the STE preparation. The DW is adjusted by changing the diffusion gradient strength and TM. Also in this scenario, the lipid droplet size can be estimated based on equation 4.7 performing a voxel-wise fitting. To avoid local minima, the fitting can be performed with multiple initial starting values and a regularized minima selection process can further increase accuracy and precision.

In summary: Both presented sequences are capable of acquiring DW measurements with high DW and long diffusion time. Signal with different diffusion weighting and multiple diffusion times can be acquired and modeled by equation 4.7 which allows the extraction of a mean diameter under the assumption of a spherical cell. A small modification in the pulse sequence can be made based on the addition of a gradient to mitigate phase errors induced by scanner table vibrations.

5 Compliance with Ethical Standards

All investigations performed in studies involving human participants were in accordance with the ethical standards of the institutional and/or national research committee and with the 1964 Helsinki declaration and its later amendments or comparable ethical standards. Informed consent was obtained from all individual participants included in the studies.

6 Comprising Journal Publications

6.1 Journal Publication I:
Measuring large lipid droplet sizes by probing restricted lipid diffusion effects with diffusion-weighted MRS at 3T

The publication entitled *Measuring large lipid droplet sizes by probing restricted lipid diffusion effects with diffusion-weighted MRS at 3T* was published in Magnetic Resonance in Medicine (ISSN: 0740-3194) [127]. The manuscript was authored by Dominik Weidlich, Julius Honecker, Oliver Gmach, Mingming Wu, Rainer Burgkart, Stefan Ruschke, Daniela Franz, Bjoern H. Menze, Thomas Skurk, Hans Hauner, Ulrich Kulozik and Dimitrios C. Karampinos. It is available online (DOI: 10.1002/mrm.27651) as an open access article under the terms of the Creative Commons Attribution-NonCommercial-NoDerivs License. Preliminary results were also presented in the conference contribution C36, which was awarded with an ISMRM Summa Cum Laude Merit Award and selected as an oral presentation at the ISMRM annual meeting 2017. A summary of the publication is provided in Section 6.1.1, the author contributions are listed in Section 6.1.2 and the full text is included subsequently on the following pages.

6.1.1 Abstract

Purpose

The in vivo probing of restricted diffusion effects in large lipid droplets on a clinical MR scanner remains a major challenge due to the need for high b-values and long diffusion times. This work proposes a methodology to probe mean lipid droplet sizes using diffusion-weighted MRS (DW-MRS) at 3T.

Methods

An analytical expression for restricted diffusion was used. Simulations were performed to evaluate the noise performance and the influence of particle size distribution. To validate the method, oil-in-water emulsions were prepared and ex-amined using DW-MRS, laser deflection and light microscopy. The tibia bone mar-row was scanned in volunteers to test the method repeatability and characterize microstructural differences at different locations

Results

The simulations showed accurate and precise droplet size estimation when a sufficient SNR is reached with minor dependence on the size distribution. In phantoms, a good correlation between the measured droplet sizes by DW-MRS and by laser deflection ($R^2 = 0.98$; $p = 0.01$) and microscopy ($R^2 = 0.99$; $p < 0.01$) measurements was obtained. A mean coefficient of variation of 11.5 % was found for the lipid droplet diameter in vivo. The average diameter was smaller at a proximal (50.1 ± 7.3 µm) compared with a distal tibia location (61.1 ± 6.8 µm) ($p < 0.01$).

Conclusion

The presented methods were able to probe restricted diffusion effects in lipid droplets using DW-MRS and to estimate lipid droplet size. The methodology was validated using phantoms and the in vivo feasibility in bone marrow was shown based on a good repeatability and findings in agreement with literature.

6.1.2 Author contributions

The first author performed the experiments (MR measurements); programmed the magnetic resonance pulse sequence (propriety hardware specific libraries and software from Philips Medical Systems (Best, The Netherlands)); implemented the post-processing and the quantification process using Matlab (Mathworks, Natick, MA). With the help and consultation form the coauthors, the first author designed the experiment, manufactured the oil-in-water-emulsion phantoms, analyzed and interpreted the data, and wrote the manuscript.

FULL PAPER

Measuring large lipid droplet sizes by probing restricted lipid diffusion effects with diffusion-weighted MRS at 3T

Dominik Weidlich[1] | **Julius Honecker**[2] | **Oliver Gmach**[3] | **Mingming Wu**[1] | **Rainer Burgkart**[4] | **Stefan Ruschke**[1] | **Daniela Franz**[1] | **Bjoern H. Menze**[5] | **Thomas Skurk**[2] | **Hans Hauner**[2] | **Ulrich Kulozik**[3] | **Dimitrios C. Karampinos**[1]

[1]Department of Diagnostic and Interventional Radiology, Technical University of Munich, Munich, Germany

[2]Else Kröner Fresenius Center for Nutritional Medicine, Technical University of Munich, Munich, Germany

[3]Chair for Food and Bioprocess Engineering, Technical University of Munich, Freising, Germany

[4]Clinic of Orthopaedic Surgery, Klinikum rechts der Isar, Technical University of Munich, Munich, Germany

[5]Department of Computer Science, Technical University of Munich, Munich, Germany

Correspondence
Dominik Weidlich, Department of Diagnostic and Interventional Radiology, Klinikum rechts der Isar, Technical University of Munich, Ismaninger Str. 22, 81675 Munich, Germany.
Email: dominik.weidlich@tum.de

Funding information
European Research Council, Grant/Award Number: 677661 (ProFatMRI); Philips Healthcare

Purpose: The in vivo probing of restricted diffusion effects in large lipid droplets on a clinical MR scanner remains a major challenge due to the need for high b-values and long diffusion times. This work proposes a methodology to probe mean lipid droplet sizes using diffusion-weighted MRS (DW-MRS) at 3T.

Methods: An analytical expression for restricted diffusion was used. Simulations were performed to evaluate the noise performance and the influence of particle size distribution. To validate the method, oil-in-water emulsions were prepared and examined using DW-MRS, laser deflection and light microscopy. The tibia bone marrow was scanned in volunteers to test the method repeatability and characterize microstructural differences at different locations.

Results: The simulations showed accurate and precise droplet size estimation when a sufficient SNR is reached with minor dependence on the size distribution. In phantoms, a good correlation between the measured droplet sizes by DW-MRS and by laser deflection ($R^2 = 0.98$; $P = 0.01$) and microscopy ($R^2 = 0.99$; $P < 0.01$) measurements was obtained. A mean coefficient of variation of 11.5 % was found for the lipid droplet diameter in vivo. The average diameter was smaller at a proximal (50.1 ± 7.3 μm) compared with a distal tibia location (61.1 ± 6.8 μm) ($P < 0.01$).

Conclusion: The presented methods were able to probe restricted diffusion effects in lipid droplets using DW-MRS and to estimate lipid droplet size. The methodology was validated using phantoms and the in vivo feasibility in bone marrow was shown based on a good repeatability and findings in agreement with literature.

KEYWORDS
adipocytes diameter, adipose tissue microstructure, diffusion of fat, DW-MRS, lipid droplet

1 | INTRODUCTION

The measurement of lipid droplet size is important in the study of adipose tissue and ectopic lipids in both health and metabolic dysfunction across organs and tissues. In skeletal muscle, droplets of intramyocellular lipids are significantly smaller than extramyocelluar lipid droplets.[1] In fat depots containing brown adipose tissue, brown adipocytes consist of much smaller lipid droplets than white adipocytes.[2] In white adipose tissue, the adipocyte size has long been known to relate to the obese phenotype.[3] In bone marrow, adipocyte size has been recently linked to the differentiation of constitutive marrow adipose tissue from regulated marrow adipose tissue.[4] Therefore, the assessment of lipid droplet size enables the measurement of ectopic lipid droplet size (e.g., in intramyocellular lipids), the measurement of adipocyte size in adipocytes containing unilocular lipid droplets (e.g., in white adipocytes and bone marrow adipocytes), and the differentiation between adipocytes containing small multilocular lipid droplets (brown adipocytes) from large unilocular lipid droplets (white adipocytes). However, such an assessment of lipid droplet size in tissue currently requires a highly invasive biopsy procedure.

Diffusion-weighted (DW) MR is a powerful tool for the noninvasive assessment of tissue microstructure. The reduction of the ADC with increasing diffusion times due to diffusion restriction effects has been previously applied to extract cell size in vivo in water-containing tissues.[5] Measuring the diffusion properties of lipids has proven to be more challenging because fat has a diffusion coefficient approximately 2 orders of magnitude lower than water due to the large molecular size of fatty acids.[6,7] The low lipid diffusion coefficient increases the required diffusion encoding strength and diffusion time. The requirement for strong diffusion encoding and long diffusion times induces additional technical challenges related to eddy currents[8] and an overall increased sensitivity to any type of physiological tissue motion including involuntary movement.[9] Furthermore, the spectral complexity of fat (the fact that fat is composed of multiple fat peaks) constitutes a major challenge in the acquisition of DW-MR imaging measurements in fatty tissues.[10]

DW-MRS is a versatile tool to measure the diffusion properties of metabolites other than water.[11,12] When a high b-value is applied to fatty tissues, DW-MRS can measure the diffusion properties of lipids while additionally resolving the different fat peaks.[6] Recently, a high b-value DW-MRS has been applied to study myocellular lipid diffusion[13] and to quantify the intramyocellular lipid droplet size by analyzing the ADC dependence on diffusion time.[14] Diffusion restriction effects on the dependence of the DW signal on b-value have also been reported in murine brown adipocytes ex vivo using a preclinical MR system with strong magnetic field gradients.[15] Murine brown adipocytes enclose many lipid droplets with a diameter below 10 μm, whereas white adipocytes enclose a single lipid droplet with diameters between 50 and 150 μm. In white adipocytes, the size of a lipid droplet would be equivalent to the size of an adipocyte. Diffusion restriction effects are visible in the signal decay curves when molecules do not freely diffuse but hit a diffusion restricting barrier during the diffusion sensitizing period of time. The larger the dimensions of the restricting barriers in comparison to the mean free path diffusion length the smaller the measurable effect is. Therefore, the sensitization of diffusion restriction effects in white adipocytes requires long diffusion times.

Presently, DW-MRS is yet to be applied for the noninvasive measurements of lipid droplet size in large cells such as white adipocytes or bone marrow adipocytes. Probing diffusion restriction effects in large lipid droplets in vivo at a clinical scanner remains a major technical challenge due to the need for high b-value and long diffusion time DW-MRS and the sensitivity to macroscopic motion effects. The present work proposes a methodology to probe diffusion restriction effects in large lipid droplets using DW-MRS at a clinical 3T system. The bone marrow region of the lower leg has been selected as a tissue minimally affected by physiological motion effects to show the in vivo feasibility of the lipid droplet size measurements. The proposed method was first evaluated using simulations, was validated experimentally in water–fat phantoms, and then was finally applied in vivo to estimate the bone marrow adipocyte size within the tibia bone of healthy subjects.

2 | METHODS

2.1 | Theoretical background

Diffusion restriction barriers in an MR experiment will introduce deviations from the monoexponential signal decay and a reduction of the ADC values with increasing diffusion time. Assuming spherical boundaries, Murday and Cotts described the diffusion signal decay curve when restricted diffusion occurs[16]:

$$\ln\left(\frac{S(\Delta,\delta,G)}{S_0(\Delta)}\right) = -2\gamma^2 G^2 \sum_{m=1}^{\infty}\left[\alpha_m^2\left(\alpha_m^2\left(\frac{d}{2}\right)^2 - 2\right)\right]^{-1}$$
$$* \left(\frac{2\delta}{\alpha_m^2 D} - \frac{2 + \exp(-\alpha_m^2 D(\Delta-\delta)) - 2\exp(-\alpha_m^2 D\delta) - 2\exp(-\alpha_m^2 D\Delta) + \exp(-\alpha_m^2 D(\Delta+\delta))}{(\alpha_m^2 D)^2}\right)$$

(1)

where S is the DW signal, S_0 is the signal weighted by spin density and relaxation effects, Δ is the diffusion time, δ is the diffusion gradient length, G is the gradient strength, γ is the gyromagnetic moment, d is the diameter of the spherical restriction barrier, D is the free diffusion constant, and α_m are the roots obtained by the following differential equation of Bessel functions:

$$\left(\alpha_m \frac{d}{2} \right) J'_{\frac{3}{2}} \left(\alpha_m \frac{d}{2} \right) - \frac{1}{2} J_{\frac{3}{2}} \left(\alpha_m \frac{d}{2} \right) = 0 \qquad (2)$$

The equation for signal attenuation (Equation 1) is not only a function of the b-value and the diffusion constant but also a function of the diffusion time and the diameter of the diffusion restricting spheres. Therefore, the size of the diffusion restricting barriers can be extracted based on the DW signal at different diffusion times and diffusion weightings as shown in Equation 1.

2.2 | DW-MRS pulse sequence and spectra postprocessing

To measure the diffusion properties of lipids, a bipolar DW STEAM MRS (Figure 1) sequence was used. The sequence was based on a standard STEAM with additional diffusion gradients in all 3 axes added after the first and third RF pulse to induce diffusion weighting.[17] The diffusion gradient duration was maximized for a given TE and the strength of the diffusion weighting gradients was adjusted to achieve certain b-values. The readout started right after the second diffusion sensitizing gradient. The mixing time was increased while keeping the b-value constant to achieve the same diffusion weighting at different diffusion times. The DW spectra with
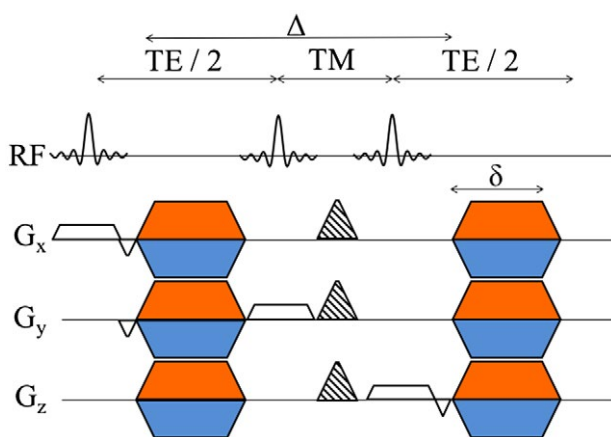
FIGURE 1 DW STEAM MRS sequence: The three 90° slice selective RF pulses generate a stimulated echo in a single voxel. The diffusion gradients (in color) are introduced in a standard STEAM MRS sequence to achieve diffusion weighting. To compensate for eddy current effects, the diffusion-weighting gradients alternate over the acquired averages between positive (orange) and negative (blue) polarity

different polarity of the DW spectra were acquired to compensate for eddy-current effects (half of the averages were acquired with positive and the other half with negative polarity).

The preprocessing of the spectra was based on a custom-built processing pipeline implemented in-house in MATLAB (MathWorks, Natick, MA).[17] The pipeline included zero order phase correction of each b-value and polarity and Gaussian apodization. The single averages were frequency aligned by taking the cross-correlation with the first average of each b-value and polarity and shifting the spectrum of the remaining averages in frequency domain until a maximum of the cross-correlation function was obtained. Averages with a deviation of the methylene peak amplitude of more than 2 SDs from the mean methylene peak amplitude were identified as outliers and excluded from the subsequent analysis. The effect of the outlier removal is further discussed in Supporting Information Figure S6 in the supplementary material, which is available online. The remaining averages for both polarities were combined and corrected for eddy currents. Peak area quantification was performed on the real spectrum fitting 8 fat peaks assuming Lorentzian peak shapes. The fat peaks included were: methyl at 0.90 ppm; methylene at 1.30 ppm, β-carboxyl at 1.60 ppm, α-olefinic at 2.02 ppm, α-carboxyl at 2.24 ppm, diallylic methylene at 2.75 ppm, glycerol at 4.20 ppm, and olefinic at 5.29 ppm.[17] Water signal was not detectable due to the strong diffusion-weighting. Only the methylene peak area (at 1.3 ppm) was used to estimate the lipid droplet size, because the different fat peaks, in general, differ in diffusion coefficient[6,15] and T_1 relaxation time.[18]

2.3 | Estimation of the diffusion restriction size

Equation 1 was used for fitting the acquired DW data. The infinite sum was calculated to the ~3000th root because afterward only negligible deviations from the signal decay were observed.

For a given diffusion time, the non-DW signal depends on the diffusion time due to T_1 relaxation effects. This gives the expression:

$$S_0(\Delta) = \rho * \exp \left(-\frac{\Delta - \frac{TE}{2}}{T_1} \right) = \rho * \exp \left(-\frac{TM}{T_1} \right) \quad (3)$$

The TE of the STEAM sequence was kept constant; therefore, no additional T_2 relaxation needed to be considered. The experimental data across diffusion gradient strengths, diffusion gradient durations, and diffusion times S_{exp} were thus fitted to an analytical signal expression using a 4-parameter fit with unknowns the free diffusion constant D, the diameter of diffusion restriction barrier d, the T_1 relaxation constant, and the overall signal ρ:

$$\arg\min_{D, d, T_1, \rho} || S(\Delta, \delta, G, T_1) * \rho * exp\left(-\frac{TM}{T_1}\right) - S_{exp} || \quad (4)$$

2.4 | Numerical simulations

To evaluate the noise characteristics of the fitting, a Monte Carlo simulation was performed. Rician noise with a SNR between 100 and 1300 was added to an artificial signal decay curve and the apparent diameter of the restriction barrier was fitted. The SNR was defined as the signal amplitude divided by the SD of the signal for the lowest b-value and shortest diffusion time. The simulation was repeated 500 times for each SNR level and both the mean and SD values of the diameter were calculated. The simulation parameters were: TM: between 300 ms and 700 ms in 100 ms steps, $\delta = 28$ ms, b-value $= 10,000 - 20,000 - 40,000 - 60,000$ s/mm^2 and restriction barrier diameter: 60 μm. The simulation was performed using diffusion coefficient values $D = 0.7 \times 10^{-5}$ mm^2/s and $D = 1.5 \times 10^{-5}$ mm^2/s to account for the dependence of D on the temperature for the phantom and in vivo experiments, respectively (see also below).

In a realistic experimental setting, it is likely that there will be a lipid droplet size distribution found for all lipid droplets. In bone marrow adipocytes, the droplet size distribution was reported to be a Gaussian distribution.[19] To test the dependency of the method on particle size distribution, the apparent diameter was simulated using 3 different lipid droplet sizes and different particle distributions. Here, lipid droplet diameters of 20 μm, 40 μm, and 60 μm were assumed and the theoretical signal assuming a Gaussian diameter distribution with SDs between 0 μm and 10 μm was calculated with the same simulation parameters as in the previous simulations. The simulated signal decay curves were again fitted using Equation 4 (which assumes a single diameter).

2.5 | Phantom measurements

To validate the proposed method water–fat phantoms (oil-in-water emulsions) with high fat concentration closely resembling in vivo adipose tissue lipid content were produced. Each phantom contained 800 mL sunflower oil (ARO), 200 mL soft water, 4 mL Tween 80 (Sigma-Aldrich, Taufkirchen) (emulsifier) and 1 g of sodium benzoate (Roth, Karlsruhe). Emulsification was carried out with a colloid mill (IKA Labor-Pilot 2000/4, IKA-Werke GmbH & Co. KG, Staufen) at 5000, 6000, 9000, and 12,000 revolutions per minute (rpm) to obtain different oil droplet sizes within the water matrix (standardized emulsification process).[20]

The phantoms were scanned on a clinical 3T system (Ingenia Elition, Philips Healthcare, Best) with a maximal diffusion gradient strength of 40 mT/m and a slew rate of 200 mT/m ms using 8-channel wrist coil with the following scanning parameters: DW STEAM MRS with volume of interest: (15 mm)^3, TE: 60 ms, $\delta = 28$ ms, TR: 1800 ms, 4096 points, spectral width: 5000 Hz, 8 phase cycles, 16 averages per b-value (half of the averages with positive and the other half with negative polarity), 1 start-up cycle, b-values: 10,000 – 20,000 – 40,000 – 60,000 s/mm^2, 14:02 min scan time per voxel location, mixing times of 300, 400, 500, 600, and 700 ms. As the DW sequence applied maximum available gradient strength and slew rates, strong vibrations of the scanner table were induced. To minimize any measurement errors induced by the table vibrations, the phantoms were placed on a wooden support table decoupled from the scanning table.

To estimate the SNR of the phantom scans, the measurements were repeated 10 times in the 6000 rpm phantom for the shortest mixing time and lowest b-values. The methylene peak area was estimated individually for each average and the peak area SNR was defined as the mean signal value divided by SD of the methylene peak area.

For validation purposes, the lipid particle size distribution within the water–fat phantoms was measured by 2 different reference methods. First, the lipid droplet size was measured by dynamic light scattering using a particle sizing instrument (Mastersizer 2000 with Hydro 2000S dispersing unit, Malvern Instruments GmbH, Worcestershire). Samples were diluted with 0.5 % sodium dodecyl sulfate (Serva, Heidelberg) solution (1:10, v/v) to separate agglomerates and measure the size of single droplets. Size distributions were logarithmically depicted between 10 nm to 10 mm.

Last, light microscopy was used to analyze the droplet sizes. All the slides were divided into 3 different sections with Leukosilk surgical tape (BSN Medical, Hamburg, Germany) and prewetted with 100 μL water. Afterward, small amounts of emulsion (approximately 10 μL) were added and spread across each section through gentle swirling. The slides were cover-slipped, and 3 images were acquired per section using 20× magnification (Leica DMI 4000 b, Leica Microsystems, Wetzlar). The droplet area was determined automatically using CellProfiler image analysis software (Broad Institute, Cambridge) and converted to diameter by assuming that lipid droplets were spherical.[21] Between 1725 droplets (5000 rpm emulsion) and 8467 droplets (12,000 rpm emulsion) were automatically measured to determine the particle distributions.

All the reported particle size distributions were based on the lipid droplet volume and not the lipid droplet number. This characterization accounted for the fact that larger lipid droplets contained more lipids. From the particle size distributions, mean diameters were extracted for all the validation experiments and, then, were used subsequently for the analysis.

2.6 | In vivo measurements

Given the strong diffusion weighting and the long diffusion times, the proposed DW-MRS sequence was sensitive to any

kind of macroscopic movement. To eliminate these potential artifact, the proposed method was applied to the nonmoving fatty tissue of the tibia bone marrow.

The robustness in vivo was measured by first scanning the tibia of 3 healthy volunteers 3 times in a row at approximately the same location, with subject repositioning on the scanner table between the 3 scans. To identify location-dependent microstructural differences, the tibia bone marrow of 7 healthy volunteers (27.0 ± 1.8 years old) was scanned at 2 different locations. Water-only images (to aid voxel placement) were computed using the online vendor's chemical shift encoding-based water–fat-separation algorithm on the data from a 3D multi-echo gradient echo sequence using bipolar (non–fly-back) gradient readout. The parameters FOV = 140 × 140 × 105 mm^3, voxel size = 1.35 × 1.35 × 1.5 mm^3, TR/TE1/ΔTE = 8.3/1.31/1.1 ms, flip angle = 5°, and 6 echoes were used for the measurement. The first spectroscopy voxel was placed approximately 1 cm below the growth plate in the tibia bone marrow (proximal location), whereas the second voxel was placed approximately 4 cm below the growth plate (distal location). The repeatability experiment was performed at the proximal location. Both experiments were performed on the same clinical scanner as the phantom experiments and with an 8 channel extremity coil. The sequence parameters were, except of the voxel size (volume of interest of proximal location: 18 × 18 × 18 mm^3; distal volume of interest: 14 × 14 × 20 mm^3), identical with the phantom experiments.

3 | RESULTS

3.1 | Simulation results

In Figure 2, the noise performance of the droplet size estimation was evaluated for phantom and in vivo conditions and at different peak area SNR levels. The experimentally determined methylene peak SNR was also included in Figure 2 for both conditions. The simulation shows that the proposed method leads to an underestimation of the droplet diameter if

FIGURE 2 Monte Carlo simulation of the droplet size estimation for different peak area SNR levels in (A) phantom and (B) in vivo conditions. The experimentally determined peak area SNR is also shown by the vertical yellow line. A decreased peak SNR leads to an underestimation of the theoretical diameter of 60 μm and a higher SD. The experimentally measured peak SNR has a relative error of 7.6 % (phantom) and 9.3 % (in vivo), respectively
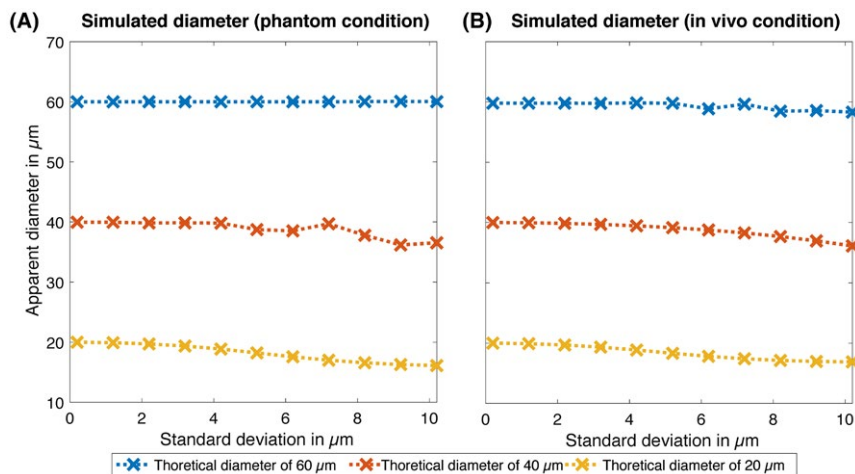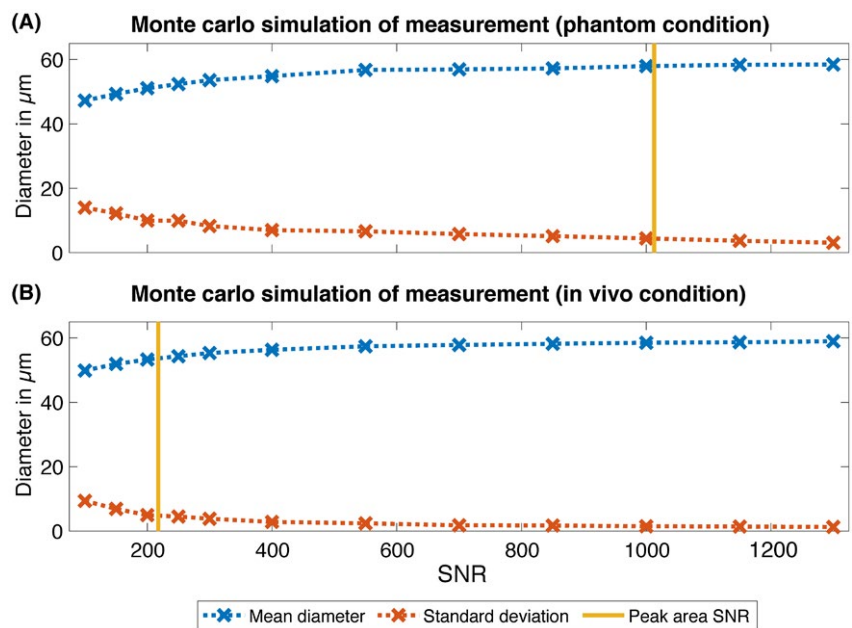
FIGURE 3 The simulation dependence of the proposed method on the lipid droplet size distribution for (A) phantom and (B) in vivo conditions. The lipid droplet diameter stays within a relative error of 11 % (phantom) and 9 % (in vivo), respectively, up to a particle SD of 10 μm for the 3 different theoretical diameters

the peak SNR is low in both the phantom and the in vivo experimental settings. In the phantom case with a lower diffusion constant the dependency of the mean droplet size on the peak area SNR is more prominent. However, the difference between the simulated cell diameter and the real cell diameter is small when a sufficient peak SNR is reached. Using a simulated diameter of 60 μm, an experimental diameter of 58.0 ± 4.4 μm (phantom condition) and 53.3 ± 4.9 μm (in vivo condition) was estimated at the experimentally determined peak area SNR levels.

Figure 3 shows the dependency of the simulated lipid droplet diameter on the Gaussian particle distribution. The error in the droplet diameter estimation was found to stay below 11 % for the phantom condition and 9 % for the in vivo condition when the SD of the distribution was increased to 10 μm. For larger SDs of the droplet distribution, an underestimation of the experimental mean diameter was predominantly observed for the smaller mean diameters of 20 μm and 40 μm.

This robustness in estimating the real mean diameter also in the presence of an underlying particle distribution was observed for all simulated diameters and SDs in both phantom and in vivo conditions.

3.2 | Phantom results

Figure 4 shows representative DW MR spectra and DW signal decay results from the water–fat phantom with a 6000 rpm rotation frequency. The measurement was performed by placing the phantom on the scanner table (Figure 4, first row). The phantom was stabilized on a wooden support table, which helped to decouple the phantom from the MR scanner and reduce the influence of any vibrational artifacts (Figure 4, second row). Both the DW spectra and the fitted signal decay curves for each mixing time were very similar for the 2 experimental conditions. The fitted model and the experimentally acquired data points were both in good agreement. However, when studying the relative signal at the highest b-value, a systematic decrease in the signal with increasing mixing times was observed when the wooden support table was used. When the phantoms were placed on the scanner table also a decrease of the relative signal decay was
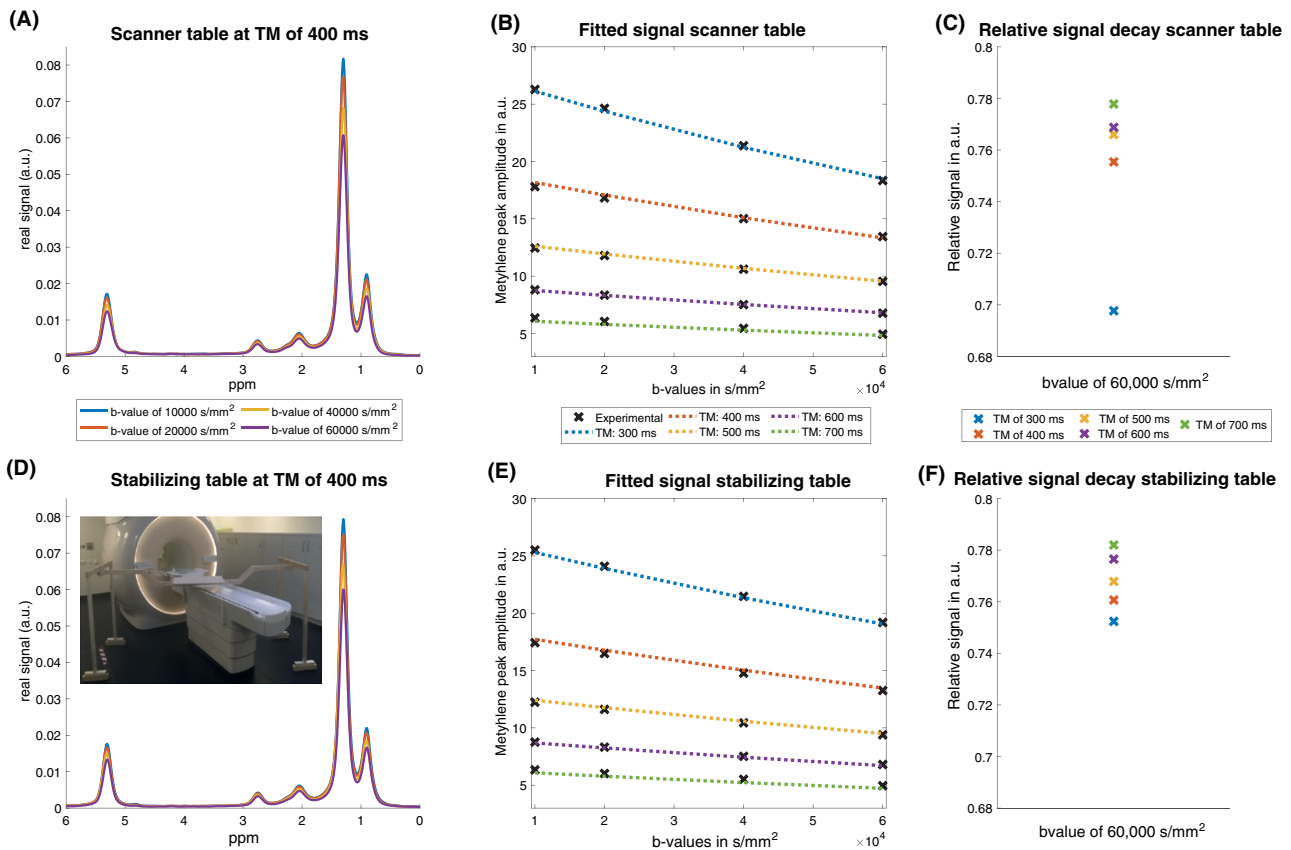
FIGURE 4 DW MR spectra (A,D), fitted methylene peak area signal (B,E) and relative signal decay (signal at the highest diffusion weighting divided by the signal at the lowest diffusion weighting at a given TM) at highest b-value for the 6000 rpm phantom (C,F) measured on the scanner table (first row) and measured on the wooden support table (second row). Minor differences can be observed when comparing the DW spectra and the DW signal decay curves. A systematic and stable decrease of the relative signal decay with increasing diffusion time (as indicated by the theoretical description of restricted diffusion) is only visible when the stabilizing table was used (F), compared with when the samples were placed on the scanner table (C)

visible. However, the diffusion signal decay dependency on the acquired mixing times was irregular, indicating additional confounding factors on the droplet size measurement. A systematic decrease in ADC with increasing diffusion time (as in exemplary case from an ADC of 5.7×10^{-5} mm^2/s to

4.8×10^{-5} mm^2/s when increasing the mixing time from 300 ms to 700 ms) agreed well with the theoretical description of restricted diffusion. The scanning table vibrations could induce additional signal decay, and these artifacts might have been superimposed on the measured signal. Therefore,

FIGURE 5 The volume particle size distributions in water–fat phantoms measured with (A) laser deflection and (B) microscopy. The distributions measured with both methods show similar shapes. The microscopic analysis measured smaller diameters for all phantoms. The second row shows an image section of the pictures used for the microscopy analysis for (C) the 5000 rpm phantom and (D) the 12,000 rpm phantom
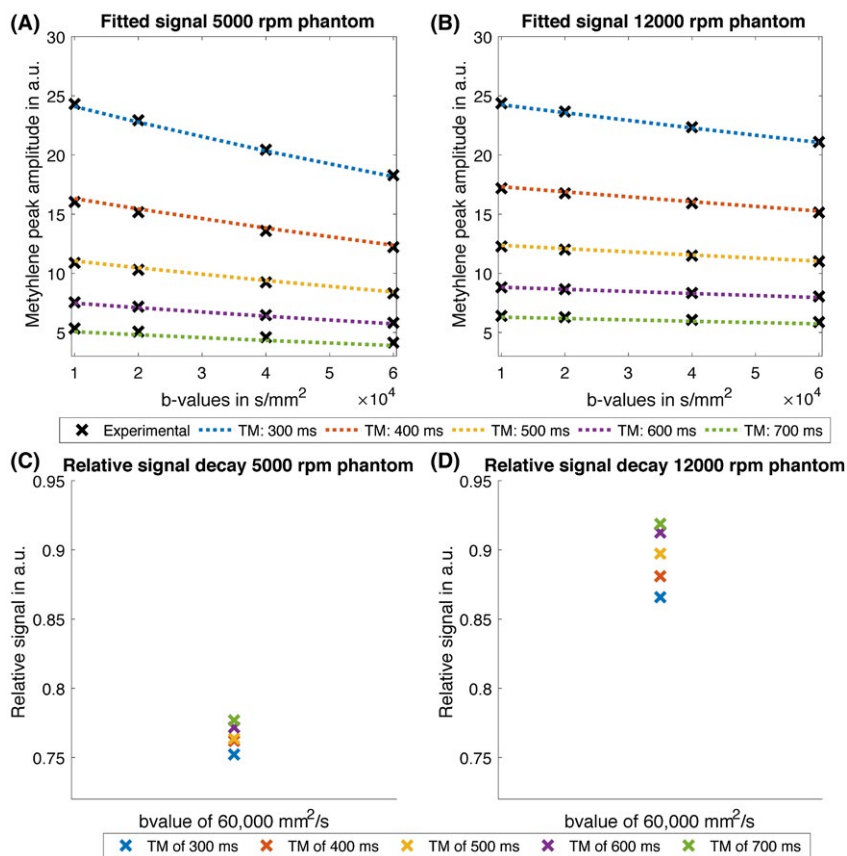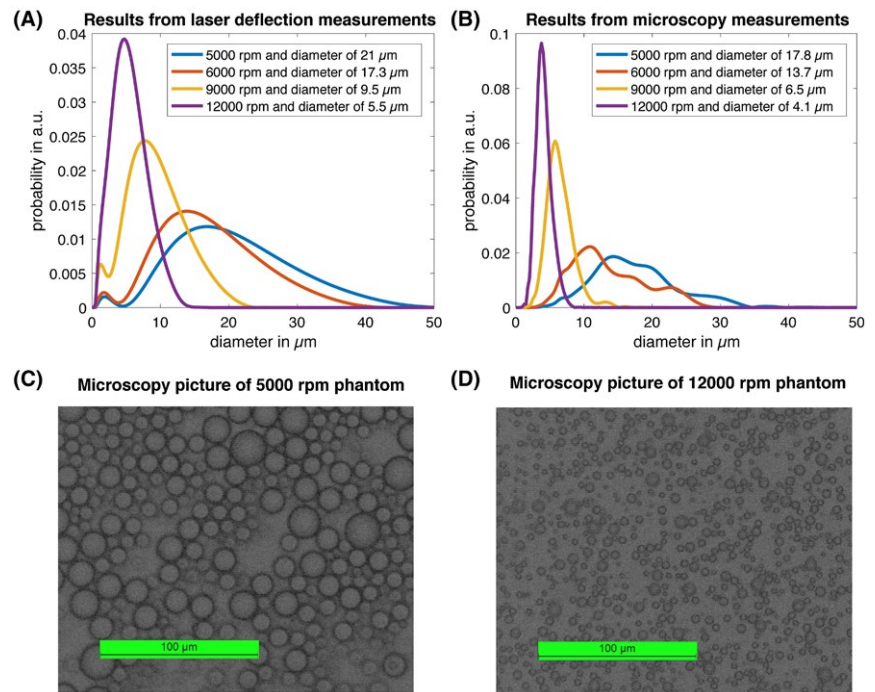
FIGURE 6 Representative signal decay curves and fitting results for (A) the 5000 rpm phantom and (B) the 12000 rpm phantom. C,D, The corresponding relative signal decay, which is the signal at the highest diffusion weighting divided by the signal at the lowest diffusion weighting at different TMs. A decrease in the signal decay slope with increasing diffusion time indicates the presence of diffusion restriction effects. In the 12,000 rpm phantom, a strong dependency of the relative signal decay on the diffusion time is observed and indicates smaller restriction barriers
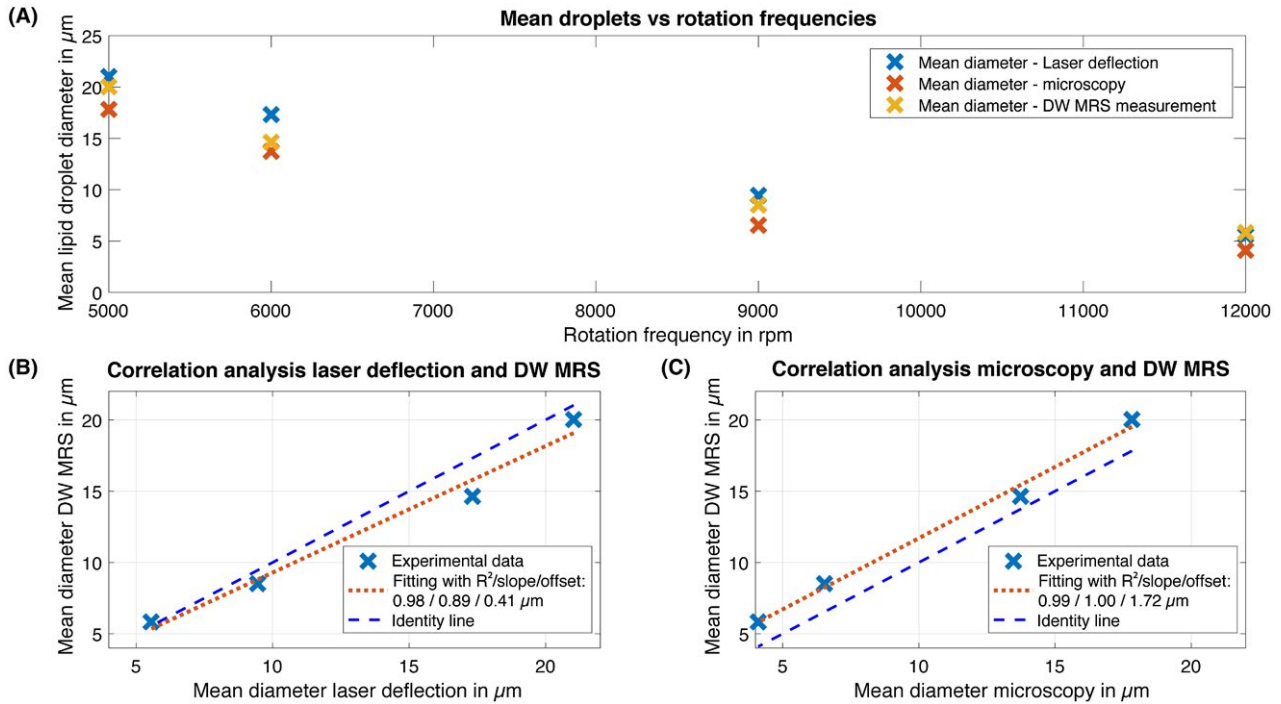
FIGURE 7 The mean diameter obtained by DW-MRS for the 2 validation measurements (A). The DW-MRS correlation analysis using (B) laser deflection and (C) microscopy are also shown. The R^2 coefficients are in good agreement between DW-MRS and laser deflection ($R^2 = 0.98$; $P = 0.01$) and between DW-MRS and microscopy ($R^2 = 0.99$; $P < 0.01$)

the subsequent phantom scans were all performed with the wooden support table. The quality of the MR data for the other phantoms was similar to the data shown in Figure 4.

Figure 5 shows the particle size distributions obtained using laser deflection (Figure 5A) and microscopy analysis (Figure 5B). Based on the mean diameter distributions, values were extracted for each phantom. The particle size distributions measured with both methods showed, in general, a similar shape. The extracted mean diameters for the 5000, 6000, 9000, and 12000 rpm phantoms were 21 μm, 17.3 μm, 9.5 μm, and 5.5 μm (laser deflection measurement) and 17.8 μm, 13.7 μm, 6.5 μm, and 4.1 μm (microscopy measurement). In general, both methods showed the same trend. However, the mean diameters obtained using microscopy were found to be smaller than the diameters measured by laser deflection.

Figure 6 shows a comparison between the signal decay curves of the phantom with a stirring frequency of 5000 rpm and 12,000 rpm, respectively. In both phantoms, the experimental signals and the fitted signals were in good agreement with each other. Nevertheless, the difference between the 2 phantoms were not easily discernable on the pure signal decay curves for the different mixing times, except a stronger signal decay of the 5000 rpm phantom. The relative signal decay at the highest b-value revealed that it was slower for the 12,000 rpm phantom compared with the 5000 rpm phantom for all measured mixing times. A dependency on the mixing time was found more prominent for the 12,000 rpm phantom.

Figure 7A compares the mean diameter obtained by DW-MRS, laser deflection, and microscopy for the different water–fat phantoms. All 3 measurements showed the same trend of reduced lipid droplet size with increasing stirring rotation frequency. In Figure 7B and E, the lipid droplet size estimated by DW-MRS, laser deflection (Figure 7B), and microscopy (Figure 7C) are shown. The coefficients of determination for the linear regression were high when comparing DW-MRS with laser deflection ($R^2 = 0.98$; $P = 0.01$) and DW-MRS with microscopy ($R^2 = 0.99$; $P < 0.01$). The resulting linear regression showed a slope of 0.89 and an offset of 0.41 μm when comparing DW-MRS measurements with the laser deflection. A slope of 1.00 and an offset of 1.72 μm was found when comparing DW-MRS and microscopy measurements.

3.3 | In vivo results

Figure 8 shows the spectroscopy voxel placement, the in vivo tibia bone marrow DW spectra for the shortest mixing time and the fitted signal decay curves for the proximal voxel location (first row) and distal voxel location (second row) from one volunteer. Here, the DW signal had a higher attenuation when comparing the in vivo measurements with the phantom measurements. The acquired spectra and signal decay curves were of similar quality for all measurements taken. Based on the extracted peak area for methylene, the size of the bone
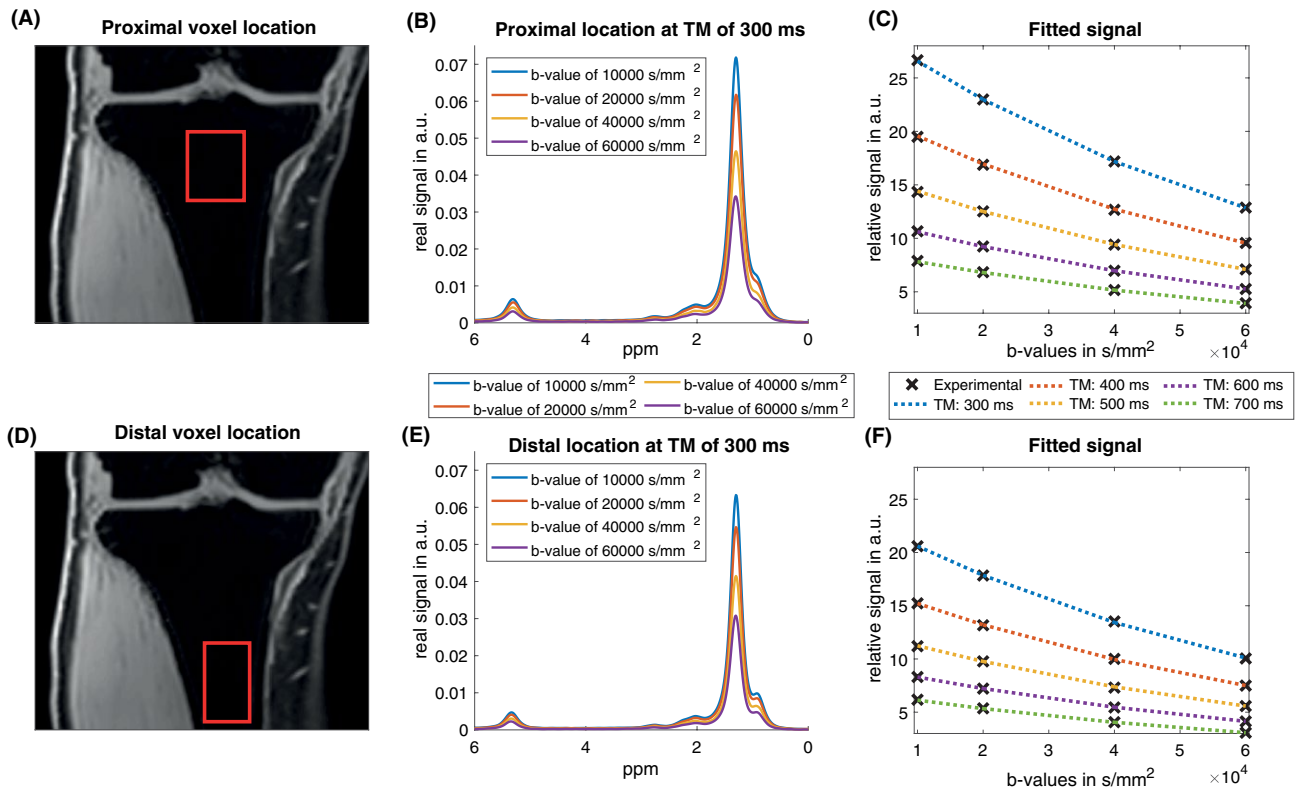
FIGURE 8   The voxel location in water-only Dixon images of the tibia at the A, proximal and (D) distal location. B,E, The DW spectra at the shortest TE. C,F, The corresponding fit to the peak area of methylene. The fitted signal decay curves correspond well to the measured data points
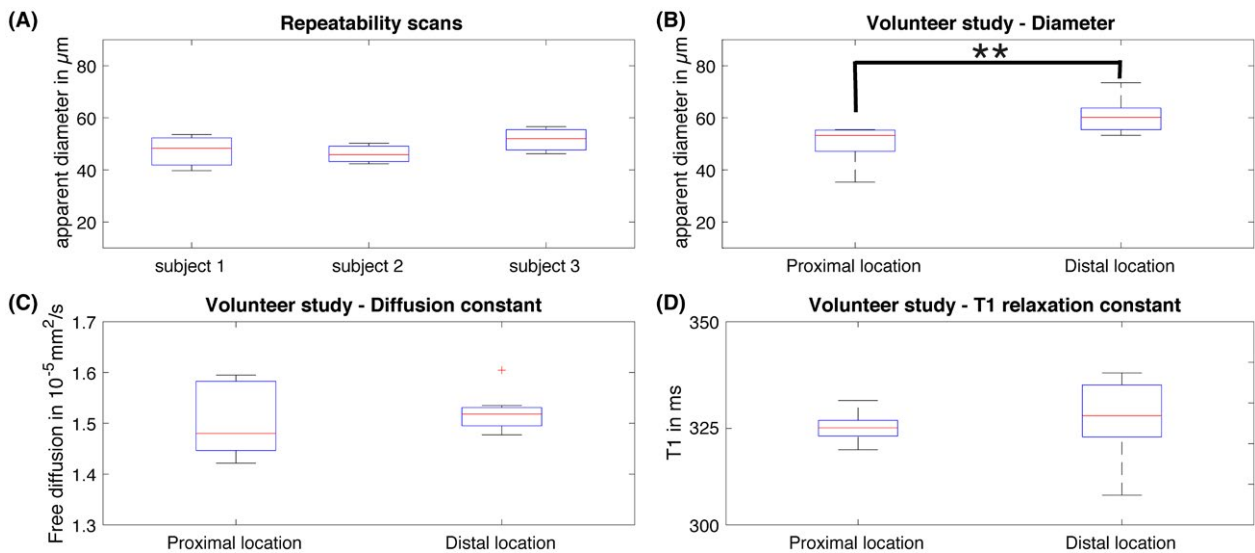

FIGURE 9   A, A summary of the repeatability measurements in the 3 subjects. The mean adipocyte cell diameter stayed within a relative error of 15% in all cases. The mean diameters measured for the repeatability study were 47.2 ± 7.0 μm, 46.1 ± 4.0 μm, and 51.6 ± 5.2 μm. B, A boxplot from the volunteer study. For every volunteer, the cell diameter was significantly larger in the distal location (61.1 ± 6.8 μm) compared with the proximal location (50.1 ± 7.3 μm) ($P = 0.003$). The free diffusion constant (C), and T_1 relaxation constant (D) for the volunteer study did not show significant differences between the two locations

marrow adipocytes was estimated for both locations and in all subjects. The fitting and the experimental data were also in good agreement.

Figure 9A shows the results from the in vivo repeatability scans. The acquired data for the 3 subsequent scans were all processed with the same postprocessing pipeline

and the mean diameter for the bone marrow adipocytes size was extracted. The coefficient of variation (defined by the SD divided by the mean value) stayed below 15 % for all 3 volunteers studied, with a mean coefficient of variation of 11.5 %.[22] The measured diameters for each of the 3 volunteers were 47.2 ± 7.0 μm, 46.1 ± 4.0 μm, and 51.6 ± 5.2 μm.

Figure 9B summarizes the results from the volunteer study at 2 different locations in the tibia. Larger lipid droplet sizes were observed more distally in the tibia bone marrow. The mean diameter at the proximal location was 50.1 ± 7.3 μm and 61.1 ± 6.8 μm at the distal location. For each volunteer, the diameter measured distally was smaller than the diameter measured proximally. A significant difference was found between the two locations ($P < 0.01$).

4 | DISCUSSION

The present study proposes a methodology to measure lipid droplet sizes with DW-MRS. The restricted diffusion effects in the DW-MR measurements of lipid droplets have been reported previously for lipid droplets a few microns in size using the strong gradient hardware of preclinical MR scanners.[14,15] The diffusion restriction effect induced by the lipid droplet boundary on the fat DW signal is reduced as the lipid droplet size increases, requires longer TEs as the gradient strength of gradient hardware decreases and can be confounded by scanner table vibrations and physiological motion due to the need of using high b-values. The present results show that it is feasible to measure large lipid droplet size using the gradient hardware of a clinical 3T system based on both phantom and in vivo measurements.

Previously published work has predominantly extracted an estimate for the restriction size by exploiting deviations from the monoexponential diffusion signal decay curve at a specific diffusion time.[14,15] An estimate for the diffusion restriction size can also be obtained when investigating the dependency of the diffusion constant on the diffusion time[23] assuming the short diffusion time limit (mean free path length is much smaller than the restriction barrier size). Instead, in the present work, signal decay curves obtained at different mixing times (corresponding to different diffusion times) are fitted all at once using the signal model of Equation 4. The present approach additionally requires the fitting for the T_1 relaxation constant because the signal decay curves acquired at different mixing times yield different T_1 weighting. The Supplementary Material characterizes the superior noise performance of the present single-step fitting approach compared with a 2-step approach first estimating ADC per diffusion time and second fitting the ADC dependence on diffusion time to a diffusion model (see Supporting Information Figure S1-S5).

The simulations performed showed that it is possible to extract information about the restriction barrier size when the peak SNR is sufficient. The effect of the diffusion restricting barriers on the DW signal decay curve is small compared with the influence of the diffusion properties or relaxation parameters. Therefore, a rather high peak area SNR is necessary to extract reliable information about the restricting barrier dimensions. However, for both the phantom and in vivo conditions, the experimental parameters were set so a reliable estimate of the droplet size could be measured. The simulated error stayed below 7.6 % for the phantom measurements and below 9.3 % for the in vivo measurements. If the peak area SNR is low, real lipid droplet size can be underestimated because the noise floor at longer mixing times mimics stronger diffusion restriction effects. Based on the simulations and the experimentally obtained in vivo peak SNR values, it can be inferred that the bone marrow adipocytes size will be underestimated. Improvements in the experimental setup and longer scan times may help to overcome such problems.

Another important aspect of the estimated lipid droplet size is the lipid droplet distribution. Figure 3 indicates that an underlying Gaussian particle distribution will only result in small deviations from the real mean value even if the distribution is broad compared with the cell diameter (e.g., an SD of 10 μm and a mean diameter of 20 μm). This finding is important for 2 reasons. First, the current description of the restricted diffusion behavior of the signal only assumes a single diameter. Multiple radii or a distribution of particle sizes can be introduced to the model but, given a high peak SNR is required, introducing more fitting parameters would only decrease the stability of the fitting process. Second, in biological tissue, a particle size distribution is more likely than a single defined diameter. Given the shown robustness of the proposed method toward the particle distribution broadness, it can be concluded that the present method delivers meaningful mean droplet sizes even if no particle size distribution is considered in the modelling, at least under the assumption of an underlying Gaussian distribution.

The analysis of water–fat phantoms was of particular interest because a ground-truth particle size was obtained through 2 independent validation measurements. Moreover, lipid droplets in a liquid water matrix can be considered as a good model to examine the restriction effects in fat adipocytes. The phantom lipid droplet size distributions measured using laser deflection and microscopy (Figure 5) were found to be quite similar. Due to the manufacturing process, a decrease in the stirring frequency of the colloid mill leads to larger lipid droplet size distributions. The observed differences between the 2 validation measurements could be explained due to the structural inhomogeneity of the water–fat phantoms, measurement inaccuracy, and differences in the phantom material used during the preprocessing stage. The

trend toward smaller diameters measured using the microscopy technique could also partly explain the fact that light scattering only measured the outer diameter of the lipid droplets, whereas microscopy postprocessing software typically measures the inner diameter.

When examining the water–fat phantoms with DW-MRS, vibrations from the scanner table were observed due to the strong diffusion weighting gradients. Figure 4 highlights the need to decouple the samples from the scanner table. If no auxiliary hardware is used and the samples are directly placed onto the scanning table, excess signal attenuation is observed at specific mixing times. This could be explained by certain mechanical resonances that cause the scanner table to vibrate at specific sequence times and diffusion gradient strengths.[24] Consequently, the signal decay cannot be described by a model of restricted diffusion, because the scanner table vibrations induce deviations from such a model. A wooden support table that is not connected to the scanner and, therefore, decoupled from the vibrations mitigated the vibration-induced artifacts. Therefore, all the phantoms were examined with this additional hardware.

In general, as Figure 4 shows, the peak SNR found in DW spectra was very high for all phantoms and mixing times. Phantoms manufactured with increased stirring frequency showed a stronger dependence on the signal decay when different mixing times were applied to the DW-MRS sequence. That corresponds to a stronger dependency of the apparent diffusion constant on the diffusion time for smaller diffusion restriction barriers. In Figure 6, this stronger dependency of the relative DW signal decay on the diffusion time can be observed for the phantom with the smallest lipid droplet diameter (12,000 rpm phantom) compared with the phantom with the largest lipid droplet diameter (5000 rpm phantom). For all the 4 different water–fat phantoms, a mean lipid droplet diameter was extracted and compared with the 2 validation measurements. For lipid droplet sizes obtained by DW-MRS, both validation measurements resulted in high R^2 values. Therefore, the present water–fat phantom study shows that DW-MRS can measure the mean lipid droplet diameters with small absolute deviations found between the different measurement methods. These results prove the applicability of the proposed method to measure lipid droplet sizes in water–fat containing phantoms.

In vivo, the presented method showed good reproducibility. The measured bone marrow diameter stayed within a relative error of 15 % during the re-positioning experiments for all the 3 healthy volunteers. This shows that the present approach is capable of measuring lipid droplet size with good precision. In the volunteer study, the bone marrow adipocytes were found to have a diameter between 40 and 70 μm, showing a tendency for larger cells more distally in the tibia bone marrow. Diameters of around 60 μm were reported in previous studies for bone marrow adipocytes,[19]

and recent findings indicate that they also increase in size from proximal to distal locations.[4] Therefore, the presently extracted adipocyte sizes are consistent with the literature and the observed differences along the long axis of the tibia agree with recent reports.

The noninvasive measurement of lipid droplet size has a wide range of applications in different tissues. In bone marrow, MR techniques have been emerging for measuring bone marrow water-fat composition[10] but techniques are lacking for the assessment of bone marrow adipose tissue (BMAT) microstructure, which is needed to differentiate between regulated BMAT and constitutive BMAT.[4] In human adipose tissue depots containing brown adipose tissue, techniques assessing lipid droplet microstructure are needed to overcome the partial volume effects on the fat fraction measurements in regions containing both white and brown adipose tissue.[25,26] The present results show that lipid droplet size measurements can be validated in water–fat phantoms and applied with good reproducibility in the tibial bone marrow. However, any extension to the present methods for other body regions requires further investigation.

The methodology shown in this study has several limitations. First, only the mean lipid droplet diameter can be estimated. The results from the simulations and phantom study show that deviations of the apparent lipid droplet diameter from the real lipid droplet diameter can occur. However, the deviations from the mean droplet diameter size were relatively small for a range of possible droplet diameters and different Gaussian droplet size distributions. Second, the range in droplet size for the water–fat phantoms scanned did not match the expected adipocytes size within the bone marrow or other larger adipocytes. However, good agreement was shown for the range of phantom diameters useed. It can be assumed that this will also be valid for larger lipid droplets if the appropriate peak SNR requirements are met. Third, no validation measurements for the in vivo adipocyte cell diameter was performed due to a lack of noninvasive reference measurements. However, the phantom data obtained did show a good agreement with 2 different reference measurements. The in vivo extracted bone marrow adipocyte size is consistent with those in literature and the observed differences along the axis of the tibia also agree with recent reports.[4,19] Fourth, no optimization of the experimental parameters to reduce the total acquisition time was performed in the present work. Finally, a translation of the presented method to anatomical regions with macroscopic physiological motion (induced by the respiratory or the cardiac cycle) is challenging due to the strong diffusion weightings and long diffusion times. Triggering and smaller voxel sizes could help to decrease the effects of intravoxel dephasing due to macroscopic physiological movement.

5 | CONCLUSIONS

In summary, the methods used in this study were able to probe diffusion restriction effects in lipid droplets in phantoms and in vivo at a 3T clinical scanner using long diffusion time and high b-value DW-MRS and to estimate lipid droplet size. The presented method was validated in phantoms showing good agreement with laser deflection and light microscopy measurements. The application of the method in the in vivo tibial bone marrow of healthy volunteers showed an estimation of the lipid droplet size with good repeatability and in agreement with the literature.

REFERENCES

1. Suzuki M, Shinohara Y, Ohsaki Y, Fujimoto T. Lipid droplets: size matters. *J Electron Microsc (Tokyo)*. 2011;60(Suppl 1):S101–S116.
2. Cousin B, Cinti S, Morroni M, et al. Occurrence of brown adipocytes in rat white adipose tissue: molecular and morphological characterization. *J Cell Sci*. 1992;103(Pt 4):931–942.
3. Salans LB, Cushman SW, Weismann RE. Studies of human adipose tissue. Adipose cell size and number in nonobese and obese patients. *J Clin Invest*. 1973;52:929–941.
4. Scheller EL, Doucette CR, Learman BS, et al. Region-specific variation in the properties of skeletal adipocytes reveals regulated and constitutive marrow adipose tissues. *Nat Commun*. 2015;6:7808.
5. Assaf Y, Blumenfeld-Katzir T, Yovel Y, Basser PJ. AxCaliber: a method for measuring axon diameter distribution from diffusion MRI. *Magn Reson Med*. 2008;59:1347–1354.
6. Lehnert A, Machann J, Helms G, Claussen CD, Schick F. Diffusion characteristics of large molecules assessed by proton MRS on a whole-body MR system. *Magn Reson Imaging*. 2004;22:39–46.
7. Steidle G, Eibofner F, Schick F. Quantitative diffusion imaging of adipose tissue in the human lower leg at 1.5 T. *Magn Reson Med*. 2011;65:1119–1125.
8. Jezzard P, Barnett AS, Pierpaoli C. Characterization of and correction for eddy current artifacts in echo planar diffusion imaging. *Magn Reson Med*. 1998;39:801–812.
9. Anderson. Analysis and correction of motion artifacts in diffusion weighted imaging. *Magn Reson Med*. 1994;32:379–387.
10. Karampinos DC, Ruschke S, Dieckmeyer M, et al. Quantitative MRI and spectroscopy of bone marrow. *J Magn Reson Imaging*. 2018;47:332–353.
11. Nicolay K, Braun KP, Graaf RA, Dijkhuizen RM, Kruiskamp MJ. Diffusion NMR spectroscopy. *NMR Biomed*. 2001;14:94–111.

12. Ronen I, Valette J. Diffusion-weighted magnetic resonance spectroscopy. *eMagRes*. 2015;4:733–750.
13. Brandejsky V, Kreis R, Boesch C. Restricted or severely hindered diffusion of intramyocellular lipids in human skeletal muscle shown by in vivo proton MR spectroscopy. *Magn Reson Med*. 2012;67:310–316.
14. Cao P, Fan SJ, Wang AM, et al. Diffusion magnetic resonance monitors intramyocellular lipid droplet size in vivo. *Magn Reson Med*. 2015;73:59–69.
15. Verma SK, Nagashima K, Yaligar J, et al. Differentiating brown and white adipose tissues by high-resolution diffusion NMR spectroscopy. *J Lipid Res*. 2017;58:289–298.
16. Murday JS, Cotts RM. Self-diffusion coeffcient of liquid lithium. *J Chem Phys*. 1968;48:4938.
17. Ruschke S, Kienberger H, Baum T, et al. Diffusion-weighted stimulated echo acquisition mode (DW-STEAM) MR spectroscopy to measure fat unsaturation in regions with low proton-density fat fraction. *Magn Reson Med*. 2016;75:32–41.
18. Hamilton G, Smith DL Jr, Bydder M, Nayak KS, Hu HH. MR properties of brown and white adipose tissues. *J Magn Reson Imaging*. 2011;34:468–473.
19. Rozman C, Reverter JC, Feliu E, Berga L, Rozman M, Climent C. Variations of fat tissue fraction in abnormal human bone-marrow depend both on size and number of adipocytes - a stereologic study. *Blood*. 1990;76:892–895.
20. Guilmineau F, Kulozik U. Influence of a thermal treatment on the functionality of hen's egg yolk in mayonnaise. *J Food Eng*. 2007;78:648–654.
21. Carpenter AE, Jones TR, Lamprecht MR, et al. Cell Profiler: image analysis software for identifying and quantifying cell phenotypes. *Genome Biol*. 2006;7:R100.
22. Gluer CC, Blake G, Lu Y, Blunt BA, Jergas M, Genant HK. Accurate assessment of precision errors - how to measure the reproducibility of bone densitometry techniques. *Osteoporosis Int*. 1995;5:262–270.
23. Mitra PP, Sen PN, Schwartz LM. Short-time behavior of the diffusion-coefficient as a geometrical probe of porous-media. *Phys Rev B Condens Matter*. 1993;47:8565–8574.
24. Gallichan D, Scholz J, Bartsch A, Behrens TE, Robson MD, Miller KL. Addressing a systematic vibration artifact in diffusion-weighted MRI. *Hum Brain Mapp*. 2010;31:193–202.
25. Hu HH. Magnetic resonance of brown adipose tissue: a review of current techniques. *Crit Rev Biomed Eng*. 2015;43:161–181.
26. Karampinos DC, Weidlich D, Wu M, Hu HH, Franz D. Techniques and applications of magnetic resonance imaging for studying brown adipose tissue morphometry and function. *Handb Exp Pharmacol*. 2018.

SUPPORTING INFORMATION

Additional supporting information may be found online in the Supporting Information section at the end of the article.

FIGURE S1 Alternative assessment of the 1st repetition of the reproducibility scans in subject 3. Signal decay curves for each mixing time with corresponding exponential fitting of the apparent diffusion constant are shown. The dependency of the diffusion constant on the diffusion time is shown in the lower right corner and yields a restriction barrier diameter of 40.88 μm

FIGURE S2 Alternative assessment of the 2nd repetition of the reproducibility scans in subject 3. Signal decay curves for each mixing time with corresponding exponential fitting of the apparent diffusion constant are shown. The dependency of the diffusion constant on the diffusion time is shown in the lower right corner and yields a restriction barrier diameter of 50.41 µm

FIGURE S3 Alternative assessment of the 3rd repetition of the reproducibility scans in subject 3. Signal decay curves for each mixing time with corresponding exponential fitting of the apparent diffusion constant are shown. The dependency of the diffusion constant on the diffusion time is shown in the lower right corner and yields a restriction barrier diameter of 36.66 µm

FIGURE S4 Monte Carlo simulation of the droplet size estimation for different peak area SNR levels in (A) phantom and (B) in vivo conditions. The calculations were performed with fitting Equation S1 proposed by Zielinski et al. The experimentally determined peak area SNR is also shown by the vertical yellow line. A decreased peak SNR leads a higher SD. The dependency of the mean estimated diameter on the SNR is different for the in vivo and phantom cases and there seems to be a systematic offset between the theoretical diameter of 60 µm and the obtained values by the fitting

FIGURE S5 Comparison of the SD of the fitting by the 2-step approach using the model of Zielinski and by the single-step approach using the model of Murday and Cotts. In general, the SD is lower when using the full model of Murday and Cotts compared with Zielinski for the phantom and the in vivo case

FIGURE S6 Effect of the outlier removal on the results of the reproducibility analysis. When no outlier removal is performed, the SD of the apparent measured diameter is greatly increased

6.2 Journal Publication II:
Reduction of vibration-induced signal loss by matching mechanical vibrational states: Application in high b-value diffusion-weighted MRS

The publication entitled *Reduction of vibration-induced signal loss by matching mechanical vibrational states: Application in high b-value diffusion-weighted MRS* was published in Magnetic Resonance in Medicine (ISSN: 0740-3194) [128]. The manuscript was authored by Dominik Weidlich, Mark Zamskiy, Marcus Maeder, Stefan Ruschke, Steffen Marburg and Dimitrios C. Karampinos. It is available online (DOI: 10.1002/mrm.28128) as an open access article under the terms of the Creative Commons Attribution-NonCommercial-NoDerivs License. Preliminary results were presented in the conference contribution C6, which was selected as an oral presentation at the ISMRM annual meeting 2020. Additional to that, parts of the work were presented as a power pitch (C12) at the ISMRM Workshop on MRI of Obesity and Metabolic Disorders 2019. A summary of the publication is provided in Section 6.2.1, the author contributions are listed in Section 6.2.2 and the full text is included subsequently on the following pages.

6.2.1 Abstract

Purpose

Diffusion encoding gradients are known to yield vibrations of the typical clinical MR scanner hardware with a frequency of 20 to 30 Hz, which may lead to signal loss in diffusion-weighted MR measurements. This work proposes to mitigate vibration-induced signal loss by introducing a vibration-matching gradient (VMG) to match vibrational states during the 2 diffusion gradient pulses.

Methods

A theoretical description of displacements induced by gradient switching was introduced and modeled by a 2-mass-spring-damper system. An additional preceding VMG mimicking timing and properties of the diffusion encoding gradients was added to a high b -value diffusion-weighted MR spectroscopy sequence. Laser interferometry was employed to measure 3D displacements of a phantom surface. Lipid ADC was assessed in water–fat phantoms and in vivo in the tibial bone marrow of 3 volunteers.

Results

The modeling and the laser interferometer measurements revealed that the displacement curves are more similar during the 2 diffusion gradients with the VMG compared to the standard sequence, resulting in less signal loss of the diffusion-weighted signal. Phantom results showed lipid ADC overestimation up to 119 % with the standard sequence and an error of 5.5 % with the VMG. An 18 % to 35 % lower coefficient of variation was obtained for in vivo lipid ADC measurement when employing the VMG.

Conclusion

The application of the VMG reduces the signal loss introduced by hardware vibrations in a high b-value diffusion-weighted MRS sequence in phantoms and in vivo. Reference measurements based on laser interferometry and mechanical modelling confirmed the findings.

6.2.2 Author contributions

The first author performed the experiments (MR measurements), programmed the magnetic resonance pulse sequence (propriety hardware specific libraries and software from Philips Medical Systems (Best, The Netherlands)), programmed the mechanical simulations, implemented the post-processing and the quantification process. With the help and consultation form the coauthors, the first author designed the experiment, manufactured the oil-in-water-emulsion phantoms, analyzed and interpreted the data, and wrote the manuscript.

Magnetic Resonance in Medicine

Reduction of vibration-induced signal loss by matching mechanical vibrational states: Application in high b-value diffusion-weighted MRS

Dominik Weidlich[1] iD　|　**Mark Zamskiy[1]**　|　**Marcus Maeder[2]** iD　|　**Stefan Ruschke[1]** iD　|
Steffen Marburg[2]　|　**Dimitrios C. Karampinos[1]** iD

[1]Department of Diagnostic and Interventional Radiology, School of Medicine, Technical University of Munich, Munich, Germany

[2]Chair of Vibroacoustics of Vehicles and Machines, Technical University of Munich, Garching, Germany

Correspondence
Dominik Weidlich, Department of Diagnostic and Interventional Radiology, Klinikum rechts der Isar, School of Medicine, Technical University of Munich, Ismaninger St. 22, 81675 Munich, Germany.
Email: dominik.weidlich@tum.de

Purpose: Diffusion encoding gradients are known to yield vibrations of the typical clinical MR scanner hardware with a frequency of 20 to 30 Hz, which may lead to signal loss in diffusion-weighted MR measurements. This work proposes to mitigate vibration-induced signal loss by introducing a vibration-matching gradient (VMG) to match vibrational states during the 2 diffusion gradient pulses.

Theory and Methods: A theoretical description of displacements induced by gradient switching was introduced and modeled by a 2-mass-spring-damper system. An additional preceding VMG mimicking timing and properties of the diffusion encoding gradients was added to a high b-value diffusion-weighted MR spectroscopy sequence. Laser interferometry was employed to measure 3D displacements of a phantom surface. Lipid ADC was assessed in water–fat phantoms and in vivo in the tibial bone marrow of 3 volunteers.

Results: The modeling and the laser interferometer measurements revealed that the displacement curves are more similar during the 2 diffusion gradients with the VMG compared to the standard sequence, resulting in less signal loss of the diffusion-weighted signal. Phantom results showed lipid ADC overestimation up to 119% with the standard sequence and an error of 5.5% with the VMG. An 18% to 35% lower coefficient of variation was obtained for in vivo lipid ADC measurement when employing the VMG.

Conclusion: The application of the VMG reduces the signal loss introduced by hardware vibrations in a high b-value diffusion-weighted MRS sequence in phantoms and in vivo. Reference measurements based on laser interferometry and mechanical modelling confirmed the findings.

KEYWORDS
artifact reduction, diffusion weighting, high b-value, mechanical vibrations, scanner table vibrations

---

1 | INTRODUCTION

Diffusion-weighted (DW) MR is a powerful tool for the non-invasive assessment of tissue microstructure and is widely applied in the clinical routine as well as in research applications.[1] Sensitizing the MR measurement to diffusion requires strong diffusion-encoding gradients, bringing up technical challenges related to increased sensitivity to motion effects,[2] eddy currents,[3] and scanner table vibrations.[4] Specifically, diffusion-encoding gradients were shown to yield vibrations of the scanner hardware (e.g., scanner table vibrations during diffusion tensor imaging with a frequency of 20-30 Hz and amplitudes up to 100 µm).[5] The observed vibrations were so strong that even elastography experiments utilizing the table vibrations as the main source of mechanical actuation have been proposed.[6] The observed influences of additional vibration-induced motion include reports of signal loss in brain DW images[7,8] and reports of increased lipid ADC measures in subcutaneous fat in regions close to the scanner table.[4]

Multiple research applications require particularly high b-values diffusion measurements, including high-resolution diffusion tensor imaging of the brain[9] or the assessment of fat microstructure with diffusion MRI.[10-12] Specifically, measuring the diffusion properties of lipids has been proven to be challenging because fat has a diffusion coefficient approximately 2 orders of magnitude lower than water due to the large molecular size.[4,13] The assessment of fat microstructure is important in the study of adipose tissue and ectopic lipids in both healthy subjects and subjects affected by metabolic dysfunction across organs and tissues. The quantification of lipid droplet size with DW MR is of great interest in skeletal muscle research,[14] in metabolic research differentiating brown and white adipocytes,[15] and in bone marrow research aiming at the quantification of bone marrow adipocyte size.[16]

Measuring high-resolution diffusion features or diffusion restriction effects requires the acquisition of an artifact-free DW signal while employing high b-values. Given that the gradient strength of clinical MR scanners is limited, high b-values are typically associated with long diffusion gradients at the maximum allowed gradient amplitude. Scanner table vibration effects induced by the long and strong diffusion gradients can become significant at certain frequencies of the scanner hardware mechanical system.[5]

Any motion during the diffusion sensitizing period induces an additional accumulated phase and eventually leads to signal cancellations due to intravoxel dephasing.[17] The amount of the intravoxel dephasing by motion scales at a first approximation with the first gradient moment. Tissue displacements induced by mechanical vibrations introduce such intravoxel dephasing. The amount of intravoxel dephasing increases in the presence of strong and long diffusion encoding gradients. Therefore, tissue displacements induced by mechanical vibrations at high b-value scanning compromise the reliability of the measured DW signal for any subsequent analysis aiming at the extraction of quantitative diffusion parameters.

The present work proposes the application of an additional gradient before the actual diffusion sensitizing period to mitigate signal loss induced by scanner table vibrations. The benefits of the proposed approach are shown by modeling a simplified mechanical model and the quantification of the scanner table displacements with and without the additional gradient by doppler laser interferometry. Afterward, the approach is tested measuring lipid ADC with a DW MRS sequence in water–fat (WF) phantoms and in vivo in the tibial bone marrow of healthy volunteers.

2 | THEORY

2.1 | Mechanical description

Modulation of magnetic field gradients is an essential element of most MR pulse sequences. Alterations of the magnetic gradient strength or polarity are achieved by changing the current in the respective gradient coil. Time-varying currents in the strong main magnetic field result in Lorentz forces on the gradient coil. The mechanical vibrations of the MR hardware components are eventually caused by the impact of the gradient coils on the mounting during the MR experiment.[18] The Lorentz forces on the gradient coils also induce vibrations of the MR scanner table that are subsequently transferred to the object that is examined. The propagation of the vibrations within the object and the damping of the displacement amplitude are dependent on the mechanical properties of the system. Consequently, the forces on the MR gradient hardware can induce time-varying displacements within the subject or object being scanned.

However, the exact displacement pattern within the tissue might be difficult to predict. Although the vibrations do not originate from the scanner table, the observed vibrations will be referred to as scanner table vibrations.

2.2 | MR diffusion encoding

Using MR, diffusion properties can be probed using 2 diffusion encoding gradients and a time interval between these 2 diffusion encoding gradients[19] (Figure 1). The accumulated phase during the first diffusion encoding gradient (DG_1) is recovered by the accumulated phase during the second diffusion gradient (DG_2) for stationary spins. For moving spins, any phase dispersion is not recovered and consequently leads to signal loss. In the absence of any macroscopic motion or flow effects, the strength of the signal loss reflects the self-diffusion of the particles; therefore, information about the
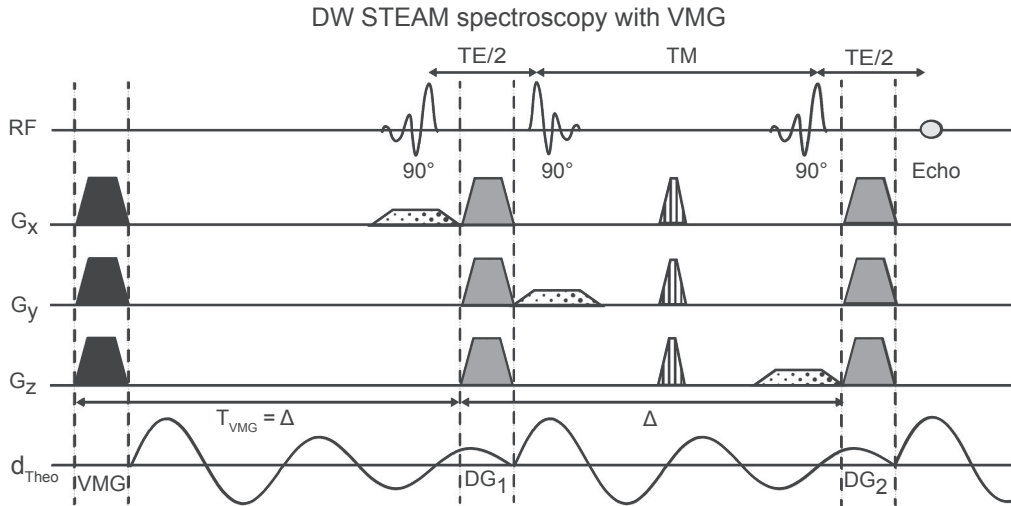
FIGURE 1 Sequence diagram of the DW-STEAM sequence with the proposed VMG (in black) and corresponding d_{Theo} induced by the strong gradient waveforms. The DW-STEAM magnetization preparation consists of 3 slice-selective 90° RF pulses and monopolar diffusion sensitizing gradients (in gray). Spoiler gradients (vertical stripes) and slice selective gradients (dots) are also shown. Both the VMG and the diffusion gradients will lead to tissue displacements. If a VMG is introduced with appropriate timing, the tissue displacement pattern is similar during DG_1 and DG_2. Δ, diffusion time; DG_1, first diffusion gradient; DG_2, second diffusion gradient; d_{Theo}, theoretical tissue displacement; DW, diffusion-weighted; TM, mixing time; T_{VMG}, timing of vibration-matching gradient; VMG, vibration-matching gradient

tissue microstructure can be extracted. Mathematically, the accumulated phase ϕ at time t for a spin located at position $\vec{r}_0$ at time $t = 0$ can be expressed as:

$$\phi\left(\vec{r}_0, t\right) = \gamma \int_0^t \vec{G}\left(t'\right) \cdot \vec{r}\left(\vec{r}_0, t'\right) dt', \qquad (1)$$

where γ is the gyromagnetic ratio; $\vec{G}$ is the magnetic field gradient; and $\vec{r}\left(\vec{r}_0, t'\right)$ is the location at time t for a spin located at position $\vec{r}_0$ at time $t = 0$. The total signal S acquired from a defined volume of spins can be expressed as:

$$S\left(t\right) = S_0 \int e^{-i\phi(\vec{r}_0, t)} d\vec{r}_0. \qquad (2)$$

Any additional accumulated phase that is not due to diffusion can lead to additional signal decay and consequently results in quantification errors.

2.3 | MR diffusion encoding in the presence of vibrations

The bottom row of Figure 1 depicts a schematic view of the displacements induced by DG_1 that will be present during the presence of DG_2. Assuming a simple diffusion encoding scheme with a time separation and a refocusing element between the 2 diffusion weighting gradients and assuming rectangular gradients, the phase at the end of the DW can be expressed as:

$$\phi\left(\vec{r}_0, \Delta + \delta\right) = \gamma G \left[\int_0^\delta \vec{r}\left(\vec{r}_0, t'\right) dt' - \int_\Delta^{\Delta+\delta} \vec{r}\left(\vec{r}_0, t'\right) dt'\right]. \qquad (3)$$

Here, δ is the length of the DW gradient, and Δ is the diffusion time. When the spins are affected only by the motion due to vibrations (assuming no diffusion or flow effects), only the displacements from the equilibrium position ($\vec{d}$) can be considered. The second integral can be simplified by a coordinate transformation:

$$\phi\left(\vec{r}_0, \Delta + \delta\right) = \gamma G \left[\int_0^\delta \vec{d}\left(\vec{r}_0, t'\right) dt' - \int_0^\delta \vec{d}\left(\vec{r}_0, t' + \Delta\right) dt'\right]$$
$$= \gamma G \int_0^\delta \left[\vec{d}\left(\vec{r}_0, t'\right) - \vec{d}\left(\vec{r}_0, t' + \Delta\right)\right] dt' \qquad (4)$$

$$S = S_0 \int e^{-i\phi(\vec{r}_0, \Delta+\delta)} d\vec{r}_0 = S_0 \int e^{-i\gamma G \int_0^\delta \left[\vec{d}(\vec{r}_0, t') - \vec{d}(\vec{r}_0, t'+\Delta)\right] dt'} d\vec{r}_0. \qquad (5)$$

Equation 5 shows that signal loss due to vibrational displacements can occur when the displacements during the 2 diffusion gradient durations (DG_1 und DG_2) differ. Larger voxel sizes and stronger first gradient moments amplify this signal loss.[17] To minimize the phase dispersion within a voxel, the following condition should be fulfilled for all spins:

$$\vec{d}\left(\vec{r}_0, t\right) = \vec{d}\left(\vec{r}_0, t + \Delta\right) \quad \text{for } 0 < t < \delta. \qquad (6)$$

This condition is not fulfilled in a standard DW sequence. DG_1 will introduce tissue displacements that in general are

different between DG_2 and DG_1. To match tissue displacements between DG_1 and DG_2 and mitigate signal loss, an additional gradient can be introduced to induce vibrations during DG_1 similar to the vibrations induced by the first diffusion gradient during DG_2. The additional gradient replicating the vibrational patterns is called vibration-matching gradient (VMG).

If the VMG is placed before DG_1 with appropriate timing, the tissue displacement pattern can become similar during both diffusion encoding gradients. The introduction of the VMG is shown in Figure 1 (see upper row). The VMG is applied before the RF excitation pulse of the diffusion sensitizing module and does not interfere with the transverse magnetization but solely induces a mechanical vibration state. When the time interval between the VMG and DG_1 is equal to the diffusion time, the tissue displacement caused by scanner table vibrations during the 2 diffusion gradients should be similar. Therefore, the accumulated phase during the diffusion encoding is similar, and the occurring signal loss can be mitigated. The mechanical vibrational pattern during the 2 diffusion gradients may become similar for other timings of the additional gradient. However, the exact optimal timing, which is when the time interval between the VMG and the DG_1 is not equal to the diffusion time, will depend on the frequency of the vibration, the coupling of the components, and the damping of the vibrations; thus, it is not easily predictable.

2.4 | Mechanical modeling of a 2-mass-spring-damper system

Most biological soft tissues can be modeled as viscoelastic materials.[20] The viscoelastic material model comprises of an elastic (spring-like) and viscous or damping (dashpot-like) response to an external force. Mathematical models have been developed to predict the dynamics and the response of viscoelastic materials.[21] The field of MR elastography deploys these models and tries to map tissue properties after intentionally applying a defined actuation to the investigated tissue during a special MR examination.[20] However, there are also involuntary actuations due to the MR scanner table, as described above. To illustrate the behavior of a viscoelastic material that is excited by an external force, the displacement of 2 masses that are connected in a spring-damper system was investigated in 1D. The system is decribed in Figure 2B, where the 2 masses could represent 2 isochromats within the viscoelastic material. They should be embedded in the material; therefore, both are connected to a larger pool represented as a fixed boundary. The excitation of the system by scanner table vibrations was represented by instantaneous force impulses on mass 1 whenever there was a gradient switching in the gradient pulse sequence shown in Figure 2A. A different direction of the impulse was assumed for different polarities of the gradient slope. It was assumed that there
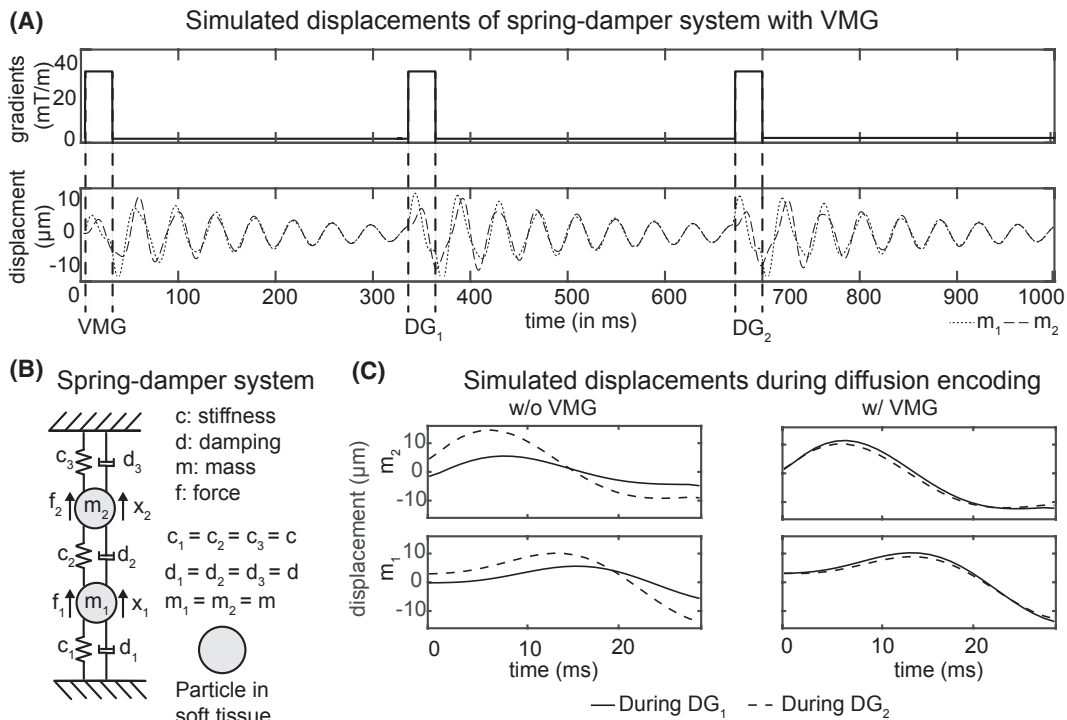

FIGURE 2 Simulated displacements during diffusion gradients assuming a 2-mass-spring-damper system (schematic B). Plot A shows the strong gradient waveforms within the pulse sequence and the corresponding simulated displacement of m_1 and m_2 when the VMG and the 2 diffusion gradients are simulated. Plot C shows the displacement of the 2 masses during DG_1 and DG_2. The displacements of the 2 masses are different without the VMG, whereas the displacements of the 2 masses are very similar with the VMG. m_1, mass 1; m_2, mass 2

was no additional force on mass 2. In the pulse sequence shown in Figure 2, the system was consequently excited by 4 Dirac impulses when no VMG was applied and was excited by 6 Dirac impulses when the VMG was employed. A mathematical derivation of equation of motion is given in the Supporting Information following Voeth et al.[22] The magnitude of the stiffness parameter of an unknown material can be estimated by the frequency of the induced vibration assuming an undamped oscillation ($c \approx 4\pi^2 m f^2$). To the best of the authors' knowledge, the mechanical parameters for adipose tissue assuming a simple 1D spring-damper system are not available in current literature.

The following parameters were assumed: mass $m = 0.5$ kg; stiffness c (25 Hz undamped oscillation) = 12,337 $\frac{N}{m}$; damping d was selected to be 5 $\frac{kg}{s}$ to achieve a similar damping as observed in the interferometer measurements; and the amplitude of the force impulse was selected to give a displacement amplitude equal to 10 μm. The system was solved for the gradient pulse sequence shown in Figure 2A with and without the VMG by means of numerical integration (Figure 2A).

3 | METHODS

3.1 | DW-MRS pulse sequence and spectrum analysis

To test the proposed method, the diffusion properties of lipids were measured with a bipolar DW STEAM MRS sequence (Figure 1). The sequence was based on a standard single-voxel STEAM MRS, with gradients added after the first and third RF pulse to induce diffusion-weighting. Half of the DW spectra were acquired with positive diffusion gradient polarity and half with negative. The DW spectra with opposite diffusion gradient polarity were used to estimate and compensate for eddy-current effects.[23] To mitigate the effect of vibration-induced tissue displacements on the DW signal, the VMG with identical gradient duration and amplitude properties to the diffusion sensitizing gradients was placed before the actual sequence. The data processing included zero order phasing and Gaussian apodization. The single averages were frequency-aligned, and averages with a deviation of the methylene peak amplitude of more than 2 SDs from the mean methylene peak amplitude were identified as outliers and excluded from the subsequent analysis. The remaining averages for both polarities were combined and corrected for eddy currents. Peak area quantification was performed on the real spectrum fitting 8 fat peaks assuming Voigt peak shapes. The fat peaks included were methyl at 0.90 parts per million (ppm), methylene at 1.30 ppm, β-carboxyl at 1.60 ppm, α-olefinic at 2.02 ppm, and α-carboxyl at 2.24 ppm, diallylic methylene at 2.75 ppm, glycerol at 4.20 ppm, and olefinic at

5.29 ppm.[23] Water signal was not detectable due to the strong diffusion-weighting. Only the methylene peak area (at 1.3 ppm) was used for further analysis because of the large peak area. ADC was determined by an exponential fitting of the methylene peak area as a function of *b*-value.

3.2 | Laser interferometer setup

To quantify the scanner table vibrations during the MR measurements, the displacements of the scanner table were measured by utilizing laser doppler interferometry (PSV-500-3D-Xtra, Polytec GmbH, Waldbronn, Germany). The interferometer setup was placed within the scanner room with a sufficient distance from the MR scanner such that the local magnetic field did not exceed 1 mT. The interferometer used infrared light with a wavelength of 1550 nm and a specific power of $P < 10$ mW. This way, it was possible to measure the table surface as well as the relative structural vibrations of the phantoms surface. With the setup at hand, a measurement sensitivity of 0.1 μm/s of the surface velocity could be realized. A schematic setup is shown in Figure 3.

3.3 | Laser interferometer measurements

Three different phantoms were utilized in the phantom measurements. For the lipid diffusion property measurements, 2 WF phantoms with 80% fat fraction were produced (content: 800 mL sunflower oil, 200 mL water, 4 mL Tween80, and 1 g of sodium benzoate). Emulsification was carried out with a colloid mill at 6000 and 11,000 revolutions per minute (rpm). The obtained phantoms yield different lipid droplet sizes and consequently different viscosities. However, the content of the WF phantoms was fluid. For the interferometer measurement reflective spray had to be attached to the phantom surface, and the experiment had to be performed with an open lid to directly measure on the phantom material. Therefore, the experiments with the laser interferometer were performed with an agar phantom (4% agar) that consisted of a solid material. All MR phantom experiments were performed with a 3 Tesla scanner (Ingenia Elition, Philips, Best) using an 8-channel wrist coil with the following common sequence parameters: Volume of Interest = $(15 \text{ mm})^3$, TE = 60 ms, TM = 300 ms, TR = 1800 ms. The experiments were performed on the scanner table and on a decoupling table made of wood (Figure 3B) that decoupled the sample from the vibrating scanner table. The following 2 interferometer experiments were performed with the interferometer setup to quantify the effects under investigation.

First, the agar phantom was placed on the scanner table, and a high *b*-value DW MRS experiment with a *b*-value of

(A) Scenario 1: sample on scanner table

(B) Scenario 2: sample on decoupling table

(C) Phantom in writst coil

(D) Measured points
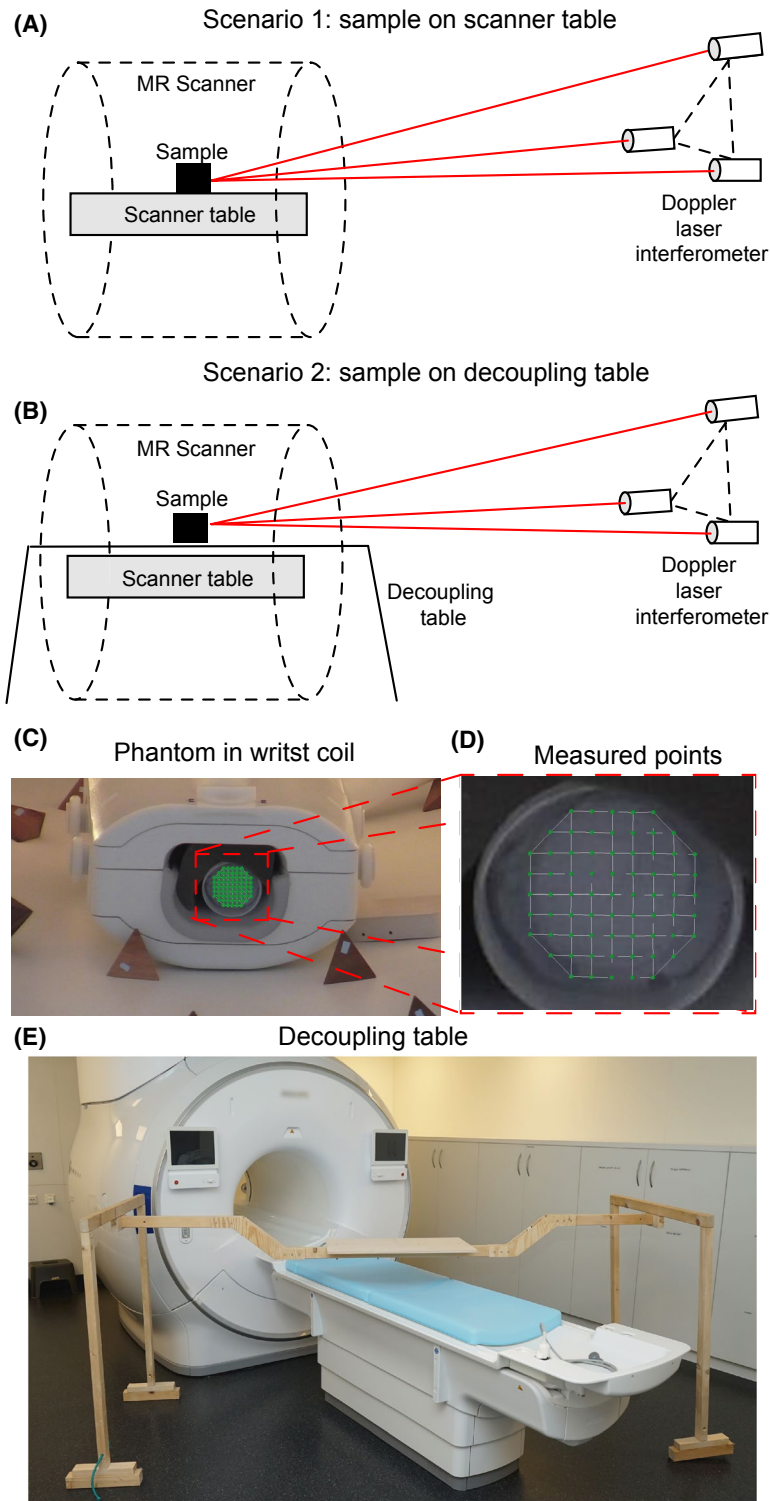

(E) Decoupling table

FIGURE 3 Experimental setup of the doppler laser interferometer measurement. 2 measurement scenarios can be distinguished: In the first scenario, the sample was measured directly on the scanner table (plot A). In the second scenario, the sample was placed on a decoupling table (plot B). The 3D displacement on the surface of a phantom was measured simultaneously from 3 doppler laser interferometers during the MR experiment to disentangle the displacements in all 3 spatial components. Plot C shows the measured agar phantom in the wrist coil, and plot D shows a zoom-in picture on the points that were measured on the top of the phantom surface. When only 1 spatial point was measured, the measurement point was placed in the middle of the surface. Plot E shows the decoupling wooden table

50,000 s/mm^2 was performed while varying the timing of the VMG from 50 ms to 650 ms in 5 ms steps.

Next, the laser was placed on a point in the middle of the phantom surface (Figure 3D), and the displacements in all 3 dimensions were acquired with 2 averages per timing. The 2 averages were combined, and the displacements during both diffusion gradients were extracted for each timing of the VMG. As a next step, the total accumulated phase was

calculated based on Equation 3. The experiment was repeated with the 6000 rpm WF phantom without measuring displacements using the laser interferometer, and the methylene peak amplitude was extracted for different timings of the VMG.

Second, the timing of the VMG relative to DG_1 was set to match the diffusion time, and the displacements were acquired on the whole 2D surface of the agar phantom (70 measurement points) to investigate the phase dispersion

on a 2D surface. The experiment was repeated for 3 different measurement scenarios: without VMG and coil placed on the scanner table, with VMG and coil placed on scanner table, and without VMG and coil placed on the decoupling table. The accumulated phase was then calculated for each point, and the total signal within the 2D surface was calculated similar to Equation 5:

$$S = \sum_{n=1}^{N} e^{-i\phi_n}. \qquad (7)$$

Here, N is the number of total measurement points (measurement points on the edge were excluded to avoid measurement artifacts due to the coupling to the probe holder). The signal on the scanner table was compared relative to the signal acquired on the decoupling table.

3.4 | ADC measurements in phantoms

To evaluate the performance of the proposed scheme, the lipid ADC value was estimated within the WF phantoms (6000 and 11,000 rpm). The voxel of interest was placed in the middle of the WF phantom material. The experiment was repeated for the same 3 different measurement scenarios as performed in the interferometer measurements and with the same scanning parameters. The utilized additional sequence parameters were: 16 averages per b-value (half of the averages with positive and the other half with negative polarity), 1 startup cycle, b-values = 10,000 – 20,000 – 40,000 – 60,000 s/mm^2, 2:48 min scan time per phantom. Diffusion gradients were applied simultaneously in all 3 axes to minimize TE.

3.5 | ADC measurements in vivo

The bone marrow in the tibia of 3 healthy volunteers (volunteer 1: 24 years/85 kg; volunteer 2: 29 years/57 kg; volunteer 3: 28 years/80 kg) was scanned using an 8-channel extremity coil without and with the VMG and with different additional weight placed on the scanner table (0/10/20 kg). By changing the loading of the scanner table, the mechanical vibrations were altered, and the influence of the vibrations on the DW measurement could be investigated. Each scan was repeated 3 times to access the reproducibility of the ADC measurement. The DW MRS voxel was placed approximately 1 cm below the growth plate in the tibia bone marrow and was performed with the same parameters as the phantom scans (including the same diffusion directions and b-values). Afterwards, the lipid ADC was extracted for each loading without and with the VMG.

4 | RESULTS

4.1 | Mechanical modeling of a 2-mass-spring-damper system

Figure 2 shows the results of the modeling of the mechanical system when actuated by the gradient pulse sequence depicted in the Figure 2A. The amplitude of the displacements during DG$_1$ are smaller compared to the displacements during DG$_2$ for both masses without the VMG. In addition, the shape of the displacements is different during both diffusion gradient durations when no VMG is employed, resulting in an additional phase accumulation when a magnetic field gradient is employed in the direction of the displacement. The amount of accumulated phase is thus different for both masses because the displacement curves also differ in their appearance without the VMG. With the VMG, the simulated displacement curves during both diffusion gradient durations and for both simulated masses are very similar. Such a phase accumulation pattern would result in a negligible phase difference between the 2 masses, inferring a minimal intramass dephasing when the phase of the 2 masses is combined.

4.2 | Quantification of scanner table vibrations by laser interferometry

Figure 4 shows the measured displacements on the agar phantom for 3 different measurement scenarios: without VMG on the scanner table, with VMG on the scanner table, and without VMG on the decoupling table. In general, the displacement in z-direction (feet-head) is small in all 3 measurements compared to the other components. In x-direction (right-left), minor deviations in the displacement can be seen in all 3 measurement scenarios. In y-direction (anterior-posterior), the displacements show an offset during the first and second diffusion gradient duration when the phantoms are placed on the scanner without the VMG, whereas the displacement patterns during the 2 diffusion gradients are very similar when the VMG is additionally employed. On the decoupling table, the displacements patterns are very similar and small for all components and show a very low- and very high-frequency component compared to the 20 to 25 Hz vibration visible on the results on the scanner table.

In Figure 5, the pulse sequence with the corresponding displacements during both diffusion gradients (DG$_1$ and DG$_2$) can be seen for 3 different timings of the VMG. Visually, a great difference in the displacement patterns can be seen when the timing of the additional gradient is much smaller or much larger than the diffusion time. Large differences in the displacements during the diffusion weighting gradients lead to accumulated phase that is not rephased and can lead
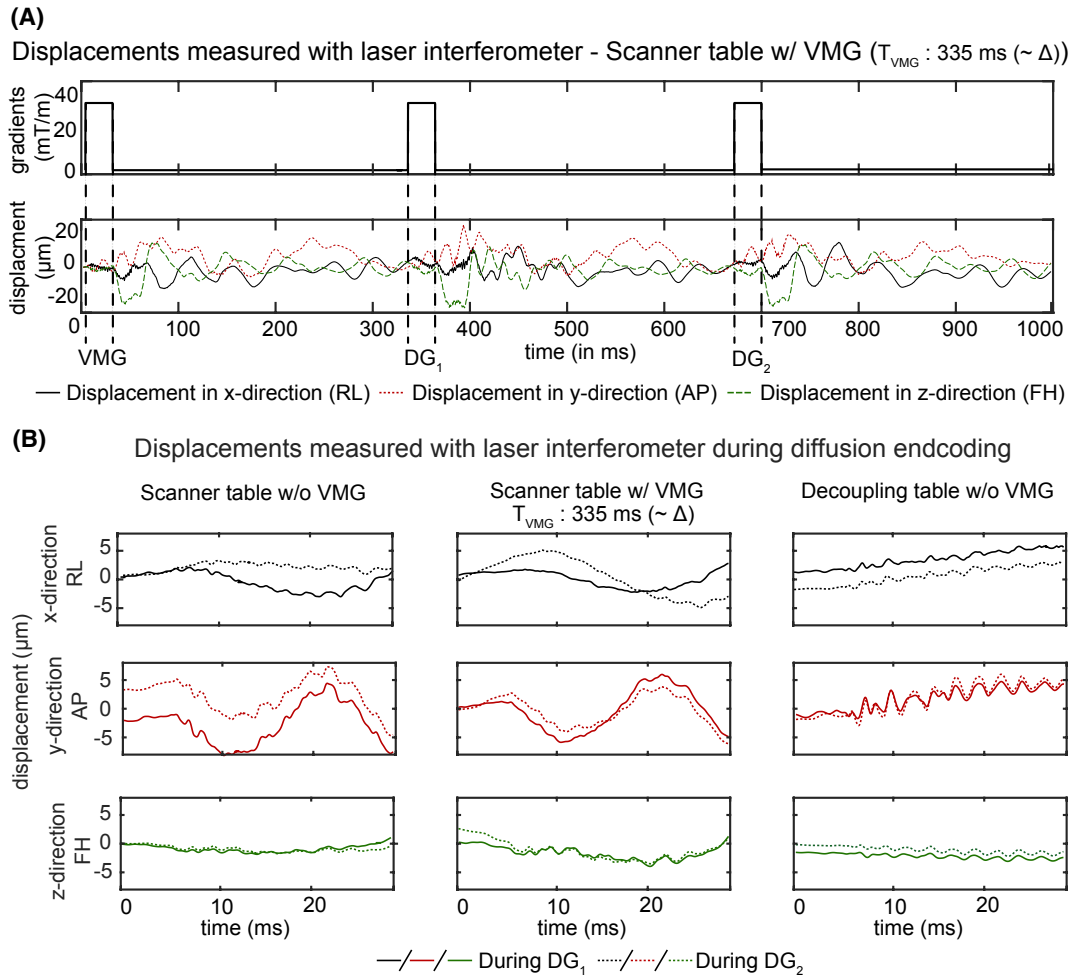
(A)

Displacements measured with laser interferometer - Scanner table w/ VMG (T_{VMG} : 335 ms (~ Δ))

— Displacement in x-direction (RL) ···· Displacement in y-direction (AP) --- Displacement in z-direction (FH)

(B)

Displacements measured with laser interferometer during diffusion endcoding

—/—/— During DG₁ ·····/·····/····· During DG₂

FIGURE 4 Measured displacements with laser interferometry when the T_{VMG} matched the diffusion time (Δ) (subplot A). Subplot B shows the *x*, *y*, and z displacements during DG₁ and DG₂ for 3 different measurement scenarios (different rows). Without the VMG, large differences between the displacement patterns can be seen compared to the case with the VMG (especially in *y* direction). Displacements are also visible with the decoupling table but follow the same patterns during both diffusion gradients

to signal loss. When the timing of the VMG is similar to the diffusion time, the displacement curves are similar.

Based on the displacement curves and the employed gradients, the phase difference for each VMG timing can be calculated based on Equation 4. Figure 6 shows the additional accumulated phase by vibrational displacements and compares it to the methylene peak amplitude acquired in a separate scan with the WF phantom. In general, areas with high and low accumulated phase can be observed with a similar pattern as the methylene peak area. When the diffusion time matches the VMG timing, a maximum in signal amplitude with corresponding minimum in the accumulated phase can be observed.

Figure 7 shows the accumulated phase that was calculated for a 2D surface on the agar phantom for different scenarios of phantom placement.

When the phantom is placed on the scanner table without the VMG, the accumulated phase during the diffusion weighting gradient has larger variations when compared to

the scenario with the VMG. This results in a relative signal of 95% on the scanner table without the VMG compared to the signal on the decoupling table without the VMG. A relative signal of 99% on the scanner table with the VMG compared to the signal on the decoupling table without the VMG is observed.

4.3 | Lipid ADC measurements in phantoms

Figure 8 shows the results from the phantom scans. Assuming that the phantoms on the decoupling table are not affected by vibration artifacts, the ADC value on the decoupling table represents the real lipid ADC value. In the 6000 rpm phantom, the DW MRS experiment on the scanner table yields to a 119.0% overestimation of the ADC value, whereas only a relative error of 5.5% is observed on the scanner table with the VMG. In the 11,000 rpm phantom, the obtained lipid ADC value is very similar between the different
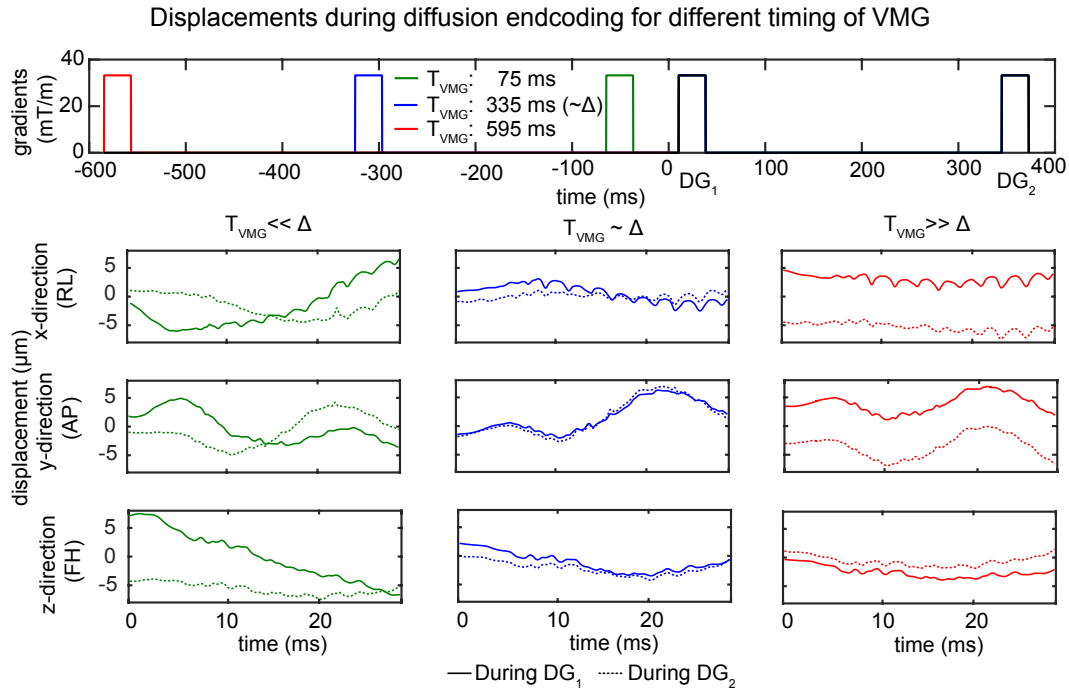
FIGURE 5 Measured x, y, and z displacements with laser interferometry during DG_1 and DG_2 for 3 different timings of the VMG. The first row shows the corresponding gradient pulse sequence. When the T_{VMG} is much smaller or larger than Δ, large variations of the displacements can be observed. When the T_{VMG} is equal to Δ, the displacement patterns are very similar
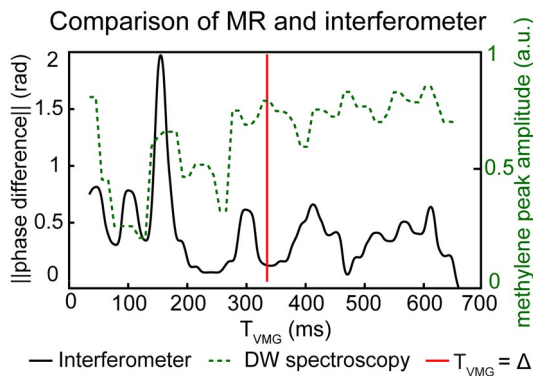

FIGURE 6 Accumulated phase on single point based on displacements measured with laser interferometry on the phantom surface (solid line) and methylene peak area acquired by DW-MRS for different T_{VMG} is shown. A maximum in signal amplitude corresponds to a minimum of acquired phase when T_{VMG} is equal to the Δ. Multiple minima of the phase and maxima of the methylene peak area can be observed

measurement scenarios, and only relative differences below 1% are observed.

4.4 | Lipid ADC measurements in vivo

Figure 9 shows the mean obtained ADC value in the tibia bone marrow, with corresponding SD of the 3 repeated measurements with different loading of the scanner table. Without

the VMG, a dependency of the measured ADC value on the additional loading of the scanner table is observed, and a larger SD of the lipid ADC estimation is observed. The ADC value combined from the different measurement is comparable with and without VMG. However, the coefficient of variation is reduced by 34.9% (volunteer 1), 18.9% (volunteer 2), and 24.0% (volunteer 3) in the 3 volunteers, comparing the measurement without the VMG to the measurement with the VMG.

5 | DISCUSSION

The present study investigates the influence of mechanical vibrations on the signal of DW-MR measurements, focusing on the example of a high b-value DW MRS sequence and proposing a method to mitigate the signal loss by the application of an additional gradient. The main underlying concept does not eliminate mechanical vibrations but aims to approximately match the vibrational states during both diffusion gradients so that the total intravoxel dephasing is small and will not lead to significant signal loss.

The simplified mechanical system used to illustrate the transfer of vibrations within the tissue does by no means fully represent the complexity of soft tissue viscoelastic mechanics. Due to the adopted simplifications and the absence of accurate values for the mechanical properties, no quantitative analysis was performed, and only qualitative results were
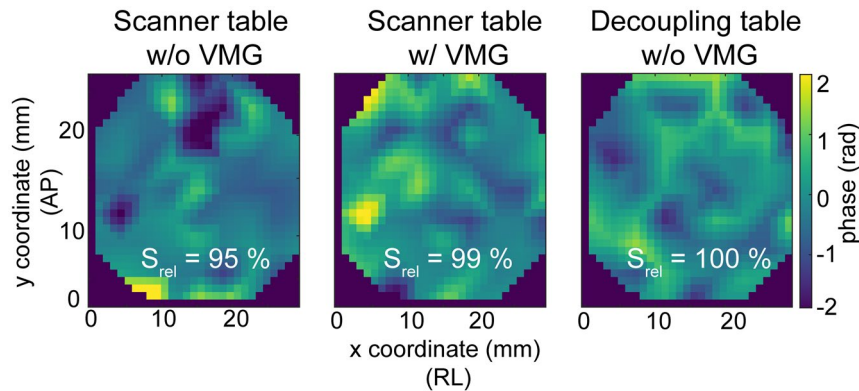
FIGURE 7 Accumulated phase on a 2D surface measured with laser interferometry on top of an agar phantom for 3 different scenarios. (A) phantom placed on the scanner table without VMG, (B) phantom placed on the scanner table with VMG, and (C) phantom placed on the decoupling table without VMG. When the phantom is solely placed on the scanner table, a 5% decay of the total signal can be observed in the measured 2D surface. When the phantoms are placed on the scanner table with the VMG, only a 1% decay of the signal is observed. It is expected that the signal decay will be larger when displacements over a 3D volume instead of over a 2D surface are measured
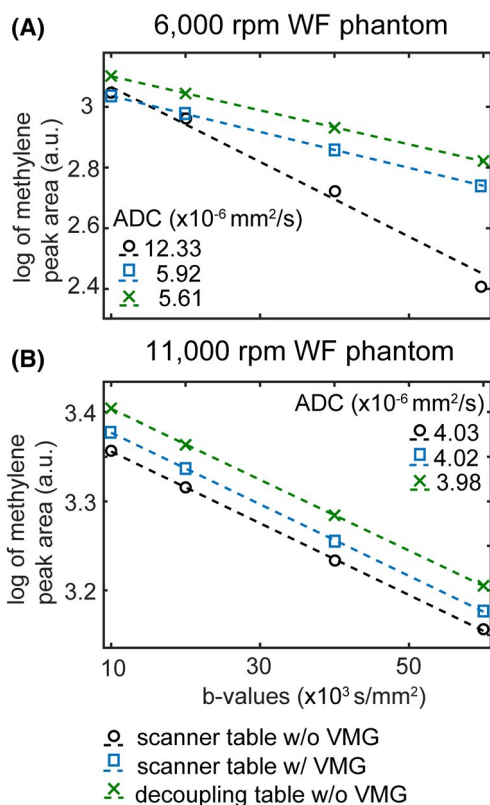
FIGURE 8 ADC determination in 6000 rpm (A) and the 11,000 rpm (B) water–fat (WF) phantoms. In the 6000 rpm phantom, a large difference in the lipid ADC value was observed without the VMG compared to the other 2 measurement scenarios. In the 11,000 rpm phantom, the differences between the measured lipid ADC values were minor. WF, water–fat

shown. The model reveals that the application of the VMG before the actual diffusion-weighting helps to approximately match the displacement patterns during both diffusion gradient durations. This is true for the investigated first mass that is directly excited by the impulse and also for the second mass that is connected to the first mass. When applying the VMG, both masses show a very similar displacement pattern during the diffusion encoding gradients, which would result in a very small accumulated phase during diffusion weighting. When the displacement pattern is different during the 2 diffusion gradients (as in the simulated case without the VMG), phase is accumulated. When this accumulated phase also varies for different positions within the tissue, the phase dispersion would result in signal losses within a voxel. Figure 2 clearly shows this variation of displacement patterns during the 2 diffusion gradient durations for the 2 simulated masses when no VMG is employed.

In Figure 4A, the measured displacements with VMG and T_{VMG} equal to the diffusion time in a real experimental setting are shown. The displacement pattern is similar but more complex than shown in the simplified model (Figure 2A). In Figure 4B, the displacements during the 2 diffusion gradients are depicted. The displacements differ when the phantom is measured on the scanner without applying the VMG and become more similar when the VMG is applied before the DW. This effect is especially prominent in the y-direction (anterior-posterior), whereas the x-direction (right-left) seems to be less affected by the application of the additional gradient. In z-direction (feet-head) the measured displacements are small compared to the other directions.

Displacements are also visible during the diffusion gradient durations when the coil is placed on the decoupling table. However, the displacements when the coil is placed on the decoupling table seem to be very similar during the diffusion gradients and represent much lower frequencies of the system. The decoupling table was manufactured with wood, which could result in low eigenfrequencies of the system. However, high vibrational frequency components can also be observed in anterior-posterior direction. This could potentially reflect
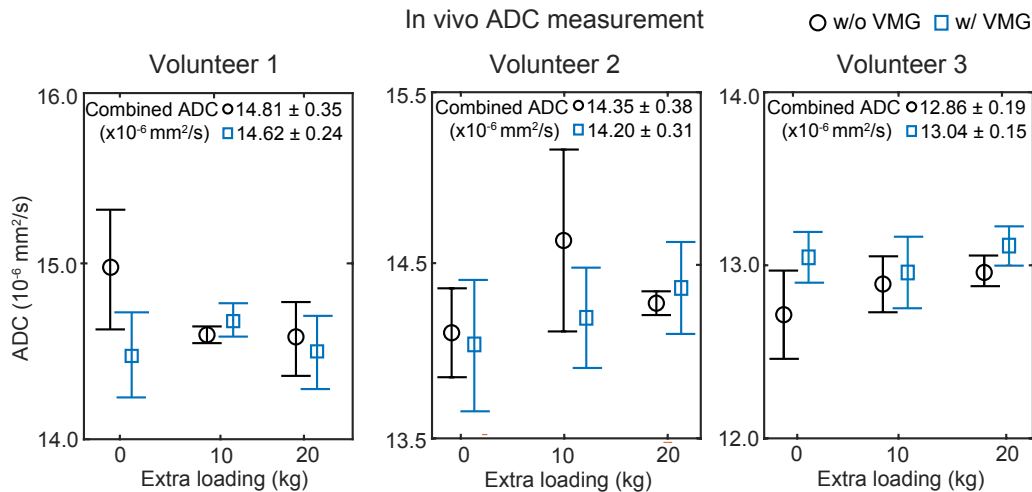
FIGURE 9　In vivo lipid ADC measurement in the tibia bone marrow for different loadings (0–10–20 kg additional weighting) on the scanner table in 3 healthy volunteers. Without the VMG, the measured ADC is dependent on the extra loading of the scanner table, and a larger ADC SD is observed. When all measurements are combined, the coefficient of variation is reduced by 34.9% (volunteer 1), 18.9% (volunteer 2), and 24.0% (volunteer 3) comparing the measurement without the VMG to the measurement with the VMG

the first natural resonance of the wooden decoupling table that is predominately present in anterior-posterior direction. The energy to excite this natural resonance vibration could also be transferred from the gradient coil to the decoupling table via sound waves.

Not only the employment of the VMG is important but also the timing of this additional gradient. Figure 5 shows that the displacement patterns differ greatly (even more compared to the absence of the VMG) when the VMG timing is much shorter or longer than the diffusion time. When the VMG replicates the shape and strength of the DW gradients and the timing of the diffusion preparation, the similarity of the displacement curves is very high.

Based on the measured displacements, the accumulated phase can be estimated and compared to the signal amplitude of a DW MRS scan. The results shown in Figure 6 represent a merging of 2 experiments, which could not be performed simultaneously. Therefore, although the location of the minima in the accumulated phase and maxima in the methylene peak area do not fully match, the pattern in the 2 curves of Figure 6 appears similar. Figure 6 shows that a maximum in the signal amplitude is obtained when the VMG timing relative to DG_1 is equal to the diffusion time. This high signal value corresponds to a minimum in the accumulated phase. The above finding is another illustration of the idea that the signal loss in a DW MR experiment due to vibrational artifacts can be reduced when the displacements during the 2 diffusion gradients are similar and eventually the accumulated phase is small. Figure 6 shows multiple minima in the accumulated phase or maxima in the signal values. However, the occurrence of these extreme values is not easily predictable without the knowledge of the exact mechanical properties of the system. Nevertheless, it can be postulated without any

knowledge of the object properties that a minimum in the accumulated phase occurs when the VMG timing relative to the first diffusion gradient is equal to the diffusion time.

Solely accumulated phase is not sufficient to induce signal loss by intravoxel dephasing. For this effect, a phase dispersion over the 3D voxel needs to be present. To quantify the phase dispersion for more than 1 point, the accumulated phase was calculated on a 2D surface on top of the phantom. The surfaces shown in Figure 7 represent the accumulated phase in each point for different measurement scenarios. Signal loss will occur in DW MR experiments when a large spatial variation of phase is present in 1 acquisition voxel. The phase variation in a 2D surface can already give a hint to the expected signal loss in a 3D volume. When the phantom was scanned on the scanner table without the proposed scheme, a signal loss of 5% already could be observed in the 2D surface, whereas it was only 1% when the VMG was employed. It would be expected that the signal loss in a 3D volume on the scanner table will be higher without the VMG compared to the case with the VMG.

The phantom results in the 2 measured WF phantoms need to be discussed separately: In the 6000 rpm WF phantom, the lipid ADC value is greatly overestimated when the phantom is measured on the scanner table without the proposed method. When the VMG is employed, a great improvement in the measurement of the lipid ADC value can be observed. In the 11,000 rpm WF phantom, the ADC measurement seems to not be affected a lot by vibrations; therefore, the 3 measurement scenarios give very similar lipid ADC values. The differences in both phantoms can be explained by different oil droplet sizes within the 2 phantoms,[12] resulting in different viscoelastic properties of the phantoms: the 11,000 rpm phantom is more viscous than the 6000 rpm

phantom. Therefore, the effect of the vibrations on the overall signal loss is highly dependent on the tissue properties and can vary a lot between different tissue type. However, it should be noted that the VMG does not cause artifacts in the ADC quantification when the estimation without the additional gradient is already sufficient (as can be seen in the 11,000 rpm WF phantom). Therefore, the application of the VMG overall improves the accuracy of the measured lipid ADC value in phantoms.

The coefficient of variation for the estimation of in vivo lipid ADC decreased significantly when the VMG was employed in all 3 volunteers. A correct estimation of the diffusion properties of lipids is particularly important when high order effects such as diffusion restriction effects are investigated.[12] The ADC value changes in an 80-μm diameter fat cell in vivo by approximately 1% per 100 ms diffusion time increase.

Therefore, a high accuracy in the DW signal acquisition is needed. The presented method could be used to improve the quality of DW MR measurements and eventually the accuracy of lipid droplet size estimations.

The proposed study has the following limitations: First, the laser interferometer data and the DW-MRS data were acquired subsequently and not in the same phantom. However, experimental limitations did not allow a simultaneous acquisition in the same phantoms. Consequently, the slight mismatch between the accumulated phase curve and the methylene peak amplitude in Figure 6 could most likely be explained by the different phantom materials with different viscoelastic effects. This difference in the material properties leads to differences in the observed displacement with different frequencies and damping. However, the overall trend is also visible in this merged dataset based on different experiments. Second, the phase dispersion was only measured on a 2D surface and not in a 3D volume. For an accurate estimation of the intravoxel dephasing effect with the corresponding signal loss, the accumulated phase should be calculated for each point in a 3D volume. However, the employed laser interferometer methodology only allows measurements on a surface without depth information. Because phase dispersion effects are even visible on a 2D surface, phase dispersion effects are expected to be present and may be even more severe if the measurements would have been extended to a 3D analysis. The presented measurements do not allow for an accurate quantification of the 3D intravoxel phase dispersion; however, based on the 2D surface information, conclusions can be drawn that the signal loss should be reduced when the VMG is applied.

Another way of reducing vibrational artifacts in diffusion-weighted sequences would be the reduction of acoustic noise produced by the applied gradients. This could be achieved by either matching the frequency of the time-varying diffusion gradient to minima of the scanner gradient response function[24] or by reducing the slew rate of the diffusion gradients. However, the above approaches would lead to less flexibility in the selection of sequence timing and most probably to prolonged TEs.

The proposed approach can be theoretically applied in other DW MR sequences with minor or negligible time penalty by adding the VMG before the start of the diffusion preparation.

An even better matching of the vibrational states might be achieved by extending the VMG and also adding additional other gradients (e.g., slice selection gradients or spoiler gradients) in the gradient prepulse. The proposed approach could be also of interest in DW imaging of the brain, where vibration induced artifacts were reported previously.[7] Especially in pediatric cases, vibration effects could be even more severe due to the light weight of the patients and the typical optimization of the scanner hardware toward adult weights and dimensions.[8] The general trend toward high *b*-value brain diffusion that allows high-resolution diffusion tensor imaging with fiber tracking comes with the cost of stronger and longer diffusion gradients.[9] Such more demanding requirements on the gradient scanner hardware are expected to increase the occurrence and strength of vibration artifacts. The proposed VMG is not able to completely recover the lost signal but can reduce the artifact with minor penalty on the acquisition time. Further studies should focus on the application of the proposed technique on other DW measurements to reduce artifacts.

6 | CONCLUSION

A method was proposed to mitigate signal loss in DW measurements induced by scanner table vibrations. The benefit for placing an additional gradient before the DW module in a DW MRS sequence was shown by mechanical modeling and by measuring the actual displacements on the surface of a phantom during a DW MRS measurement. When using the additional gradient, the displacements during the diffusion gradients were more similar, which would result in less signal loss by intravoxel dephasing. The application of the proposed method showed an improvement in lipid ADC quantification in WF phantoms and in the tibia bone marrow of 3 healthy volunteers.

ORCID

Dominik Weidlich [iD] https://orcid.org/0000-0001-7842-2682
Marcus Maeder [iD] https://orcid.org/0000-0001-8541-8630
Stefan Ruschke [iD] https://orcid.org/0000-0001-9658-6541
Dimitrios C. Karampinos [iD] https://orcid.org/0000-0003-4922-3662

REFERENCES

1. Jones DK. *Diffusion MRI: Theory, Methods, and Applications*. New York, NY: Oxford University Press; 2012.

2. Anderson AW, Gore JC. Analysis and correction of motion artifacts in diffusion weighted imaging. *Magn Reson Med*. 1994;32:379–387.

3. Reese TG, Heid O, Weisskoff RM, Wedeen VJ. Reduction of eddy-current-induced distortion in diffusion MRI using a twice-refocused spin echo. *Magn Reson Med*. 2003;49:177–182.

4. Steidle G, Eibofner F, Schick F. Quantitative diffusion imaging of adipose tissue in the human lower leg at 1.5 T. *Magn Reson Med*. 2011;65:1119–1125.

5. Hiltunen J, Hari R, Jousmaki V, Muller K, Sepponen R, Joensuu R. Quantification of mechanical vibration during diffusion tensor imaging at 3 T. *NeuroImage*. 2006;32:93–103.

6. Gallichan D, Robson MD, Bartsch A, Miller KL. TREMR: table-resonance elastography with MR. *Magn Reson Med*. 2009;62:815–821.

7. Gallichan D, Scholz J, Bartsch A, Behrens TE, Robson MD, Miller KL. Addressing a systematic vibration artifact in diffusion-weighted MRI. *Hum Brain Mapp*. 2010;31:193–202.

8. Berl MM, Walker L, Modi P, et al. Investigation of vibration-induced artifact in clinical diffusion-weighted imaging of pediatric subjects. *Hum Brain Mapp*. 2015;36:4745–4757.

9. Setsompop K, Kimmlingen R, Eberlein E, et al. Pushing the limits of in vivo diffusion MRI for the Human Connectome Project. *NeuroImage*. 2013;80:220–233.

10. Cao P, Fan S-J, Wang AM, et al. Diffusion magnetic resonance monitors intramyocellular lipid droplet size in vivo. *Magn Reson Med*. 2015;73:59–69.

11. Verma SK, Nagashima K, Yaligar J, et al. Differentiating brown and white adipose tissues by high-resolution diffusion NMR spectroscopy. *J Lipid Res*. 2017;58:289–298.

12. Weidlich D, Honecker J, Gmach O, et al. Measuring large lipid droplet sizes by probing restricted lipid diffusion effects with diffusion-weighted MRS at 3T. *Magn Reson Med*. 2019;81:3427–3439.

13. Lehnert A, Machann J, Helms G, Claussen CD, Schick F. Diffusion characteristics of large molecules assessed by proton MRS on a whole-body MR system. *Magn Reson Imaging*. 2004;22:39–46.

14. Suzuki M, Shinohara Y, Ohsaki Y, Fujimoto T. Lipid droplets: size matters. *J Electron Microsc (Tokyo)*. 2011;60(suppl 1):S101–S116.

15. Cousin B, Cinti S, Morroni M, et al. Occurrence of brown adipocytes in rat white adipose tissue: molecular and morphological characterization. *J Cell Sci*. 1992;103:931–942.

16. Scheller EL, Doucette CR, Learman BS, et al. Region-specific variation in the properties of skeletal adipocytes reveals regulated and constitutive marrow adipose tissues. *Nat Commun*. 2015;6:7808.

17. Callaghan PT. *Principles of Nuclear Magnetic Resonance Microscopy*. Oxford University Press on Demand; 1993.

18. Hurwitz R, Lane SR, Bell RA, Brant-Zawadzki MN. Acoustic analysis of gradient-coil noise in MR imaging. *Radiology*. 1989;173:545–548.

19. Stejskal EO, Tanner JE. Spin diffusion measurements: spin echoes in the presence of a time-dependent field gradient. *J Chem Phys*. 1965;42:288–292.

20. Low G, Kruse SA, Lomas DJ. General review of magnetic resonance elastography. *World J Radiol*. 2016;8:59–72.

21. Gao L, Parker KJ, Lerner RM, Levinson SF. Imaging of the elastic properties of tissue—a review. *Ultrasound Med Biol*. 1996;22:959–977.

22. Vöth S. *Dynamik schwingungsfähiger Systeme: Von Der Modellbildung bis zur Betriebsfestigkeitsrechnung mit MATLAB/SIMULINK*. Wiesbaden, Germany: Vieweg+Teubner Verlag; 2007.

23. Ruschke S, Kienberger H, Baum T, et al. Diffusion-weighted stimulated echo acquisition mode (DW-STEAM) MR spectroscopy to measure fat unsaturation in regions with low proton-density fat fraction. *Magn Reson Med*. 2016;75:32–41.

24. Schmitter S, Diesch E, Amann M, Kroll A, Moayer M, Schad LR. Silent echo-planar imaging for auditory FMRI. *MAGMA*. 2008;21:317–325.

SUPPORTING INFORMATION

Additional supporting information may be found online in the Supporting Information section.
Equations of motion for 2 mass-spring-damper system

6.3 Journal Publication III: Lipid droplet size mapping in human adipose tissue using a clinical 3T system

The publication entitled *Lipid droplet size mapping in human adipose tissue using a clinical 3T system* was published in Magnetic Resonance in Medicine (ISSN: 0740-3194) [129]. The manuscript was authored by Dominik Weidlich, Julius Honecker, Christof Boehm, Stefan Ruschke, Daniela Junker, Anh T. Van, Marcus R. Makowski, Christina Holzapfel, Melina Claussnitzer, Hans Hauner and Dimitrios C. Karampinos. It is available online (DOI: 10.1002/mrm.28755) as an open access article under the terms of the Creative Commons Attribution-NonCommercial-NoDerivs License. Preliminary results were presented in the conference contribution C1, which was awarded with an ISMRM Magna Cum Laude Merit Award and selected as an oral presentation at the ISMRM annual meeting 2021. A summary of the publication is provided in Section 6.3.1, the author contributions are listed in Section 6.3.2 and the full text is included subsequently on the following pages.

6.3.1 Abstract

Purpose

To develop a methodology for probing lipid droplet sizes with a clinical system based on a diffusion-weighted (DW) stimulated echo-prepared (STE) turbo spin echo (TSE) sequence and to validate the methodology in water-fat emulsions and ex vivo adipose tissue (AT) samples.

Methods

A DW-STE preparation was combined with a single-shot TSE readout for measurements at different b-values and diffusion times. An analytical expression was used to estimate the droplet size and three fitting approaches were compared: magnitude-based spatial averaging with voxel-wise residual minimization (MbV), complex-based spatial averaging with voxel-wise residual minimization (CbV) and complex-based spatial averaging with neighborhood-regularized residual minimization (CbR). Simulations were performed to characterize the fitting residual landscape and the approaches' noise performance. The applicability was assessed in oil-in-water emulsions in comparison with laser deflection and in ten human white AT samples in comparison with histology.

Results

The fitting residual landscape showed a minimum valley with increasing extent as the droplet size increased. In phantoms, a very good agreement of the mean droplet size was observed between the DW-MRI-based and the laser deflection measurements, showing the best performance with the CbR processing (R^2/p: 0.971/0.014). In the human AT samples, the CbR processing showed a significant correlation (R^2/p: 0.531/0.017) compared to histology.

Conclusion

The proposed methodology was able to probe restricted diffusion effects in lipid droplets and to estimate lipid droplet size using a clinical 3T system. The methodology was validated using phantoms and the feasibility to measure lipid droplet size in white AT was shown ex vivo.

6.3.2 Author contributions

The first author performed the experiments (MR measurements), programmed the magnetic resonance pulse sequence (propriety hardware specific libraries and software from Philips Medical Systems (Best, The Netherlands)), implemented the post-processing and the quantification process. With the help and consultation form the coauthors, the first author designed the experiment, manufactured the oil-in-water-emulsion phantoms, established the cooperation with several surgery departments to obtain the adipose tissue samples, analyzed and interpreted the data and wrote the manuscript.

FULL PAPER

Lipid droplet–size mapping in human adipose tissue using a clinical 3T system

Dominik Weidlich[1] 🆔 | **Julius Honecker**[2] 🆔 | **Christof Boehm**[1] 🆔 | **Stefan Ruschke**[1] 🆔 | **Daniela Junker**[1] | **Anh T. Van**[1] | **Marcus R. Makowski**[1] | **Christina Holzapfel**[3] | **Melina Claussnitzer**[4,5,6] 🆔 | **Hans Hauner**[2,3] 🆔 | **Dimitrios C. Karampinos**[1] 🆔

[1]Department of Diagnostic and Interventional Radiology, School of Medicine, Technical University of Munich, Munich, Germany

[2]Else Kröner Fresenius Center for Nutritional Medicine, School of Life Sciences, Technical University of Munich, Munich, Germany

[3]Institute for Nutritional Medicine, School of Medicine, Technical University of Munich, Munich, Germany

[4]Broad Institute of MIT and Harvard, Cambridge, Massachusetts, USA

[5]Division of Gerontology, Department of Medicine, Beth Israel Deaconess Medical Center, Boston, Massachusetts, USA

[6]Harvard Medical School, Harvard University, Boston, Massachusetts, USA

Correspondence
Dominik Weidlich, Department of Diagnostic and Interventional Radiology, School of Medicine, Technical University of Munich, Ismaninger Str. 22, 81675 Munich, Germany.
Email: dominik.weidlich@tum.de

Purpose: To develop a methodology for probing lipid droplet sizes with a clinical system based on a diffusion-weighted stimulated echo–prepared turbo spin-echo sequence and to validate the methodology in water–fat emulsions and show its applicability in ex vivo adipose-tissue samples.

Methods: A diffusion-weighted stimulated echo–prepared preparation was combined with a single-shot turbo spin-echo readout for measurements at different b-values and diffusion times. The droplet size was estimated with an analytical expression, and three fitting approaches were compared: magnitude-based spatial averaging with voxel-wise residual minimization, complex-based spatial averaging with voxel-wise residual minimization, and complex-based spatial averaging with neighborhood-regularized residual minimization. Simulations were performed to characterize the fitting residual landscape and the approaches' noise performance. The applicability was assessed in oil-in-water emulsions in comparison with laser deflection and in ten human white adipose tissue samples in comparison with histology.

Results: The fitting residual landscape showed a minimum valley with increasing extent as the droplet size increased. In phantoms, a very good agreement of the mean droplet size was observed between the diffusion-weighted MRI-based and the laser deflection measurements, showing the best performance with complex-based spatial averaging with neighborhood-regularized residual minimization processing (R^2/P: 0.971/0.014). In the human adipose-tissue samples, complex-based spatial averaging with neighborhood-regularized residual minimization processing showed a significant correlation (R^2/P: 0.531/0.017) compared with histology.

Conclusion: The proposed acquisition and parameter-estimation methodology was able to probe restricted diffusion effects in lipid droplets. The methodology was validated using phantoms, and its feasibility in measuring an apparent lipid droplet size was demonstrated ex vivo in white adipose tissue.

KEYWORDS

adipocyte diameter, adipose tissue microstructure, DW-TSE, fat diffusion, lipid droplet

1 | INTRODUCTION

The assessment of lipid droplet size is important to study adipose-tissue (AT) remodeling in both health and metabolic dysfunction. In white AT (WAT), adipocytes contain unilocular lipid droplets with a diameter between 50 μm and 150 μm and a thin surrounding cytoplasm. Thereby, the lipid droplet size is typically considered synonymous for the adipocyte size. With the onset of obesity, an increase in adipocyte size in subcutaneous and visceral WAT can be observed in adults.[1,2] WAT adipocyte size is known to be associated with comorbidities of obesity such as type 2 diabetes, dyslipidemia, and cardiometabolic risk.[3] Therefore, adipocyte size assessment is highly desirable to identify the patient's risk to develop obesity-related medical conditions. Currently, however, the measurement of adipocyte size requires invasive biopsy procedures.[4]

Diffusion-weighted (DW) MR is a powerful approach for the noninvasive probing of tissue microstructure. The reduction of the ADC with increasing diffusion times due to diffusion-restriction effects has been applied extensively to estimate cell size in water-containing tissues.[5] Measuring lipid-diffusion properties remains challenging, as fat has a diffusion coefficient approximately two orders of magnitude lower than water.[6,7] The low fat diffusivity imposes the requirement for high b-values and long diffusion times to measure diffusion-restriction effects, inducing further technical challenges related to eddy currents[8] and increased motion sensitivity.[9,10] However, even when using high b-values and long diffusion times, the extraction of lipid droplet size from DW measurements requires high SNR,[11] especially due to small diffusion-restriction effects when probing large lipid droplet sizes in human WAT.

Diffusion-weighted MRS (DW-MRS) is a versatile tool that allows to measure diffusion properties of metabolites other than water[12,13] and has recently been applied to study lipid diffusion. Specifically, high b-value single-voxel DW-MRS techniques have been applied to study myocellular lipid diffusion,[14] to quantify the intramyocellular lipid droplet size[15] and to study murine brown adipocytes.[16] However, most of the existing lipid DW-MRS work has been performed ex vivo, investigating small lipid droplets (below 10 μm) using the gradient hardware of preclinical systems. Only recently, the feasibility of using DW-MRS was reported for the in vivo probing of lipid droplet size in human bone marrow adipocytes on a clinical system, which represents a milestone toward probing the lipid droplet size in larger WAT adipocytes.[11]

Single-voxel DW-MRS allows high SNR but is associated with important limitations when aiming at clinical translation of the lipid droplet size measurement: Due to the large voxel size, DW-MRS is sensitive to motion-induced intra-voxel dephasing effects, which results in quantification errors. Acquiring data with smaller voxel size would mitigate this effect and is an important step toward in vivo applicability. Neighborhood information could also lead to a more robust lipid droplet size fitting, but with single-voxel MRS no neighborhood information is encoded. Acquiring spatially resolved data would allow regularized parameter fitting in the lipid droplet size estimation.

Therefore, a lipid DWI technique is desirable, which allows the acquisition of lipid signals at high b-values and long diffusion times to at least partly overcome the aforementioned limitations of lipid single-voxel DW-MRS. Lipid DWI will not only be less sensitive to motion/vibration effects and has the possibility to consider the voxel neighborhood in the fitting process, but potentially also allows the extraction of spatially resolved lipid droplet size maps. Previous work aiming at lipid DWI have been based on DW spin-echo single-shot EPI.[7] However, spin echo–based DW suffers from lower SNR when using long diffusion times, whereas EPI readouts are highly sensitive to off-resonance effects (including different chemical shift artifacts for the different fat peaks).[17] Instead, a stimulated echo–based (STE) preparation may allow to probe diffusion restriction effects at long diffusion times, and a single-shot turbo spin-echo (TSE) readout could reduce the sensitivity to chemical shift artifacts.[18]

Therefore, the purpose of the present work was to (1) develop a DW-STE-prepared single-shot TSE sequence for measuring lipid diffusion using a clinical 3T system, (2) develop the processing for lipid droplet size mapping, (3) validate the methodology in water–fat emulsions by comparing the MR results with laser deflection measurements (methodology to measure lipid particle-size distributions[19]) and (4) to investigate the methodology in ex vivo human AT samples by comparing the MR results with histology.

2 | METHODS

2.1 | Pulse sequence

A nonselective 3D DW-STE preparation consisting of four 90° Malcom-Levitt RF pulses[20] and monopolar diffusion gradients combined with a single-shot 2D TSE readout (Figure 1) was developed. To eliminate eddy current–induced and motion-induced phase errors, magnitude-stabilizing gradients following Alsop's method[18] were introduced in preparation and readout.[21] The b-value was adjusted by changing the diffusion gradient strength. The diffusion time was changed by varying the mixing time (TM) of the preparation module. The DW-STE preparation was designed to allow the strong DW necessary to investigate lipid diffusion, while offering the possibility to increase the diffusion time with minor signal attenuation. The influence of residual water signal was reduced by only acquiring DW signals at b-values above 5000 mm²/s and by a frequency selectivity of the preparation module that additionally attenuates the water signal. The preparation module has a bandwidth of approximately ±400 Hz, and the Malcom-Levitt RF pulses were used to ensure a decent robustness against B_1 inhomogeneities with moderate specific absorption rate penalty (Supporting Information Figure S1). The center frequency was set manually to the main fat peak in all subsequent experiments. The maximum b-value and diffusion time were empirically selected to be as large as possible, while simultaneously ensuring a sufficient SNR in the measurement protocols listed subsequently.

2.2 | Reconstruction and preprocessing of DW images

The obtained k-space data were low-pass-filtered using a Hanning window filter. Different sizes of the filter were empirically tested and the results were inspected visually. A filter size of half of the k-space window was selected and used for the subsequent processing because it provided a robust estimation of the low-resolution phase term. The low-resolution phase term was extracted and subsequently subtracted from the corresponding full-resolution DW image.[22] Afterward, the effective SNR ($SNR_{effective}$) was increased by spatially averaging the DW image under the assumption that the tissue heterogeneity is small. Spatial averaging was performed by taking the signal's mean within a square with a certain voxels edge length. The value of $SNR_{effective}$ was equal to sqrt(N)*SNR_0, where N is equal to the number of voxels that are averaged and SNR_0 is the SNR of a single voxel. The 2D spatial averaging was either performed on the magnitude or the complex DW images separately for each diffusion time, b-value, and average.

2.3 | Lipid droplet size estimation

The lipid droplet size can be estimated based on DW signals, previously measured by DW-MRS[11] with the corresponding cost function C:

$$C = \left\| S_0 \, \text{c.} \, S_{Murday\&Cotts}(d,D) \, \text{c.} \exp\left(-\frac{TM}{T1}\right) - S_{exp} \right\|^2 \quad (1)$$

where S_0 is the signal without DW; $S_{Murday\&Cotts}$ is the theoretical DW signal,[23] d is the restricting spherical barrier diameter, D is the free diffusion constant, TM is the DW-STE preparation's mixing time, T_1 is the longitudinal relaxation constant, and S_{exp} is the measured signal.

The obtained DW images can be used to fit the lipid droplet size spatially resolved by minimizing the cost function C voxel-wise. Fitting was performed using a nonnegative least-squares fitting using the trust-region-reflective algorithm by *MATLAB*
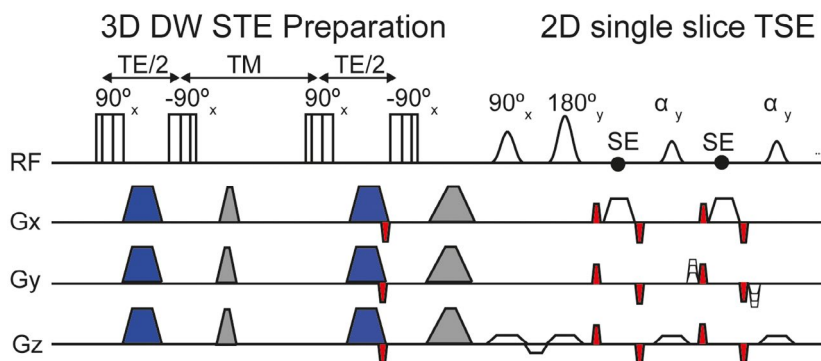

FIGURE 1 Sequence diagram of the proposed diffusion-weighted (DW) stimulated echo–based (STE)-prepared single-shot 2D turbo spin echo (TSE). The DW-STE magnetization preparation consists of four composite 90° Malcom-Levitt RF pulses and monopolar diffusion-sensitizing gradients (blue). To eliminate eddy current–induced and motion-induced phase errors, an additional pair of dephasing/rephasing gradients (indicated in red), denoted as magnitude stabilizers, are introduced before the last tip-up pulse. Additional, magnitude stabilizers are performed immediately before and after every spin-echo formation (also indicated in red). The spoiler gradients within the magnetization preparation are indicated in gray. Abbreviations: SE, spin echo; TE, echo time; TM, mixing time

(MathWorks, Natick, MA). To avoid local minima at each voxel, the fitting was performed with multiple initial starting value pairs (i) for d and D. The residual $res_i(r)$ and the estimated parameters $d_i(r)$, $D_i(r)$, $T1_i(r)$, $S_{0,i}(r)$ were recorded for each initial starting value pair i and voxel location r. The initial starting values were selected to be close to the expected parameter values but also covering a large range. Therefore, the initial starting values for phantom fitting were $d = 4\text{-}28$ µm in 4-µm steps, $D = 6 \times 10^{-6}$ mm²/s to 10×10^{-6} mm²/s in 0.5×10^{-6}-mm²/s steps, and $T_1 = 300$ ms. The value of S_0 was estimated based on the other initial starting values and the maximum value of the noisy signal. For the AT samples case, the initial starting values for the fitting were $d = 20\text{-}80$ µm in 10-µm steps, $D = 6 \times 10^{-6}$ mm²/s to 10×10^{-6} mm²/s in 0.5×10^{-6}-mm²/s steps, and T_1 and S_0 were the same as in the phantom case.

The final parameters were estimated by finding either a voxel-wise minimum or a neighborhood-regularized global minimum. Figure 2 shows an overview of the processing pipeline. Combined with the possibility of performing a magnitude-based (resulting in the residuals $res_{Mbi}[r]$) or complex-based (resulting in the residuals $res_{Cbi}[r]$) averaging before the parameter estimation, different processing schemes can be distinguished.

Specifically, three different ways of processing were compared: magnitude-based spatial averaging with voxel-wise residual minimization (MbV, red color in figures), complex-based spatial averaging with voxel-wise residual minimization (CbV, blue color in figures), and complex-based spatial averaging with neighborhood-regularized residual minimization (CbR, green color in figures). In Figure 2, only the
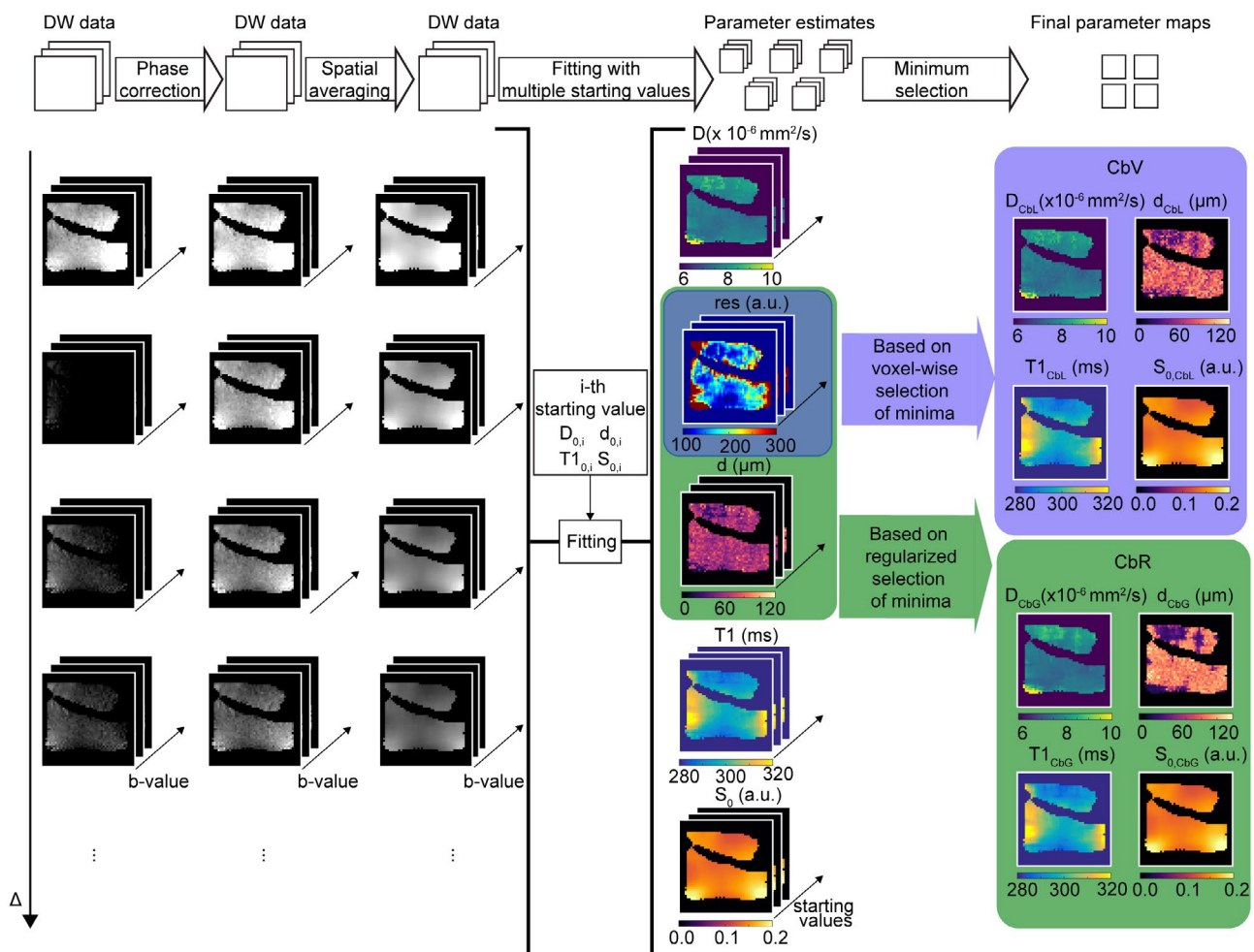

FIGURE 2 Overview of fitting process is shown in one adipose-tissue (AT) sample. Data are acquired with different diffusion times (Δ, rows) and diffusion weightings (b-value, diagonal dimension). First, the complex data are phase-corrected and then spatially averaged to increase SNR. All data are pooled, and a voxel-wise fitting is performed with different initial starting values. The fitting process leads to different estimates for the parameter maps. The final parameter maps can be obtained from the estimates in two different ways. Taking the voxel-wise estimate with lowest residual leads to the magnitude-based spatial averaging with voxel-wise residual minimization (MbV) processing (not shown) when using magnitude data or CbV processing (blue) using complex data. Using the complex data and additionally imposing a spatially slowly varying lipid droplet size (represented by its diameter) leads to the CbR processing (green). Abbreviations: CbR, complex-based spatial averaging with neighborhood-regularized residual minimization; CbV, complex-based spatial averaging with voxel-wise residual minimization

CbV and the CbR processing are shown because the MbV processing is identical to CbV besides the performed spatial averaging.

2.3.1 | Magnitude-based spatial averaging with voxel-wise residual minimization

Spatial averaging was first performed on the magnitude DW images. Fitting was then performed voxel-wise for multiple initial starting values, and an analysis of the residuals was performed at each voxel location r as follows:

$$\left[d_{MbV}(r), D_{MbV}(r), T1_{MbV}(r), S_{0,MbV}(r)\right] = arg \min_{d(r),D(r),T1(r),S_0(r)} res_{Mb}(r) \quad (2)$$

2.3.2 | Complex-based spatial averaging with voxel-wise residual minimization

Spatial averaging was first performed on the complex DW images. Fitting was then performed voxel-wise for multiple initial starting values, and an analysis of the residuals was performed at each spatial location r as follows:

$$\left[d_{CbV}(r), D_{CbV}(r), T1_{CbV}(r), S_{0,CbV}(r)\right] = arg \min_{d(r),D(r),T1(r),S_0(r)} res_{Cb}(r) \quad (3)$$

2.3.3 | Complex-based spatial averaging with neighborhood-regularized residual minimization

Spatial averaging was first performed on the complex DW images, and the fitting was performed voxel-wise with different initial starting values. A global analysis was then performed, imposing a small spatial lipid droplet–size variation. Therefore, the fitted parameters in each voxel were selected not only based on the local voxel residual but also by penalizing large diameter variations in the Von Neumann neighborhood (representing the four adjacent voxels) of the voxel ($N[r]$). A regularized global cost function similar to Cui et al[24] and Boehm et al[25] was used, in which $res_{Cb}(r)$ replaced the data-consistency term, and the regularization term was the estimated diameter's variation in the voxel's neighborhood. The minimization problem was solved with a graph-cut algorithm using a graph construction with convex priors that allows for unequally sampled space[26] in the diameter dimension:

$$\begin{aligned}&\left[d_{CbR}(r), D_{CbR}(r), T1_{CbR}(r), S_{0,CbR}(r)\right]\\&= arg \min_{d(r),D(r),T1(r),S_0(r)} \sum_r res_{Cb}(r) + \lambda\, c. \sum_{s\in N(r)} \|d(r)-d(s)\|\end{aligned}$$
$$(4)$$

The regularization parameter λ was chosen following the discrepancy principle and was set to 0.1. The discrepancy principle states that the regularization term should be similar to the noise floor.[27] The used regularization term was approximately 10% of the data consistency term.

2.4 | Phantom manufacturing

Four high-fat water–fat phantoms (oil-in-water emulsions) resembling in vivo AT lipid content were produced. Each phantom contained 800 mL sunflower oil (ARO), 200 mL water, 20 mL Tween 80 (Sigma-Aldrich, Taufkirchen, Germany), and 1 g of sodium benzoate (Roth, Karlsruhe, Germany). Emulsification was carried out with a colloid mill (IKA Labor-Pilot 2000/4; IKA-Werke, Staufen, Germany) at 5000/6000/9000/12 000 revolutions per minute to obtain different oil droplet sizes (standardized emulsification process[28]). The particle size was measured by dynamic light scattering using a particle-sizing instrument (Mastersizer 2000; Malvern Instruments, Worcestershire, United Kingdom). Samples were diluted with 0.5% sodium dodecyl sulfate (Serva; Heidelberg, Germany) solution (1:10, vol/vol) to separate agglomerates and measure single lipid droplets.[19] From the particle-size distributions, mean diameters were extracted.

2.5 | Adipose tissue sampling

Ten abdominal subcutaneous AT samples were obtained from patients undergoing abdominoplasty after severe weight loss. The study was approved by the local ethics commission, and written consent was obtained. Small pieces from the AT samples were fixed in formalin for histological processing. After slicing and staining with hematoxylin and eosin, images were taken in high-definition range at ×200 magnification (VHX-6000l Keyence, Osaka, Japan). Adipocyte area determination was carried out using the proprietary microscope image analysis software (VHX-6000; Keyence) by automatically identifying round objects within the histology slice and obtaining the object's area. A lower (200 μm^2) and upper size limit (16 000 μm^2) were used to remove objects typically representing artifacts, cell debris, or ruptured adipocytes. Each image was manually inspected after automated identification. Adipocyte diameter was calculated assuming a spherical shape.[4]

2.6 | Numerical analysis of fitting residual landscape

To investigate the residual landscape of the fitting, the difference of the signal decay curves relative to selected reference

signals was calculated based on the cost function C ($T_1 = 300$ ms and $S_0 = 100$ were assumed while varying the free diffusion constant and diameter). The following measurement scenarios were distinguished due to different scan protocols.

In the phantom case, the protocol included 50 pairs of b-value and TM, with b-values of 5000 to 50 000 s/mm^2 in 5000-s/mm^2 steps and TM of 200-400 ms in 50-ms steps. The reference signals were simulated for droplet diameters of 4 μm and 12 μm and for a free diffusion constant of 8×10^{-6} mm^2/s. The difference relative to these two reference signals was calculated for a range of combinations of droplet diameter (2-30 μm) and free diffusion constant ($[7.5-8.5] \times 10^{-6}$ mm^2/s).

In the AT sample case, the protocol included 110 pairs of b-value and TM, with b-values of 5000 to 50 000 s/mm^2 in 5000-s/mm^2 steps and TM of 200-700 ms in 50-ms steps. The reference signals were simulated for droplet diameters of 50 μm and 60 μm and for a free diffusion constant of 8×10^{-6} mm^2/s. The difference relative to these two reference signals was calculated for a range of combinations of droplet diameter (20-120 μm) and free diffusion constant ($[7.5-8.5] \times 10^{-6}$ mm^2/s).

2.7 | Noise performance analysis

To characterize the three processing approaches, a noise simulation was performed using as ground truth the signal from the fitting residual landscape numerical analysis (droplet diameter in phantom case [12 μm] and droplet diameter in AT sample [60 μm]). Gaussian noise was added to the real and imaginary part of the complex signal to achieve a SNR_0 (defined for the first b-value and diffusion time). The value of SNR_0 was selected as the approximate lower SNR limit from the subsequent experimental scans. Spatial averaging was simulated by averaging the magnitude or complex data within a square window of 1-11 voxels edge length. Therefore, noise was first added over groups of $1^2/2^2/3^2/4^2/5^2/6^2/7^2/8^2/9^2/10^2/11^2$ voxels, and the signals were averaged in a second step that led to variable $SNR_{effective}$. At each size of the averaging window, the spatially averaged signal was then used to perform the fitting with multiple starting values. The noisy signal generation and averaging was repeated 1089 (corresponding to a 33 × 33 voxel 2D slice) times, resulting in 1089 noisy samples at each SNR level (depending on the size of the averaging window), and statistics were extracted for the MbV and CbV processing.

To evaluate the performance of the regularized fitting, the 1089 noise samples at each SNR level were rearranged to form a 2D slice that was processed with the CbR processing. In the phantom case, SNR_0 was assumed to be 75, and in the AT sample case, SNR_0 was assumed to be 50.

2.8 | Phantom measurements and analysis

Magnetic resonance scanning of the emulsion phantoms and coconut oil was performed on a 3T system (Ingenia Elition; Philips, Best, Netherlands) using an eight-channel wrist coil with the following parameters: FOV = 90 × 90 mm^2, acquisition voxel size = 1.4 × 2.5 × 10 mm^3, reconstruction voxel size = 1.4 × 1.4 × 10 mm^3, TSE factor = 36, TR/TE/TE$_{Prep}$ = 2000/23/61 ms, five averages, 50 pairs of b-value and TM with b-values = 5000 to 50 000 s/mm^2 in 5000-s/mm^2 steps and TM = 200/250/300/350/400 ms, scan time = 8:30 minutes. To minimize vibration artifacts induced by the strong diffusion gradients, a wooden support table was used.[10]

Neighboring voxels (3 × 3) were averaged to increase $SNR_{effective}$, leading to an effective voxel size of 4.2 × 4.2 × 10 mm^3. The lipid droplet–size fitting was performed with the initial starting values described in the noise simulations. Each average was treated as a separate b-value/TM measurement pair. The SNR was calculated as the ratio between the mean and the SD of the magnitude images across acquired averages for the first diffusion time and b-value.

2.9 | Ex vivo AT sample measurements and analysis

The approximately 10 × 10 × 5 cm^3 AT samples fixed in formalin were scanned using an eight-channel extremity coil with the following parameters: FOV = 120 × 120 mm^2, acquisition and reconstruction voxel size = 1.9 × 1.9 × 8 mm^3, TSE factor = 64, TR/TE/TE$_{Prep}$ = 2000/18.5/62 ms, four averages, 110 pairs of TM and b-value with b-values = 5000 to 50,000 s/mm^2 in 5000-s/mm^2 steps and TM = 200-700 ms in 50-ms steps, and scan time = 14:56 minutes. To minimize vibration artifacts, a wooden support table was used[10] and the ramps of the diffusion gradient were reduced. Additionally, a proton density fat fraction map was acquired with a 3D multi-echo gradient-echo sequence using bipolar gradient readout with FOV = 100 × 100 × 65 mm^3, voxel size = 1.3 × 1.3 × 1.3 mm^3, TR/TE1/ΔTE = 15/1.4/1.1 ms, flip angle = 5°, and six acquired echoes. The vendor's fat quantification routine included a phase error correction and a complex-based water–fat decomposition using a precalibrated fat spectrum with a single T_2^* correction.[29]

A neighborhood of 6 × 6 voxels was averaged to increase SNR, resulting in an effective voxel size of 11.4 × 11.4 × 8 mm^3. Each average was treated as a separate b-value/TM measurement pair. Voxel-wise SNR was calculated as the ratio between the mean magnitude signal at the first diffusion time and b-value and the SD of an additional noise scan acquired without RF and gradient power.

Given that the influence of certain tissue properties (like particle-size distribution) on the measurement of the MRI-based mean lipid droplet size is still unknown in the ex vivo AT samples, the term "apparent lipid droplet size" was used in the context of the AT study.

3 | RESULTS

3.1 | Numerical analysis of fitting residual landscape

Figure 3 shows the signal fitting landscape for both measurement scenarios with their respective reference droplet diameters. For the diameter of 4 μm in the phantom case, a distinct global minimum in the diameter dimension at the reference droplet diameter was observed with different free diffusion constants yielding very similar signal decay curves. With increasing diameter, the minimum residual valley got broader and more curved. Diameters smaller than the reference diameter with a free diffusion constant larger than the reference as well as diameters larger than the reference diameter with free diffusion constants smaller than the reference can have similar DW signal curves. Within the observed minimum residual valley, the differences between the signal decay curves were small, indicating a small gradient of the fitting's cost function. In the AT case, the minimum residual valley got distinctively broader, and the range of diameter and free diffusion constant combinations resulting in small residuals increased.

3.2 | Noise performance analysis

Figure 4 shows the results from the noise analysis for the phantom case. The 2D histograms of the estimated diffusion constant and droplet diameter yielded a similarly shaped minimum valley, as in Figure 3. The broadness of the diameter and free diffusion constant distribution was reduced at higher $SNR_{effective}$. A noticeable bias of the mean diameter was only observed for the initial SNR_0 (without averaging) for MbV (22.2% overestimation), CbV (22.2% overestimation), and CbR (17.1% overestimation). With increasing $SNR_{effective}$, the mean diameter and free diffusion constant approached the true value, and the associated SDs were decreasing. For CbR, the estimated parameters followed the same trend, but the SD at low $SNR_{effective}$ was reduced compared with MbV and CbV.

In general, the noise analysis for the AT sample case (Figure 5) was comparable to the phantom case, but a higher variability in the estimated parameters and differences between the proposed methods were visible. The 2D histogram showed a broad distribution for the droplet diameter and free diffusion constant estimates for all processing approaches. When the $SNR_{effective}$ was low, even two distinct peaks in the diameter estimation were visible in the MbV and CbV case. With increasing $SNR_{effective}$, these two peaks tended to merge into one. The SD in the diameter estimation appeared similar with voxel-wise estimations (MbV and CbV), whereas it was reduced with CbR. At high $SNR_{effective}$, quantification biases were still observed. At an $SNR_{effective}$ of 500, the deviation from the true value was −10.6 % (MbV), 3.9% (CbV), and 1.7% (CbR).

3.3 | Phantom experimental results

Supporting Information Figure S2 shows the DW signal decay for each phantom. The mono-exponential diffusion signal decay curve at each diffusion time was visible for the water–fat emulsion phantoms as well as coconut oil. The measured ADC of the coconut oil was not dependent on the diffusion time indicating free diffusion.
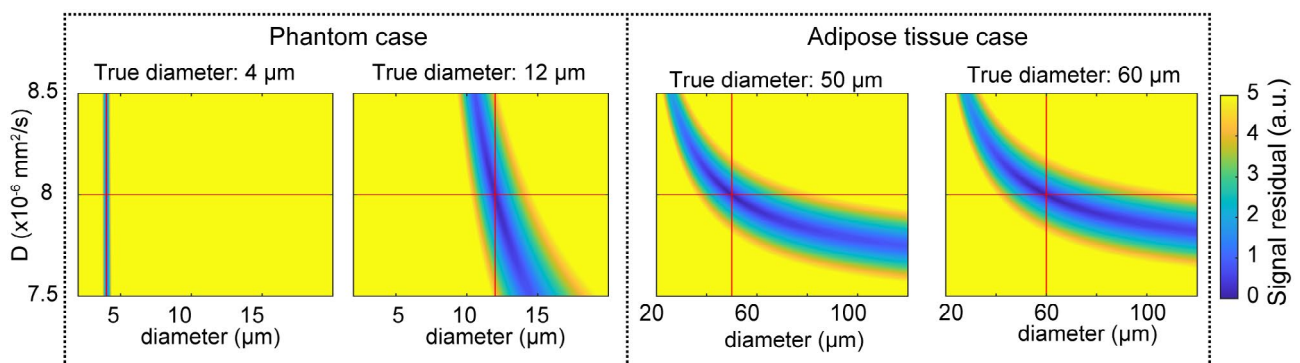

FIGURE 3 Simulated parameter landscape of the fitting process. The differences in the signal decay curves relative to their respective selected signal (reference signal indicated with red cross) were calculated based on Equation 1. The columns show different selected diameters with the same free diffusion constant. The first two columns represent the phantom case, whereas the third and fourth columns represent the AT sample case. With increasing diameter, the minimum valleys get visually broader, indicating a decreasing gradient of the optimization function. Please note the different ranges on the x-axis (diameter dimension)
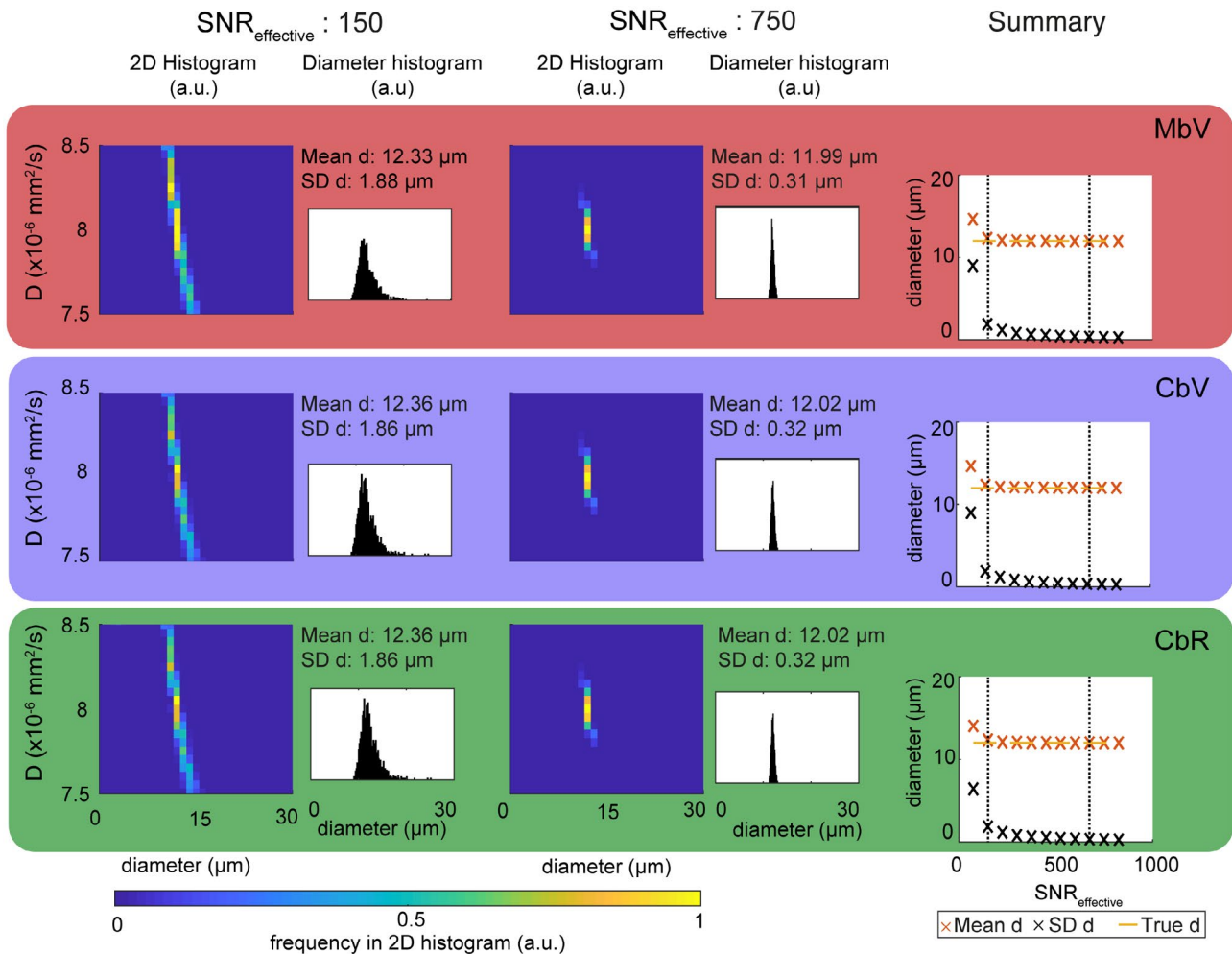
FIGURE 4 Noise performance of the lipid droplet–size estimation in the phantom case (true diameter = 12 μm). The 2D histogram for diameter and diffusion constant estimates as well as a diameter histogram are shown. At low SNR, diffusion constant and diameter estimates closely reassembling the minimum valley shown in Figure 3 can be observed. The MbV and CbV processing yield very similar results. At low SNR, both measurements tend to overestimate the true diameter with an increasing SD. With increasing effective SNR, the mean diameter approaches the true value, and the SD in the estimation decreases. The CbR processing follows the trend of the CbV; however, the SD at different SNR levels is reduced. At an effective SNR (SNR$_{effective}$) of 750, the bias of all methods is below 1%

Figure 6 shows the obtained phantom diameter maps. The two voxel-wise residual minimizations (MbV and CbV) resulted in nearly identical droplet diameter maps with certain regions showing local spatial heterogeneity. A trend toward larger lipid droplet sizes was observed for decreasing stirring frequency. When compared with the voxel-wise fitting, the CbR processing showed reduced spatial heterogeneity in the droplet diameter map. The free diffusion constant maps were similar in all phantoms.

Figure 7 plots the correlation of the MR-based results against the reference measurement laser deflection. The droplet diameter results from the MbV and CbV were very similar; therefore, only the CbV results were shown. In all cases, the DW-MRI results agreed well with the validation measurement ($R^2 > 0.95$ and $P < 5\%$). When the lipid droplet–size fitting was performed with CbV, the linear fit deviated from the identity line (slope/offset = 1.37/−2.52

μm). When CbR was used, the linear fit again approached the identity line (slope/offset = 1.13/−0.71 μm), and the SD of the lipid droplet–size estimation was reduced.

3.4 | Ex vivo AT sample experimental results

Figure 8 depicts the results from two AT samples. AT sample 1 showed smaller adipocyte sizes in histology, higher proton density fat fraction map heterogeneity, and a lower overall SNR (mean SNR of 55 compared with 78 in sample 2 [not shown]). In AT sample 1, smaller apparent lipid droplet sizes were observed with MbV compared with the other methods. The apparent diameter distribution with CbV showed two distinct peaks. With CbR, outliers were reduced in the apparent diameter map, and the height of
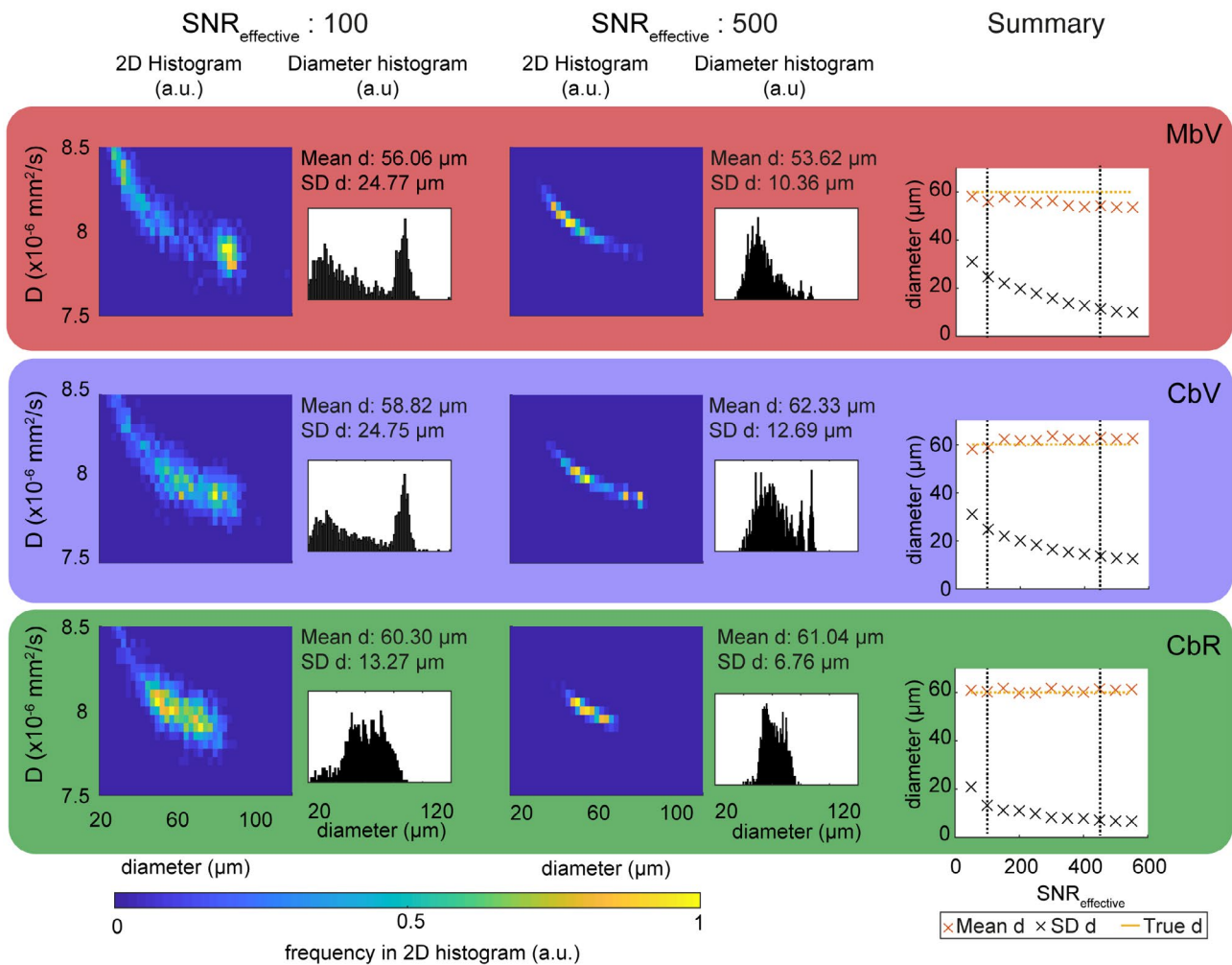
FIGURE 5 Noise performance of the lipid droplet–size estimation in the AT sample case (true diameter = 60 μm). In the 2D histogram, a rather broad distribution for the droplet diameter and free diffusion constant estimates can be observed. The broadness and the SD in the mean diameter estimation decrease with increasing SNR. The distributions of the results obtained by MbV and CbV appear similar, whereas the broadness is reduced with CbR. At high SNR$_{effective}$ (by spatial averaging), quantification biases can be observed. At a SNR$_{effective}$ of 500, the deviation from the true diameter is −10.6% (MbV), 3.9% (CbV), and 1.7% (CbR)

the peak at larger apparent lipid droplets was decreased. In AT sample 2, larger apparent lipid droplet sizes and a better agreement among the three processing methods was observed. The apparent diameter map obtained by MbV showed a relatively large fraction of voxels with small apparent diameter. This fraction decreased when the apparent droplet diameter map was obtained by CbV, and even further when CbR was used. The free diffusion constant maps obtained by CbR showed similar values in both samples. The obtained free diffusion constants for all phantoms and AT samples are listed in the Supporting Information (including a discussion of their agreement with literature values).

Figure 9 summarizes the results from the AT sample study, showing the mean apparent droplet size estimation obtained by the CbR processing in comparison with histology. The depicted SD for the MR-based measurement reflects the broadness of the estimated voxel-wise apparent lipid droplet

size within the acquired 2D slice. The MR-based results and the histology measurements correlated significantly (R^2/P: 0.531/0.017). The CbV processing showed a similar trend as CbR, and the MbV processing resulted in an underestimation of the mean apparent lipid droplet size and no significant correlation with histology (both processing methods not shown in Figure 9).

4 | DISCUSSION

The present study proposes a methodology to noninvasively measure lipid droplet size based on a novel lipid DWI acquisition and lipid droplet–size parameter-estimation approaches. The work shows that it is feasible to measure large lipid droplet size in phantoms and to provide an apparent estimate of lipid droplet sizes in ex vivo human specimens using a clinical 3T system.
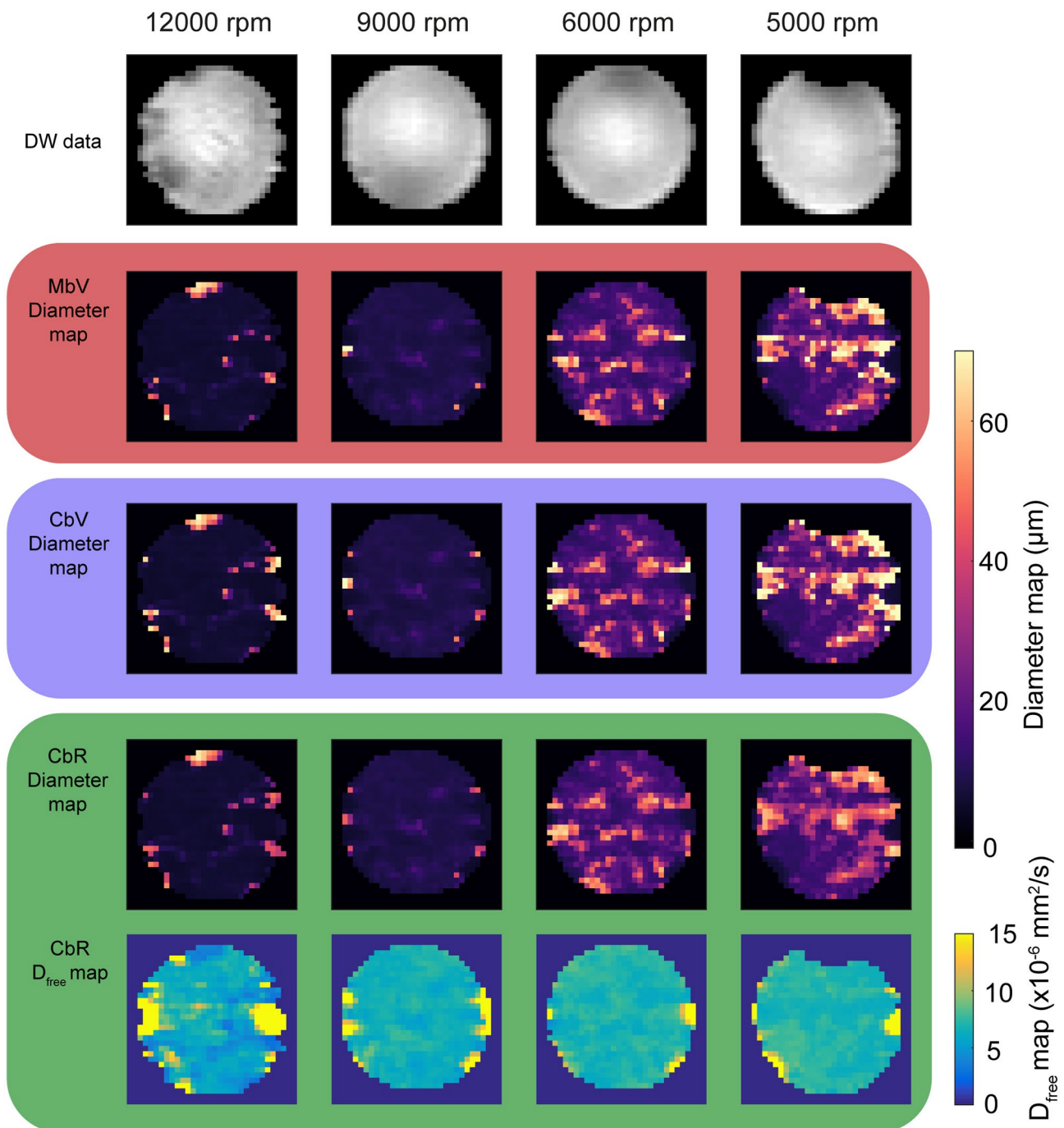
FIGURE 6 Diffusion-weighted imaging data (first row) and corresponding diameter maps for the water–fat emulsion phantoms with the three examined processing approaches. For the CbR processing, the free diffusion constant map is also shown (last row). All processing approaches show an increasing lipid droplet size with decreasing rotation frequency of the colloid mill. Local overestimations of the measured lipid droplet size are visible with the processing approaches with a voxel-vise residual minimization (MbV and CbV), but are reduced with CbR processing. The free diffusion constant is rather similar in all investigated phantoms. Abbreviation: rpm, revolutions per minute

Regarding lipid DWI acquisition, a high b-value DW-STE single-shot TSE acquisition was developed. To measure lipid diffusion in water–fat mixtures, the interference with water signals needs to be reduced. The proposed sequence is tailored to this need, because the used STE preparation has a frequency selectivity with the resonance frequency centered on the main fat peak. In addition, only images with very high b-values ($\geq$ 5,000 s/mm^2) are acquired, which attenuates most of the fast-diffusing water. The proposed preparation module has the disadvantage of measuring only 25% of the available signal. First, 50% of the available signal is lost due to the stimulated echo preparation; and second, an additional 50% of the signal is lost due to the magnitude stabilizing gradients. Despite the inherently low SNR, the developed
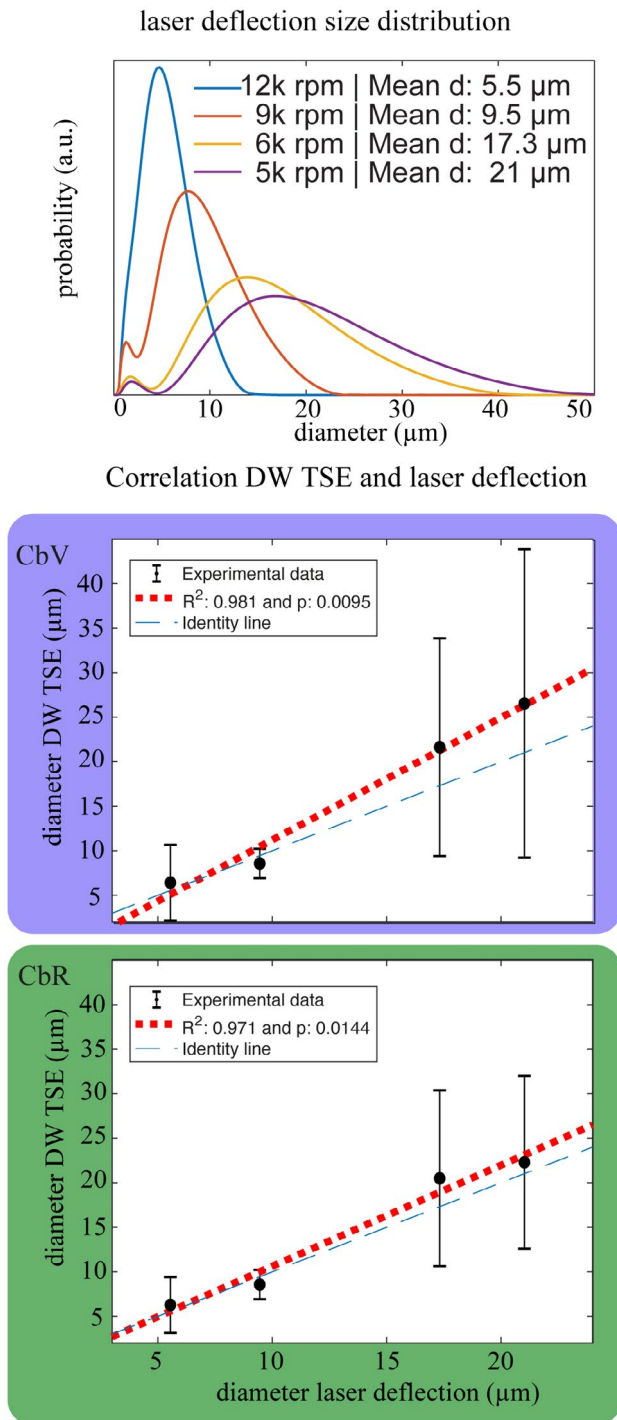
laser deflection size distribution

Correlation DW TSE and laser deflection

FIGURE 7 Correlation analysis of the droplet diameter results obtained with DW MRI compared with the laser-deflection measurement. The laser-deflection measurements revealed an increasing lipid droplet size and distribution broadness with decreasing frequency of the colloid mill. Both presented processing methods (CbV and CbR) correlate significantly with the reference-method laser deflection ($R^2 > 0.95$ and $P < 5\%$). With the CbV processing, the linear fit deviates from the identity line (slope/offset: 1.37/−2.52 µm). With the CbR processing, the linear fit again approaches the identity line (slope/offset: 1.13/−0.71 µm)

technique enables very strong DW with reduced sensitivity to motion-induced phase errors (single-shot TSE design using magnitude stabilizers) and off-resonance effects (TSE design), and allows the acquisition of DW data at varying diffusion times (STE preparation). To sensitize the acquired signal to diffusion restriction effects, longer diffusion times and higher b-values would increase the sensitivity of the measurement to lipid diffusion restriction effects. However, longer diffusion times or higher b-values would increase the required preparation's TE and TM, and are therefore not easily realizable because they would further reduce the measurement SNR.

The present work shows that the lipid droplet–size fitting is challenging, especially for estimating larger diameters. When the DW signal decay curves are compared, different parameter combinations result in very similar decay curves, even without noise (Figure 3). Specifically, small residual variations were observed within a large region around the reference diameter and diffusion coefficient. This might not be critical for smaller diameters, because the lipid droplet diameter can be precisely determined. With increasing size, the curvature and the extent of the region with small residual variation increases, resulting in underestimated and overestimated diameters with very similar DW signal decays.

With added noise, certain parameter combinations within the minimum valley can form local minima. The fitting problem becomes ill-posed and cannot be solved with a standard approach. Using multiple starting values for the fitting process is recommended to find the global, and not only a local, minimum. However, with low SNR, even the approach with multiple starting values can fail, as observed in the noise simulations (Figures 4 and 5). In a 2D histogram of the diameter and corresponding free diffusion constant estimates, similarities to the minimum valleys in Figure 3 can be observed. Because of the small gradient within the minimum valley, a stopping of the fitting within the minimum valley is likely, especially with noisy signals.

When investigating the simulated mean diameter in the phantom case, only deviations from the true value are observed for the minimal SNR with smaller SD with the CbR processing compared with MbV and CbV. With increasing $SNR_{effective}$, all three processing methods approach the true diameter with a small SD. Due to the rather strong restriction effects and high SNR_0 in this phantom scenario, the results from MbV and CbV are similar, whereas the CbR processing shows the same trend but smaller bias and SD. In the simulated AT sample case, much broader droplet diameter and free diffusion-estimate distributions are observed. This can be explained by the small diffusion-restriction effects in the AT samples. The SD in diameter estimation decreases with increasing $SNR_{effective}$. A large underestimation bias is observed, even at high $SNR_{effective}$, with the MbV processing.
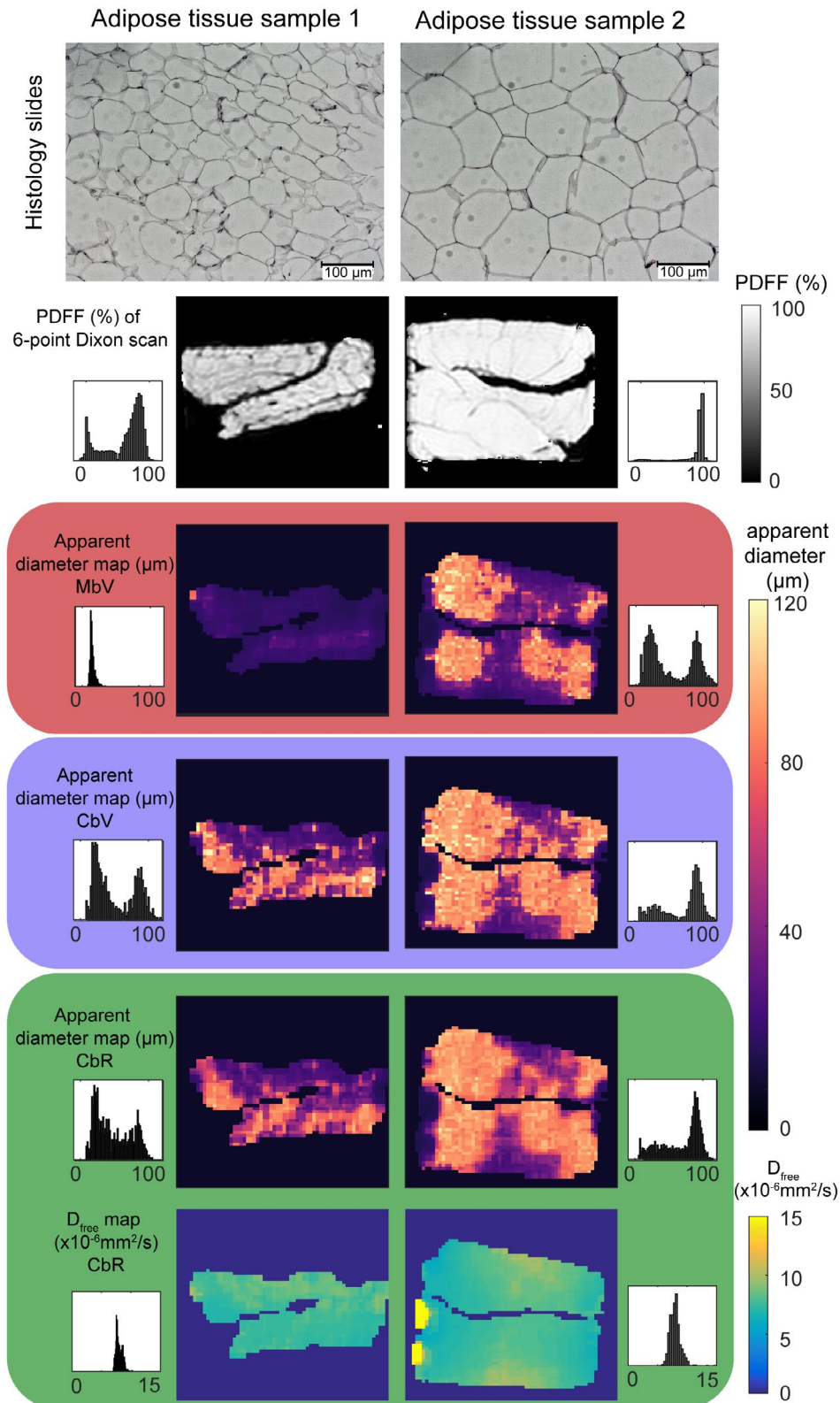
FIGURE 8 Histology slides, proton density fat fraction (PDFF) maps, MbV-based, CbV-based and CbR-based apparent diameter maps, CbR-based free diffusion constant, and corresponding histograms for two AT samples. Adipose-tissue sample 1 shows larger heterogeneity in the PDFF compared with AT sample 2, and a smaller mean adipocyte size in the histology. The apparent diameter map obtained by MbV processing yields very low apparent-diameter estimates in the low-SNR sample compared with the high-SNR sample. When the apparent lipid droplet size is estimated with the CbV processing, larger droplet diameters are extracted in both samples. The SD is decreased with the CbR compared to the CbV processing (broadness in the diameter histograms). The free diffusion constant maps give similar values in both samples
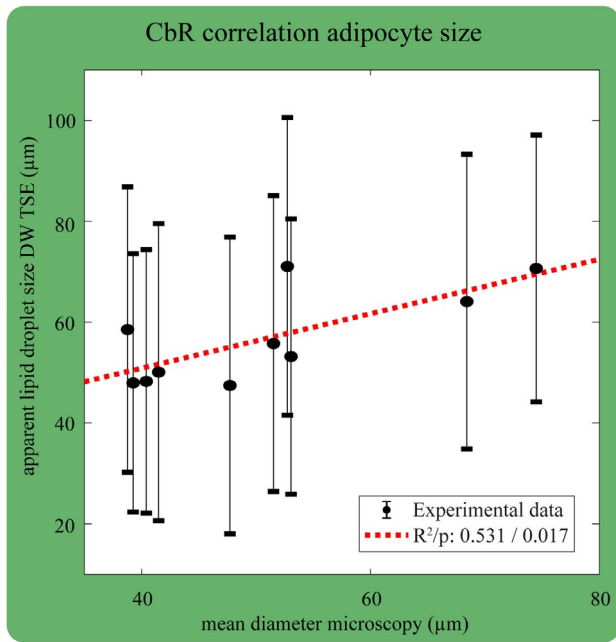
FIGURE 9 Correlation analysis of the mean apparent droplet diameter obtained with CbR processing compared with microscopy in AT sample study. A significant correlation was found when comparing the mean lipid droplet size (R^2/P: 0.531/0.017) obtained by both methods, although a large uncertainty was found in the size estimation of the MR-based method. Mean values ± 1 SD (error bar) are shown

Magnitude averaging can lead to a noise floor, which decreases the measured ADC at longer diffusion times, corresponding to a signal behavior that is characteristic for smaller droplet sizes. With complex averaging, noise bias effects are reduced and the true diameter is only slightly overestimated. The CbR processing not only reduces the SD but also eliminates the bias. The noise simulation reveals that an accurate estimation of large lipid droplet diameters is feasible when the $SNR_{effective}$ is high enough and the data are complex-averaged. The proposed CbR processing yields more accurate and precise results compared with the other two studied fitting approaches.

In the water–fat emulsion phantoms consisting of small lipid droplets, a decreasing ADC curve with increasing diffusion time is observed, which is a clear indicator of diffusion-restriction effects. In coconut oil, no such restriction barriers exist; therefore, the ADC values do not depend on the diffusion time (Supporting Information Figure S2). This analysis can be interpreted as a proof-of-principle experiment, showing the applicability of the presented method to investigate restriction effects of diffusing lipids.

Rather homogenous lipid droplet diameter maps are obtained in phantoms with all processing approaches (Figure 6). The MbV and CbV lead to similar results but show regions with unreasonably large diameters. When the CbR processing is used, the diameter map homogeneity is increased. When comparing the lipid droplet–diameter results from

DW-MRI with laser deflection measurement, a high correlation is found. The diameter maps obtained by CbV included voxel-wise diameter overestimations; therefore, the agreement with laser deflection deviates from the identity line. With the CbV processing, local quantification errors in the droplet-diameter estimates can occur, which can be partly recovered by the proposed CbR processing, leading to a better agreement with the reference method. It can be summarized that the presented methodology provides accurate results in water–fat emulsions (lipid droplet diameter up to 25 μm).

Measuring the apparent droplet size in AT samples ex vivo is challenging because of the small measurable restriction effects due to large droplets and the low lipid diffusivity at room temperature. The two AT samples shown in Figure 8 deviate significantly in their microstructure, as highlighted in the histology images and proton density fat fraction maps. The MbV processing yields too small apparent lipid droplet–size estimates, especially in the low SNR sample. When the CbV processing is used, two distinct apparent diameter peaks are observed in both samples (in agreement with the simulation). When the CbR processing is used, the obtained apparent droplet-diameter map appears smoother and the SD of the apparent diameter estimates is reduced. Within both samples a spatial variation of the apparent diameter map can be observed for all processing approaches. It is unclear whether the observed spatial variation is caused by measurement uncertainties (as indicated in Figure 5) or due to real spatial adipocyte size variations. Given that the used histology provides only a localized estimate of the adipocyte size from the biopsy site, the mean MR-derived apparent droplet diameter (averaged over the acquired 2D slice) was used in the comparison with histology (shown in Figure 9). In the group analysis, a large SD is visible in MRI-based apparent droplet size. Overall, a significant correlation can be observed between the MR-based mean apparent lipid droplet size (with CbR processing) and histology. The results acquired in human AT samples show that it is feasible to estimate an apparent lipid droplet size of ex vivo AT and that a similar trend as histology can observed when examining samples with different mean adipocyte sizes.

An MR-based white adipocyte size estimate could potentially serve as a biomarker for the risk of cardiometabolic diseases and could replace invasive biopsy measurement. Therefore, the proposed technique should be thoroughly validated ex vivo with more AT samples, and the in vivo application should be subsequently targeted. However, additional significant challenges related to motion and prolonged scan times have to be addressed when measuring in vivo.

The described methodology has limitations: First, the measured DW signal is the sum over several fat peaks that have different T_1 relaxation times and potentially different diffusion constants. This is not incorporated in the modeling, which assumes a single component. Because most of the

signal should be associated with the main fat peak, the contribution of these spins should be dominant. Second, the used modeling does not incorporate an underlying cell-size distribution. An asymmetric or multimodal particle-size distribution could induce a bias on the estimated mean adipocyte size, leading eventually to an overestimation or underestimation. Incorporating the estimation of the size distribution in the fitting process can be considered as very challenging because it would require the acquisition of DW data at different diffusion encodings with higher SNR. In addition, a parametrization of the size distribution would need to be known, for which currently no consensus can be found in the literature.[4] However, previous work showed that the broadness of a symmetric particle distribution has minor influence on the mean droplet-size estimation.[11] Third, a partially smooth spatial variation of the lipid droplet size is assumed. Given the fact that subcutaneous fat biopsies are very homogenous and no spatial variation is visible on MR images, the assumption of a slowly varying droplet diameter might be justifiable. Fourth, the balancing term λ is not optimized further, but is instead chosen based on the SNR of the acquired data. Optimizing λ could further reduce quantification errors and should be discussed in further research. Fifth, different existing methods to obtain the adipocyte size from ex vivo AT samples yield different quantitative results.[4] However, this work does not intend to show a quantitative comparison in the AT samples, but rather to demonstrate the feasibility of the developed methodology for large lipid droplet sizes. Sixth, this work is based on a limited sample size in the phantom and the AT study, and includes no optimization of the experimental parameters. Studies using larger sample sizes and further optimizing the experimental parameters are required.

5 | CONCLUSIONS

The present work proposes a methodology to probe diffusion restriction effects in lipid droplets in phantoms and ex vivo AT samples at a 3T clinical scanner using a long diffusion time and high b-value DW-TSE sequence. The challenges in estimating the lipid droplet size from DWI data were evaluated with simulations, and strategies to improve the measurement were proposed. Namely, increasing the SNR by complex spatial averaging, using multiple initial fitting starting values, and applying the additional graph-cut postprocessing steps improved both accuracy and precision in estimating lipid droplet size in phantoms and enabled the estimation of an apparent lipid droplet size in ex vivo AT samples. The presented method showed excellent agreement in measuring lipid droplet size against laser deflection in water–fat phantoms and a correlation when the MR-based mean apparent lipid droplet size was compared with histology in ex vivo human AT samples.

ORCID

Dominik Weidlich https://orcid.org/0000-0001-7842-2682
Julius Honecker https://orcid.org/0000-0002-1592-7023
Christof Boehm https://orcid.org/0000-0003-1321-5804
Stefan Ruschke https://orcid.org/0000-0001-9658-6541
Melina Claussnitzer https://orcid.org/0000-0003-2450-736X
Hans Hauner https://orcid.org/0000-0002-1682-5088
Dimitrios C. Karampinos https://orcid.org/0000-0003-4922-3662

REFERENCES

1. Spalding KL, Arner E, Westermark PO, et al. Dynamics of fat cell turnover in humans. *Nature*. 2008;453:783-787.
2. Salans LB, Cushman SW, Weismann RE. Studies of human adipose tissue. Adipose cell size and number in nonobese and obese patients. *J Clin Invest*. 1973;52:929-941.
3. Laforest S, Labrecque J, Michaud A, Cianflone K, Tchernof A. Adipocyte size as a determinant of metabolic disease and adipose tissue dysfunction. *Crit Rev Clin Lab Sci*. 2015;52:301-313.
4. Laforest S, Michaud A, Paris G, et al. Comparative analysis of three human adipocyte size measurement methods and their relevance for cardiometabolic risk. *Obesity*. 2017;25:122-131.
5. Assaf Y, Blumenfeld-Katzir T, Yovel Y, Basser PJ. AxCaliber: a method for measuring axon diameter distribution from diffusion MRI. *Magn Reson Med*. 2008;59:1347-1354.
6. Lehnert A, Machann J, Helms G, Claussen CD, Schick F. Diffusion characteristics of large molecules assessed by proton MRS on a whole-body MR system. *Magn Reson Imaging*. 2004;22:39-46.
7. Steidle G, Eibofner F, Schick F. Quantitative diffusion imaging of adipose tissue in the human lower leg at 1.5 T. *Magn Reson Med*. 2011;65:1119-1125.
8. Jezzard P, Barnett AS, Pierpaoli C. Characterization of and correction for eddy current artifacts in echo planar diffusion imaging. *Magn Reson Med*. 1998;39:801-812.
9. Anderson AW, Gore JC. Analysis and correction of motion artifacts in diffusion weighted imaging. *Magn Reson Med*. 1994;32:379-387.
10. Weidlich D, Zamskiy M, Maeder M, Ruschke S, Marburg S, Karampinos DC. Reduction of vibration-induced signal loss by

matching mechanical vibrational states: application in high b-value diffusion-weighted MRS. *Magn Reson Med*. 2020;84:39-51.

11. Weidlich D, Honecker J, Gmach O, et al. Measuring large lipid droplet sizes by probing restricted lipid diffusion effects with diffusion-weighted MRS at 3T. *Magn Reson Med*. 2019;81:3427-3439.

12. Nicolay K, Braun KP, Graaf RA, Dijkhuizen RM, Kruiskamp MJ. Diffusion NMR spectroscopy. *NMR Biomed*. 2001;14:94-111.

13. Ronen I, Valette J. Diffusion-weighted magnetic resonance spectroscopy. *eMagRes*. 2015;4:733-750.

14. Brandejsky V, Kreis R, Boesch C. Restricted or severely hindered diffusion of intramyocellular lipids in human skeletal muscle shown by in vivo proton MR spectroscopy. *Magn Reson Med*. 2012;67:310-316.

15. Cao P, Fan SJ, Wang AM, et al. Diffusion magnetic resonance monitors intramyocellular lipid droplet size in vivo. *Magn Reson Med*. 2015;73:59-69.

16. Verma SK, Nagashima K, Yaligar J, et al. Differentiating brown and white adipose tissues by high-resolution diffusion NMR spectroscopy. *J Lipid Res*. 2017;58:289-298.

17. Le Bihan D, Poupon C, Amadon A, Lethimonnier F. Artifacts and pitfalls in diffusion MRI. *J Magn Reson Imaging*. 2006;24:478-488.

18. Alsop DC. Phase insensitive preparation of single-shot RARE: application to diffusion imaging in humans. *Magn Reson Med*. 1997;38:527-533.

19. Gmach O, Bertsch A, Bilke-Krause C, Kulozik U. Impact of oil type and pH value on oil-in-water emulsions stabilized by egg yolk granules. *Colloids Surf A Physicochem Eng Asp*. 2019;581:123788.

20. Tycko R, Cho HM, Schneider E, Pines A. Composite pulses without phase distortion. *J Magn Reson*. 1985;61:90-101.

21. Van AT, Cervantes B, Kooijman H, Karampinos DC. Analysis of phase error effects in multishot diffusion-prepared turbo spin echo imaging. *Quant Imaging Med Surg*. 2017;7:238-250.

22. Pipe JG. Motion correction with PROPELLER MRI: application to head motion and free-breathing cardiac imaging. *Magn Reson Med*. 1999;42:963-969.

23. Murday JS, Cotts RM. Self-diffusion coefficient of liquid lithium. *J Chem Phys*. 1968;48:4938-5000.

24. Cui C, Wu X, Newell JD, Jacob M. Fat water decomposition using globally optimal surface estimation (GOOSE) algorithm. *Magn Reson Med*. 2015;73:1289-1299.

25. Boehm C, Diefenbach MN, Makowski MR, Karampinos DC. Improved body quantitative susceptibility mapping by using a variable-layer single-min-cut graph-cut for field-mapping. *Magn Reson Med*. 2021;85:1697-1712.

26. Shah A, Abámoff MD, Wu X. Optimal surface segmentation with convex priors in irregularly sampled space. *Med Image Anal*. 2019;54:63-75.

27. Engl HWH, Neubauer MA. *Regularization of Inverse Problems*. Dordrecht, Netherlands: Springer; 2000. p 322.

28. Guilmineau F, Kulozik U. Influence of a thermal treatment on the functionality of hen's egg yolk in mayonnaise. *J Food Eng*. 2007;78:648-654.

29. Eggers H, Brendel B, Duijndam A, Herigault G. Dual-echo Dixon imaging with flexible choice of echo times. *Magn Reson Med*. 2011;65:96-107.

SUPPORTING INFORMATION

Additional Supporting Information may be found online in the Supporting Information section.

FIGURE S1 Simulated longitudinal magnetization after preparation for a stimulated echo preparation with 90° hard pulses (left) and 90° MLEV scheme pulses. With MLEV scheme 90° a larger insensitivity towards frequency offsets can be observed

FIGURE S2 Diffusion signal decay curves at increasing diffusion times (different columns) for the water-fat emulsion phantoms and the coconut oil (different rows). At each diffusion time and the investigated phantom, the signal decay is mono-exponential. In the water-fat-emulsions a clear ADC decay is visible for increasing diffusion time, whereas such a trend is not visible in the coconut oil

7 Discussion

The non-invasive measurement of adipocyte size would have tremendous implications in the field of obesity and diabetes as described in chapter 2. DW-MR is a promising technique to perform such measurements. However, due to the small measurable effects and additional technical challenges, it is so far not possible to measure adipocyte size in large white adipocytes with MR especially when employing a clinical MR scanner. The present dissertation solves some important technical challenges in the DW-MR of fat-containing tissue and lays the foundation for the application of DW-MR in order to measure adipocyte size in white AT in vivo.

7.1 Review of Existing Literature

The present work is based on several preceding publications in the field of DW-MR. The developed methods shown in this dissertation predominantly build on developments in the field of restriction effects on DW-MR measurements and the findings regarding artifacts caused by scanner table vibrations. In the following, the existing literature is reviewed regarding the utilization of DW-MRS (section 7.1.1), artifacts on DW measurements due to vibrations (section 7.1.2) and the utilization of DW-MRI to investigate lipid diffusion (section 7.1.3):

7.1.1 Measurement of Lipid Droplet Size with DW-MRS

Numerous different models exist to describe the diffusion behavior in a diffusion restricted environment. Both, DW-MRS and DW-MRI have been applied to acquire the necessary DW signal to extract eventually microstructural properties. These techniques were successfully used and showed astonishing results in the characterization of pore size in sediments [116, 117], in the context of food science [130] and in the field of medicine. In medical applications the main use cases are the investigation of tumor microstructure [12] and structural information of the brain [124].

The purpose of this work was the investigation of the microstructure of white AT because of its high significance in metabolic research (please refer to chapter 2). Most of the existing applications of DW-MR have so far focused on the diffusion of water and the interaction of these water molecules with cellular restriction barriers. Translating the applied methodologies to study restricted diffusion properties of lipids constitutes a major challenge: The diffusivity of lipids is around two orders of magnitude smaller compared to water [13]. The slow diffusion of fatty acids results in a small mean free path length in experimental reasonable diffusion times. White adipocytes constitute very large cells with a large plasticity. The diameter of white adipocytes depends on the measurement method and is in the order of 50 - 150 μm [16]. In combination with a very slow lipid diffusion, the measurable effects observable in diffusion times achievable on a clinical scanner, are very small. This creates high requirements regarding the quality of the measured signal. The required diffusion encoding strength and diffusion time for the experiment are orders of magnitude higher then the ones used in the clinical routine. This creates additional technical challenges related to eddy currents and

having an increased sensitivity to any type of physiological tissue motion including involuntary movement [13]. In addition to the above challenges, the fat spectrum is much more complex than the water spectrum, consisting of multiple different peaks with different relaxation times [125] and potentially also different diffusion constants [126].

Especially, because of its capability to spectrally resolve different metabolites and also due to the high SNR, DW-MRS is a natural first candidate to study restricted diffusion of lipids. However, performed studies in this field remain limited.

In 2001, Lahrech et al. were the first to show restricted diffusion effects of lipids in rat tumors (approximate droplet diameter $< 5\ \mu m$) [131]. Also the size of intramyocellular lipids (approximate droplet diameter: 1-2 μm) were investigated in animals [14] and humans [132]. Verma et al. showed intriguing results applying DW-MRS in order to distinguish brown adipocytes (approximate droplet diameter $< 5\ \mu m$) from white adipocytes in a mouse model [15]. The previous work was mostly investigating lipid droplet size in animal models on a strong pre-clinical system. Also the hereby investigated tissues constitute of lipid droplets way smaller then the adipocytes of interest in this dissertation (droplet diameter $< 10\ \mu m$). The present work tries to apply DW-MRS to probe lipid droplet size on a clinical MR system in substantially larger lipid droplets compared to preceding works.

7.1.2 Reduction of Signal Loss Induced by Scanner Table Vibrations

As described in section 4.4.4, gradients can induce vibrations that can lead to signal loss in DW measurements. Early analysis of the vibrations of gradient coils mostly focused on the problems related to acoustic noise [133, 134]. In 2006, Hiltunen et al. were the first to investigate vibrations induced by a DW sequence (more precise a DTI sequence for brain applications) with laser interferometry. They measured the encountered displacements on a phantom and on the scanner hardware but did not report the influence on the DW MR measurements. In their study they found displacement amplitudes on the phantom surface of up to 100 μm, potentially leading to severe artifacts in their measurement protocol. [106] In the same year Ogura et al. observed differences in the measured ADC in phantoms when the phantoms were placed on the scanner table and placed on a decoupled table, indicated an influence of scanner table vibrations on DW measurements [135]. The first observation in a clinical in vivo protocol was observed in 2010: In a DTI protocol, a systematic artifact was found in posterior brain regions that are close to the scanner table leading to signal loss in the DW raw imaging data and quantification errors in the parameter maps extracted from the DTI processing [108]. This was especially severe in pediatric cases, when the patient weight is lower than the typical adult patient [109]. Gallichan et al. were the first to induce vibrations intentionally to use the scanner table as the driving force in a MR elastography experiment. They applied a "velocity-inducing" gradient before the actual DW module and changed the time interval between this additional gradient and the rest of the sequence. By analyzing the phase images at different time intervals, conclusions were drawn about viscoelastic properties of the system. [107]

The correction of artifacts induced by vibrations is not trivial. Rescaling regions with lost signal in the post-processing is challenging because the signal amplitude is already lost by intravoxel dephasing and the lost information can not be simply retrieved. Also the exact location and severity of the regions affected by signal loss depend on the local viscoelastic properties of the tissue and the exact coupling of the hardware with the investigated subject. This hampers potential signal re-scaling approaches. A prediction of the vibrations and subsequent correction is challenging because of the complex mechanical coupling between

scanner hardware and subject as well as the missing knowledge about mechanical tissue properties. Most promising approaches include the reduction of scanner table vibrations by modifications of the scanner hardware or the modification of the MR pulse sequence on the acquisition site to be less susceptible to this vibration artifacts or allow a correction scheme.

Modifications on the pulse sequence have been made by Mohammadi et al. to mitigate signal loss due to vibrations in DW-MR measurements employing partial Fourier. By acquiring two DW data sets with reversed phase-encoding direction, shifts of the acquired echo out of the k-space center can be corrected. [136] However, this technique is not suitable for reducing signal loss induced by intravoxel dephasing. To the best of the author's knowledge, no other technique to reduce the effect of hardware vibrations on the DW signal has been proposed so far.

7.1.3 Measurement of Lipid Droplet Size with DW-MRI

Applying single-voxel DW-MRS for lipid droplet size measurement has an important disadvantage that limits its clinical utility: The large voxel size of MRS result in a high sensitivity towards intra-voxel dephasing effects, which could results in quantification errors. Acquiring data with smaller voxel size would mitigate this effect and therefore the development of a high b-value and long diffusion time DW imaging sequence is an important step towards in vivo application.

DW-MRI is frequently applied to measure diffusion properties of water-containing tissues. The most dominant method that utilizes diffusion restriction effects is probably linked to the investigation of brain tissue, particularly white matter structures measured with DW-MRI [137]. Thereby, it is utilized that nerve axons will allow free diffusion along the nerve fiber and restrict diffusion perpendicular to the nerve fiber. DW imaging data is acquired with different directionality of the diffusion gradients and consequently a local estimation of the diffusion propagator can be obtained [138, 139].

Although these techniques explore the dominant diffusion directions, no quantitative information about the cellular structure is obtained. There are methods to extract parameters like the axon diameter [9–11] or other microstructural parameters of the brain [124]. Despite the great potential of quantitative measurements of white matter microstructure the approaches are predominantly used in research settings [140].

All the above mentioned techniques are focus on the diffusion of water. Probing spatially resolved diffusion properties of lipids suffer from the same drawbacks and challenges as MRS measurements (described in more detail in section 7.1.1). However, going from single-voxel DW-MRS to DW-MRI to probe restriction effects would come with distinct advantages: First, due to the smaller voxel size of MRI compared to single-voxel MRS, the sensitivity towards bulk motion could be reduced significantly [101]. Second, the spatial resolved DW raw imaging data could be utilized by incorporating the neighborhood information into a regularized fitting paradigm to increase the robustness of the parameter estimation. Third, acquiring spatially resolved lipid droplet size maps, would be very valuable because it allows the investigation of heterogeneous adipose tissue. Therefore, going from a spectroscopy to an imaging framework to probe adipose tissue microstructure could lay the foundation for in vivo measurements of adipocyte size.

In general, the literature applying DW imaging techniques to spatially resolved measure lipid droplet size is very limited. Work by Steidle et al. introduces a DW EPI sequence to measure the diffusion constant of lipids in subcutaneous fat and bone marrow [13]. However, the measurements suffered from vibrational artifacts and were only performed at one diffusion

time. Ohno et al. proposed a sequence to simultaneously measure water and lipid diffusion based on a DW-EPI sequence [141]. In their sequence design they only used b-values up to $3000 \frac{s}{mm^2}$ which resulted in a very small attenuation of the lipid signal. Because both of the mentioned approaches are based on a spin-echo diffusion weighting, the acquisition of multiple diffusion times is challenging. Increasing the diffusion time would only be possible by increasing TE which would result in a strong signal attenuation due to T_2 relaxation.

To allow the acquisition of longer diffusion times, the application of a stimulated echo preparation for DW is a natural choice [110]. The previously used EPI readout is very fast and offers great SNR efficiency but it suffers from off-resonance effects and especially from chemical shift artifacts in lipid DW measurements. One way to overcome this is the usage of a single shot TSE sequence that additionally does not additionally suffer from phase errors present in multi-shot acquisitions. To eliminate motion-induced and eddy current-induced phase errors, magnitude stabilizing gradients following Alsop's method can be introduced in the preparation and readout [91, 97]. In summary, a DW preparation based on a stimulated echo based DW preparation in combination with a single shot TSE sequence would be a promising candidate for probing lipid diffusion at high b-values and long diffusion times.

The same modeling of the signal decay utilized for the lipid droplet size estimation obtained by DW-MRS could be applied in the DW imaging framework by applying this equation on a voxel-by-voxel basis. However, the SNR in imaging sequences is inherently smaller compared to single-voxel MRS sequences because of the smaller voxel sizes. Therefore, more sophisticated fitting approaches exploiting an assumed low spatial variation of the lipid droplet diameter in a homogeneous tissue should be applied. The selection of the local estimate for the diameter can be regularized similar to work by Cui et al. [142] and Boehm et al [143]. This minimization problem can be solved via a graph cut algorithm employing a graph construction with convex priors that allows for unequally sampled space [144] in the dimension of the adipocyte cell size.

7.2 Present Work

The present work includes several contributions to the field of metabolic MR. JP-I shows for the first time that it is feasible to measure the droplet size in larger lipid droplets in vivo and on a clinical scanner using DW-MRS. JP-II proposes a methodology to mitigate vibration artifacts otherwise corrupting the acquired DW signal. The technique was tested with a single-voxel DW-MRS sequence but can in principle be also applied to other sequences. Finally, JP-III extended the initial work of JP-I and introduces a method for lipid droplet size mapping using DW-MRI that is capable of measuring the lipid droplet size in ex vivo white AT samples.

7.2.1 Novelty

Up to now, the assessment of AT microstructure was limited to small lipid droplets (diameter $\leq 10 \ \mu m$). The measurements were mostly performed in animal models with a preclinical MR system employing strong gradients. In JP-I it was shown for the first time, that lipid droplet size measurements are feasible in vivo on a clinical MR scanner in larger lipid droplets (diameter $\approx 40 \ \mu m - 50 \ \mu m$). To validate the method the lipid droplet size in water-fat-emulsion-phantoms was measured and compared to the two different reference measurements laser deflection and microscopic analysis. The lipid droplet diameters extracted from the water-

fat-emulsion-phantoms experiments showed great agreement with the validation measurements and the values extracted from the tibia bone marrow were consistent with the literature. This first proof of concept measurements were very important to push the technique further in the direction of in vivo measurement of larger adipocytes in subcutaneous or visceral adipose tissue which would be of high interest in metabolic research.

Scanner table vibrations were identified as a major source for artifacts in the measurements of high b-value DW-MRS. Therefore, modifications of the pulse sequence were proposed to mitigate the signal loss induced from vibrations shown in JP-II. This was the first time that a gradient pre-pulse was utilized to match the vibrational patterns during diffusion sensitizing periods in order to reduce signal loss. The idea how to mitigate signal loss was not only theoretically examined and proven by simulations but also validated by measuring the displacements of a phantom with laser interferometry. The displacement measurements indicated a similar displacement pattern in both DW periods when the additional gradient was applied and lipid diffusion measurements in phantoms and in vivo became more accurate and precise.

In JP-III, the feasibility of DW-MR to extract spatially resolved lipid droplet maps was presented. Previous work only showed maps containing microstructural information in water-containing tissues or a non statially resolved investigation of the diffusivity of lipids. Consequently, the present work represents the first time that spatially resolved lipid droplet diameter maps were successfully acquired and validated. The DW-TSE sequence based on a stimulated echo preparation was specifically designed to acquire high b-value and long diffusion time data focusing on lipid diffusion. Additionally, a novel post-processing framework utilizing a graph-cut approach to enforce smooth spatial variation of the extracted lipid droplet diameter was presented. Thereby, redundancy in the acquired data under the assumption of smoothy varying in space parametric maps could be utilized to stabilize the fitting process. The proposed method was validated in water-fat-emulsion phantoms and the applicability was shown by measuring the lipid droplet size in human white AT samples.

7.2.2 Impact

Given the potential that the non-invasive measurement of adipocyte size would offer in the field of diabetes and obesity research (refer to chapter 2), the impact of the presented methods can be considered as high. Methods presented so far were only capable of measuring the lipid droplet size in adipocytes smaller than a few micrometers [14, 15, 131, 132]. JP-I shows for the first time that those measurements are also possible in lipid droplets as large as 50 µm in diameter. It is a important proof of principle to show the feasibility of using DW-MR in this context. Additionally, the utilization of a clinical MR system can be seen as a milestone because it accelerates the translation of the technique in the clinical practice. However, using single-voxel DW-MRS for lipid droplet size measurements has important limitations for its clinical utility: Applying the DW-MRS sequence used in JP-I directly in vivo to investigate white AT can be considered as challenging because of the large motion sensitivity of the method. Therefore, a second pulse sequence to measure adipocyte size was proposed in JP-III. The DW-TSE imaging sequence based on a stimulated echo preparation allows the acquisition of strong DW and long diffusion time data necessary to measure restriction effects of lipids but with much smaller voxel size than necessary with DW-MRS. The smaller voxel size reduces the sensitivity towards motion and renders a clinical application in regions with residual physiological motion realistic. In this publication, it was shown for the first time that adipocyte size can be measured with DW-MR in white AT samples that the measured adipozyte size

correlates well with values obtained from histology. The DW-MRI sequence can be seen as an excellent candidate for an ex-vivo adipose tissue sample study and for the future application of the technique in vivo. Especially due to the strong DW applied in JP-I and JP-III, scanner table vibrations can be identified as a major source of quantification errors. Due to the fact that the acquired signal needs to be of high quality to extract microstructural information, methods to reduce artifacts are highly desirable. Therefore, a methodology was developed and presented in JP-II to mitigate those errors. The presented improvements are of large interest in the specialist research setting of measuring small effects with very high DW. But also in clinical application, the sequence modifications presented in JP-II will be useful. The frequent usage of high b-value DW imaging in the context of brain examinations and the already published occurrence of vibration-induced artifacts shows the need for solutions to mitigate the effects of these vibration artifacts. JP-II offers a methodology that is easily applicable in routinely used DW imaging sequences with very limited penalty on the acquisition time.

7.2.3 Limitations

The presented work has some limitations: Based on the presented modeling of the DW signal decay curve, it was only possible to extract a mean lipid droplet diameter although the underlying particle size distribution might be more complex. However, it was shown in simulations that the deviations from the real diameter is rather small when the particle size distribution is assumed to be Gaussian. This applies to both the DW-MRS in JP-I and DW-MRI in JP-III sequences. In JP-I the method was only validated by measuring water-fat-emulsion phantoms with smaller lipid droplet sizes compared to the target application white AT. However, a great agreement between the method and the validation measurements were found. Therefore, it was assumed that the presented method is also valid to measure larger lipid droplets. Additional to this, the extracted lipid droplet diameters in the tibia bone marrow are close to literature values. A translation of the single-voxel DW-MRS sequence to anatomical regions with macroscopic physiological motion (induced by the respiratory or the cardiac cycle) was found to be challenging due to its motion sensitivity.

To overcome this restriction of the single-voxel DW-MRS method and to allow spatially resolved lipid droplet size measurements, the DW-TSE sequence was introduced in JP-III. Also this technique has limitations: By the design of the imaging sequence the signal is the sum over several fat peaks that have different T_1 relaxation times and potentially also different diffusion constants. This is not incorporated in the modeling which assumes a single component with a defined free diffusion constant and relaxation constant. However, as a large part of the signal should be associated with the methylene fat peak at 1.3 ppm, the contribution of these spins should be dominant. In the investigated adipose tissue samples a spatial heterogeneity of the droplet size maps was observed using the MR-based imaging technique. Given the fact that no reference measurement was performed in multiple locations within one sample, it is unclear whether the observed variation is real or an artifact arising from the measurement. However, a good correlation was observed with the estimated mean adipocyte diameter when comparing the MR-based method and histology. In addition, a smooth spatial variation of the lipid droplet size was assumed although this point was not proven. Given the fact that subcutaneous fat samples appear to be very homogenous on biopsies and no spatial variations are visible on MR images of this region, the assumption of a smooth variation of the droplet diameter might be justifiable. The balancing term λ that regulates the importance of the neighborhood information was not optimized in detail. Based on the SNR of the acquired DW data, one parameter λ was selected. Optimizing λ

based on the obtained DW data could further reduce the bias and standard deviation in the estimation and should be discussed in further research. Also the number of investigated water-fat emulsion phantoms and adipose tissue samples is rather small. However, even in this limited study a significant correlation between the MR-based measurements and the validation measurements was observed.

The application of the VMG in JP-II has the following limitations: First, the laser interferometer data and the DW-MRS data were acquired in different phantoms and in a subsequent fashion because experimental limitation did not allow a simultaneously acquisition in the same phantom. Therefore, a slight mismatch between the observed effects could be explained by the different viscoelastic properties of the phantoms. However, also in this merged dataset the overall trend was clearly visible. Finally, the laser interferometry measurements are only capable of acquiring surface information and cannot reveal three dimensional volume information. Therefore, the phase dispersion calculated in this work, was only based on a 2D surface. As phase dispersion effects are even visible on a 2D surface, phase dispersion effects are expected to be present and may be even more severe if the measurements would have been extended to a 3D analysis.

7.3 Perspectives

The presented methodologies in JP-I and JP-III lay the foundation for the application of DW-MR measurements for the in vivo probing of AT microstructure. The next steps to achieve this goal is a formal validation of the proposed measurement framework with more AT samples to prove that the method is really working well in the target organ. JP-III included ten investigated AT samples and a significant correlation was already found in this small number of specimens. However, more AT samples will strengthen the validity and an extension of the presented data is currently ongoing. Additionally, the techniques should be tested for in vivo measurement of adipocyte size in the subcutaneous fat in humans. Because residual motion artifacts are expected in the subcutaneous fat, experimental optimization and additional correction schemes might be necessary to obtain robust estimates for the mean adipocyte size. In vivo, the diffusion constant is larger compared to the ex vivo case (because of the temperature difference) and therefore the measurable effects should be larger which might help in improving the noise performance of the parameter estimation. When a reliable non-invasive in vivo measurement of adipocyte size is achieved, large scale longitudinal human studies are of particular interest. In lifestyle intervention studies, the usefulness of applying DW-MR techniques in the context of obesity to monitor interventions and disease progression can be evaluated. A successfully implemented adipocyte size measurement sequence can be added to the examination and the obtained adipocyte size measurements can be compared to other clinical parameters obtained by the department of nutritional medicine. Using the adipocyte size measurement based on DW-MR as an early predictor for diabetes could potentially show benefit in insulin resistance studies and is therefore of high clinical interest. Such prospective clinical studies would be necessary to translate the presented technique to a clinical application. The necessity for very high b-values and diffusion times constitute a severe vulnerability of the described methods to any type of motion. Therefore it is recommended to include the gradient pre-pulse presented in JP-II in any type of high b-value DW measurement used to obtain the adipocyte size. DW-MR measurements are also frequently applied in today's clinical routine and all the measurements rely on the utilization of gradient pulses with often high gradient strength. The occurrence of vibrations and their potential to cause artifacts is

well-known. Especially, if parameters are measured that exceed a simple DW imaging or ADC estimation, small artifacts can lead to severe quantification errors and wrong findings. DTI is such a technology that is prone to errors caused by vibrations. When DTI data is used for a more sophisticated modeling like fibertracking which is used for surgical planing [145], the quality of the measured data is very important for the clinical care of the patient. The general trend towards stronger DW and more powerful gradients will increase the severity of occurring vibrations and therefore there is a high need for sophisticated artifact reduction schemes. [146]

8 Conclusion

The present dissertation represents an important step towards non invasive adipocyte size measurements. DW-MR is a powerful tool to assess tissue microstructure and was so far mostly applied in water-containing tissue. Due to small measurable restriction effects when lipids are diffusing within adipocytes, applying those measurements in adipose tissue was previously not possible with MR. Based on three embedded journal publications the presented methodologies allow for the first time the application of DW-MR measurements for in vivo probing of adipose tissue on a clinical MR scanner. First, a technique to estimate a mean adipocyte size was established using DW-MRS. Second, a method to reduce the effect of vibrational artifacts in DW-MR measurements was presented. Third, the methodology of the first publication was extended to allow the spatially resolved acquisition of adipocyte size estimates using DW-MRI.

As adipose tissue composition plays a crucial role in a variety of metabolic diseases and microstructural alterations are often accompanying disease progression, the presented techniques for MR-based adipocyte size estimation will be a valuable tool to understand pathophysiological processes. In the field of obesity and diabetes type 2 the non invasive measurement of adipocyte size could eventually work as a marker for disease activity, progression and therapy effectiveness.

The present work lays the foundation stone for further improvements in sequence design, sequence parameter selection and post-processing in the field of MR-based adipocyte size measurements, enabling an evaluation of the presented techniques in large-scale longitudinal studies. Metabolic diseases are affecting a high percentage of people living in the industrialized world. Establishing the presented measurements techniques in the clinical routine will eventually influence the medical treatment of a high number of patients.

Acknowledgments

At the very beginning, I would like to express my deep gratitude to all the people that supported me during this dissertation. Without their help, certain parts of this work would not have been possible, the dissertation would have been of limited scope, and it would definitely not have been such a great experience for me personally. I really enjoyed my PhD thanks to the supportive, friendly, and inspiring environment. There are, of course, a few people who I would like to thank individually:

My deepest gratitude goes to Professor Dimitrios Karampinos, who has been much more than just my group leader. Thank you, Dimitris, for being the best supervisor that I could ever imagine (finally, also acknowledged by the TUM!). Thank you for always supporting me with all the issues I had, let it be work-related or personally. During my time in the BMRR group, I learnt a lot from you and this shaped my professional and personal identity. I share a lot of great memories with you that would be simply too numerous to list here. Among these, I remember the baptism of your children in Athens, self-cooked group dinners, being interrogated together at the Munich Airport before our flight to Israel, night shifts before important deadlines and many more. For me, you are a role model for a great supervisor and scientist. I would like to thank you for everything I learnt from you and for being a great friend in the past five years.

Working in the medical field is a highly rewarding experience, but without the help and support of people with a medical background it would only be half as interesting. First of all and most prominently in this context, I would like to thank Sarah Schläger, who started as a medical student in one of my projects, but was eventually much more important in my research activities. Sarah, thanks for the endless hours of explaining medical topics to me and working together with me on numerous projects. You have shared your rich medical knowledge with me, which enhanced my understanding and kept my motivation high. Your willingness to learn about the technique and the physics behind it was absolutely inspiring and working with you was always a great experience for me. Sarah, I enjoyed every minute of it, so thank you for all your help during my dissertation.

With the technical background from my education, biological processes were always a mystery to me. Due to a collaboration with the chair of nutritional medicine, we got in contact with the experts in the field, who were willing to help us regarding our deficits. Thank you, Professor Hans Hauner, for supporting my work, always being reachable for discussion and keeping an eye on the big picture. Special thanks also to Julius Honecker. Thank you for the endless hours of driving around in Munich to collect the human tissue samples, for helping me in the laboratory, for long discussions about the project and for answering every little biological question that I had.

Another very important person regarding the success of this work was Professor Rainer Burgkart. Professor Burgkart, you manufactured a wooden table in your leisure time that made all the measurements shown in three embedded journal publications possible. And all this despite the fact that you barely knew me at that point and that we had only shared a short discussion during a lab tour before that. Next to your multiple tasks in the clinics and research, you took the time to help an unexperienced and young student, and thus enabled

research that would not have been possible otherwise. In my opinion, you truly embody a curious and altruistic researcher, and I would like to express my deep appreciation for this.

One of my projects I could not have realized without the help and initiative of Marcus Mäder from the Chair of Vibro-Acoustics within mechanical engineering. Thank you for building up such a fruitful collaboration within just a couple of days and helping me with all your expertise and industry contacts!

We, as a research group that relies on the usage of proprietary software, can only perform successful research with the help of our great industrial collaborators. Therefore, I would like to thank our partners and friends from Philips Healthcare for all their help. Thank you, Andy, Kurt, Christoph, and Kilian.

I would also like to thank my second supervisor, Professor Björn Menze, for always having time for me and supporting me during this dissertation! Your input was always well appreciated!

A factor that should never be underestimated is the influence of family and friends outside of the working environment. In particular, I would like to thank my parents for enabling me my education and teaching me values that are also applicable in professional life. In the same breath, I would also like to thank my brother Daniel for always being there for me. You three have been very supportive throughout my whole dissertation and were always curious about the progress of my projects although it was sometimes not easy for me to explain the topics. Thank you for tolerating reduced communication in stressful times and for supporting me in every possible way in the last years. Without your support and love, I would not have reached this point in my professional life!

Last but definitely not least, I would like to thank my research group! The BMRR group is one of the greatest environments to perform research or to work in general. Not only is it a research environment that is strongly motivating and inspiring, but also a very warm and welcoming family. Special thanks to Stefan, Barbara, Anh, and Michael, who were already there when I started my master thesis and who taught me everything I now know about programming and research. Max, Sophia, Stephan, Christoph, Ronja, and Sean: Together with you, I spent most of my days in the office. Thanks for making this such a great experience and thanks also for so much fun during my PhD time! The next generation of researchers with a technical background within the group are Mark, Chris, and Ely. It was great working with you and have fun in the best research group I could imagine! I also would like to thank the students that I supervised, especially Marco and Franziska - it might sound unoriginal, but I really think that I learned more from you than the other way around. Thanks to everybody that helped me with the clinical studies or explained all my medical questions to me. There, I would like to thank Christian, Lisa, Cora, Jan S., Nico, Daniela, Jan K. and Thomas. One of the, in my opinion, researchers with the deepest understanding of MR physics is Carl Ganter. Carl, thank you a lot for being my mentor, regularly coming by at our Thursday's team building events and answering every question I had. With all of you (the BMRR family and the extended BMRR family), I will always remember the travels to exotic conference locations and the associated holiday trips (ideally booked with Kaczmarz's tours!), team building on Thursdays, making mulled wine with our high-tech lab equipment, nerf gun battles after hours, the group retreats, skiing trip, hiking, Bavarian curling, BBQs, Christmas and summer parties, having beers at Johannis Cafe, disco breaks before deadlines and many, many more great memories. Thank you for making this dissertation a unique experience and so much fun!

I hope that I can stay in touch with all of you and wish you all the best for the future!

List of Symbols and Abbreviations

Symbols

α_m	Roots obtained from Differential Equation of Bessel Functions
ΔB_{inhom}	Local Magnetic Field Inhomogeneity [Hz]
ΔE	Energy Difference [J]
Δ	Diffusion Time [s]
δ	Effective Duration of a Trapezoidal Gradient [s]
ϵ	Ramping Time of a Trapezoidal Gradient [s]
γ	Gyromagnetic Ratio $\left[\mathrm{Hz\,T^{-1}}\right]$
μ	Magnetic Moment $\left[\mathrm{N\,m\,T^{-1}}\right]$
ω_0	Lamor Frequency $\left[rads^{-1}\right]$
$\overrightarrow{r}$	Spatial Location Vector [m]
$\rho(x)$	Spin Density $\left[m^{-3}\right]$
φ	Phase [rad]
$E_\downarrow$	Energy of the Spin-down Energy Level [J]
$E_\uparrow$	Energy of the Spin-up Energy Level [J]
J	Inherent Angular Momentum $\left[\mathrm{kg\,m^2\,s^{-1}}\right]$
$<X>^2$	Average Squared Distance [m]
2D	Two-Dimensional
3D	Three-Dimensional
^{1}H	Proton
A	Surface Area $\left[m^2\right]$
A/V	Surface to Volume Ratio $\left[m^{-1}\right]$
ADC	Apparent Diffusion Constant $\left[mm^2 s^{-1}\right]$
B	Magnetic Field [T]

b	B-value $[mm^{-2}s]$
B_0	Main Magnetic Field [T]
$B_1(t)$	Time-varying Magnetic Field [T]
B_{eff}	Effective Magnetic Field [T]
D	Diffusion Coefficient $[mm^2s^{-1}]$
d	Diameter of Spherical Restriction Barrier [m]
D_{free}	Free Diffusion Constant $[mm^2s^{-1}]$
G	Magnetic field Gradient $[Tm^{-1}]$
G_x	Spatial x Component of the Magnetic field Gradient $[Tm^{-1}]$
G_y	Spatial y Component of the Magnetic field Gradient $[Tm^{-1}]$
G_z	Spatial z Component of the Magnetic field Gradient $[Tm^{-1}]$
k	K-space Variable $[m^{-1}]$
k_b	Boltzmann's Constant $[JK^{-1}]$
M	Magnetization
M_0	Equilibrium Magnetization
M_{ex}	Excited Magnetization
M_{xy}	Transverse Magnetization
M_x	Spatial x Component of the Magnetization Vector
M_y	Spatial y Component of the Magnetization Vector
M_z	Spatial z Component of the Magnetization Vector
N	Number of Spins
S	Signal
S_0	Signal without Diffusion Attenuation
T	Temperature$[K]$
t	Time [s]
T_1	Spin-Lattice (Longitudinal) Relaxation Time [s]
T_2	Spin-Spin (Transverse) Relaxation Time [s]
T_2'	Reversible Relaxation Time [s]
T_2*	Effective Transverse Relaxation Time [s]

V	Volume [m^3]
x	Image-space Variable [m]

Abbreviations

AT	Adipose Tissue
BMI	Body Mass Index
DTI	Diffusion Tensor Imaging
DW	Diffusion Weighted
EPI	Echo Planar Imaging
FID	Free Induction Decay
IDF	International Diabetes Federation
MHO	Metabolically Healthy Obese
MLEV	Malcolm-Levitt
MR	Magnetic Resonance
MRI	Magnetic Resonance Imaging
MRS	Magnetic Resonance Spectroscopy
NMR	Nuclear Magnetic Resonance
PGSE	Pulsed-Gradient Spin-Echo
PRESS	Point-Resolved Spectroscopy
RF	Radio Frequency
SNR	Signal-to-Noise Ratio
STEAM	Stimulated Echo Acquisition Mode
TE	Echo Time
TM	Mixing Time
TSE	Turbo Spin Echo
VMG	Vibration Matching Gradient
WHO	World Health Organization

List of Figures

Bibliography

[1] M. Finucane, G. Stevens, M. Cowan, G. Danaei, J. Lin, C. Paciorek, G. Singh, H. Gutier-rez, Y. Lu, A. Bahalim, F. Farzadfar, L. M. Riley, and M. Ezzati, "National, regional, and global trends in body-mass index since 1980: systematic analysis of health examination surveys and epidemiological studies with 960 country-years and 9.1 million participants," *Lancet*, vol. 377, no. 9765, pp. 557–567, 2011.

[2] A. Hruby and F. B. Hu, "The epidemiology of obesity: a big picture," *Pharmacoeconomics*, vol. 33, no. 7, pp. 673–689, 2015.

[3] A. von Ruesten, A. Steffen, A. Floegel, G. Masala, A. Tjønneland, J. Halkjaer, D. Palli, N. J. Wareham, R. J. Loos, T. I. Sørensen, and H. Boeing, "Trend in obesity prevalence in european adult cohort populations during follow-up since 1996 and their predictions to 2015," *PloS One*, vol. 6, no. 11, p. e27455, 2011.

[4] S. Laforest, J. Labrecque, A. Michaud, K. Cianflone, and A. Tchernof, "Adipocyte size as a determinant of metabolic disease and adipose tissue dysfunction," *Critical reviews in Clinical Laboratory Sciences*, vol. 52, no. 6, pp. 301–313, 2015.

[5] L. B. Salans, S. W. Cushman, and R. E. Weismann, "Studies of human adipose tissue adipose cell size and number in nonobese and obese patients," *The Journal of Clinical Investigation*, vol. 52, no. 4, pp. 929–941, 1973.

[6] M. Bahceci, D. Gokalp, S. Bahceci, A. Tuzcu, S. Atmaca, and S. Arikan, "The correlation between adiposity and adiponectin, tumor necrosis factor α, interleukin-6 and high sensitivity c-reactive protein levels. is adipocyte size associated with inflammation in adults?," *Journal of Endocrinological Investigation*, vol. 30, no. 3, pp. 210–214, 2007.

[7] S. G. Dubois, L. K. Heilbronn, S. R. Smith, J. B. Albu, D. E. Kelley, E. Ravussin, and L. A. A. R. Group, "Decreased expression of adipogenic genes in obese subjects with type 2 diabetes," *Obesity*, vol. 14, no. 9, pp. 1543–1552, 2006.

[8] R. Roberts, L. Hodson, A. Dennis, M. Neville, S. Humphreys, K. Harnden, K. Micklem, and K. Frayn, "Markers of de novo lipogenesis in adipose tissue: associations with small adipocytes and insulin sensitivity in humans," *Diabetologia*, vol. 52, no. 5, p. 882, 2009.

[9] Y. Assaf, T. Blumenfeld-Katzir, Y. Yovel, and P. J. Basser, "Axcaliber: a method for measuring axon diameter distribution from diffusion mri," *Magnetic Resonance in Medicine*, vol. 59, no. 6, pp. 1347–1354, 2008.

[10] D. Barazany, P. J. Basser, and Y. Assaf, "In vivo measurement of axon diameter distribution in the corpus callosum of rat brain," *Brain*, vol. 132, no. 5, pp. 1210–1220, 2009.

[11] H. H. Ong and F. W. Wehrli, "Quantifying axon diameter and intra-cellular volume fraction in excised mouse spinal cord with q-space imaging," *Neuroimage*, vol. 51, no. 4, pp. 1360–1366, 2010.

[12] O. Reynaud, "Time-dependent diffusion mri in cancer: tissue modeling and applications," *Frontiers in Physics*, vol. 5, p. 58, 2017.

[13] G. Steidle, F. Eibofner, and F. Schick, "Quantitative diffusion imaging of adipose tissue in the human lower leg at 1.5 t," *Magnetic Resonance in Medicine*, vol. 65, no. 4, pp. 1118–1124, 2011.

[14] P. Cao, S.-J. Fan, A. M. Wang, V. B. Xie, Z. Qiao, G. M. Brittenham, and E. X. Wu, "Diffusion magnetic resonance monitors intramyocellular lipid droplet size in vivo," *Magnetic Resonance in Medicine*, vol. 73, no. 1, pp. 59–69, 2015.

[15] S. K. Verma, K. Nagashima, J. Yaligar, N. Michael, S. S. Lee, T. Xianfeng, V. Gopalan, S. A. Sadananthan, R. Anantharaj, and S. S. Velan, "Differentiating brown and white adipose tissues by high-resolution diffusion nmr spectroscopy," *Journal of Lipid Research*, vol. 58, no. 1, pp. 289–298, 2017.

[16] S. Laforest, A. Michaud, G. Paris, M. Pelletier, H. Vidal, A. Géloën, and A. Tchernof, "Comparative analysis of three human adipocyte size measurement methods and their relevance for cardiometabolic risk," *Obesity*, vol. 25, no. 1, pp. 122–131, 2017.

[17] K. G. M. M. Alberti, P. Zimmet, and J. Shaw, "Metabolic syndrome—a new world-wide definition. a consensus statement from the international diabetes federation," *Diabetic Medicine*, vol. 23, no. 5, pp. 469–480, 2006.

[18] E. Kylin, "Studien ueber das hypertonie-hyperglykamie-hyperurikamiesyndrom," *Zentralblatt Fuer Innere Medizin*, vol. 44, pp. 105–127, 1923.

[19] B. Balkau, P. Valensi, E. Eschwège, and G. Slama, "A review of the metabolic syndrome," *Diabetes and Metabolism*, vol. 33, no. 6, pp. 405–13, 2007.

[20] World Health Organization, "Definition, diagnosis and classification of diabetes mellitus and its complications: report of a who consultation. part 1, diagnosis and classification of diabetes mellitus," tech. rep., World Health Organization, 1999.

[21] B. Balkau, "Comment on the provisional report from the who consultation. european group for the study of insulin resistance (egir)," *Diabet Med*, vol. 16, pp. 442–443, 1999.

[22] E. Panel, "Executive Summary of the Third Report of the National Cholesterol Education Program (NCEP) Expert Panel on Detection, Evaluation, and Treatment of High Blood Cholesterol in Adults (Adult Treatment Panel III)," *JAMA*, vol. 285, pp. 2486–2497, 05 2001.

[23] G. D. Kolovou, K. K. Anagnostopoulou, K. D. Salpea, and D. P. Mikhailidis, "The prevalence of metabolic syndrome in various populations," *The American journal of the Medical Sciences*, vol. 333, no. 6, pp. 362–371, 2007.

[24] B. Isomaa, P. Almgren, T. Tuomi, B. Forsén, K. Lahti, M. Nissen, M.-R. Taskinen, and L. Groop, "Cardiovascular morbidity and mortality associated with the metabolic syndrome," *Diabetes Care*, vol. 24, no. 4, pp. 683–689, 2001.

[25] P. Anderson, J. Critchley, J. Chan, C. Cockram, Z. Lee, G. Thomas, and B. Tomlinson, "Factor analysis of the metabolic syndrome: obesity vs insulin resistance as the central abnormality," *International Journal of Obesity*, vol. 25, no. 12, pp. 1782–1788, 2001.

[26] E. Bonora, S. Kiechl, J. Willeit, F. Oberhollenzer, G. Egger, G. Targher, M. Alberiche, R. C. Bonadonna, and M. Muggeo, "Prevalence of insulin resistance in metabolic disorders: the bruneck study.," *Diabetes*, vol. 47, no. 10, pp. 1643–1649, 1998.

[27] R. W. Nesto, "The relation of insulin resistance syndromes to risk of cardiovascular disease," *Reviews in Cardiovascular Medicine*, vol. 4, no. S6, pp. 11–18, 2019.

[28] J. O. Hill, H. R. Wyatt, and J. C. Peters, "Energy balance and obesity," *Circulation*, vol. 126, no. 1, pp. 126–132, 2012.

[29] Expert Panel on the Identification and Treatment of Overweight and Obesity in Adults (US) and National Heart and Lung and Blood Institute and National Institute of Diabetes and Digestive and Kidney Diseases (US), *Clinical guidelines on the identification, evaluation, and treatment of overweight and obesity in adults: the evidence report.* No. 98, National Institutes of Health, National Heart, Lung, and Blood Institute, 1998.

[30] A. Vegiopoulos, M. Rohm, and S. Herzig, "Adipose tissue: between the extremes," *The EMBO Journal*, vol. 36, no. 14, pp. 1999–2017, 2017.

[31] J. Blundell, A. Dulloo, J. Salvador, and G. Fruhbeck, "Beyond bmi–phenotyping the obesities," *Obesity Facts*, vol. 7, no. 5, pp. 322–328, 2014.

[32] E. M. Bomberg, J. R. Ryder, R. C. Brundage, R. J. Straka, C. K. Fox, A. C. Gross, M. M. Oberle, C. T. Bramante, S. D. Sibley, and A. S. Kelly, "Precision medicine in adult and pediatric obesity: a clinical perspective," *Therapeutic Advances in Endocrinology and Metabolism*, vol. 10, 2019.

[33] R. H. Eckel, S. E. Kahn, E. Ferrannini, A. B. Goldfine, D. M. Nathan, M. W. Schwartz, R. J. Smith, and S. R. Smith, "Obesity and type 2 diabetes: what can be unified and what needs to be individualized?," *The Journal of Clinical Endocrinology & Metabolism*, vol. 96, no. 6, pp. 1654–1663, 2011.

[34] M. Blüher, "Are metabolically obese individuals are really healthy?," in *Endocrine Abstracts*, vol. 35, BioScientifica, 2014.

[35] M. Blüher, "Metabolically healthy obesity," *Endocrine Reviews*, vol. 41, no. 3, pp. 405–420, 2020.

[36] S. Virtue and A. Vidal-Puig, "Adipose tissue expandability, lipotoxicity and the metabolic syndrome—an allostatic perspective," *Biochimica et Biophysica Acta (BBA)-molecular and cell biology of lipids*, vol. 1801, no. 3, pp. 338–349, 2010.

[37] W. Garvey, A. Garber, J. Mechanick, G. Bray, S. Dagogo-Jack, D. Einhorn, G. Grunberger, Y. Handelsman, C. Hennekens, D. Hurley, J. McGill, P. Palumbo, and G. Umpierrez, "American association of clinical endocrinologists and american college of endocrinology position statement on the 2014 advanced framework for a new diagnosis of obesity as a chronic disease," *Endocrine Practice*, vol. 20, no. 9, pp. 977–989, 2014.

[38] C. M. Phillips, "Metabolically healthy obesity: personalised and public health implications," *Trends in Endocrinology & Metabolism*, vol. 27, no. 4, pp. 189–191, 2016.

[39] S. Chatterjee, K. Khunti, and M. J. Davies, "Type 2 diabetes," *The Lancet*, vol. 389, no. 10085, pp. 2239–2251, 2017.

[40] G. Wilcox, "Insulin and insulin resistance," *Clinical Biochemist Reviews*, vol. 26, no. 2, p. 19, 2005.

[41] C. Bommer, V. Sagalova, E. Heesemann, J. Manne-Goehler, R. Atun, T. Bärnighausen, J. Davies, and S. Vollmer, "Global economic burden of diabetes in adults: projections from 2015 to 2030," *Diabetes Care*, vol. 41, no. 5, pp. 963–970, 2018.

[42] S. E. Inzucchi, R. M. Bergenstal, J. B. Buse, M. Diamant, E. Ferrannini, M. Nauck, A. L. Peters, A. Tsapas, R. Wender, and D. R. Matthews, "Management of hyperglycemia in type 2 diabetes: a patient-centered approach: position statement of the american diabetes association (ada) and the european association for the study of diabetes (easd)," *Diabetes Spectrum*, vol. 25, no. 3, pp. 154–171, 2012.

[43] T. Vos, C. Allen, M. Arora, R. M. Barber, Z. A. Bhutta, A. Brown, A. Carter, D. C. Casey, F. J. Charlson, A. Z. Chen, *et al.*, "Global, regional, and national incidence, prevalence, and years lived with disability for 310 diseases and injuries, 1990–2015: a systematic analysis for the global burden of disease study 2015," *The Lancet*, vol. 388, no. 10053, pp. 1545–1602, 2016.

[44] R. Williams, "Medical and economic case for prevention of type 2 diabetes and cardiovascular disease," *European Heart Journal Supplements*, vol. 7, pp. D14–D17, 2005.

[45] I. M. Stratton, A. I. Adler, H. A. W. Neil, D. R. Matthews, S. E. Manley, C. A. Cull, D. Hadden, R. C. Turner, and R. R. Holman, "Association of glycaemia with macrovascular and microvascular complications of type 2 diabetes (ukpds 35): prospective observational study," *Bmj*, vol. 321, no. 7258, pp. 405–412, 2000.

[46] American Diabetes Association, "Diagnosis and classification of diabetes mellitus," *Diabetes Care*, vol. 28, no. S37, pp. S5–S10, 2005.

[47] S. E. Inzucchi, R. M. Bergenstal, J. B. Buse, M. Diamant, E. Ferrannini, M. Nauck, A. L. Peters, A. Tsapas, R. Wender, and D. R. Matthews, "Management of hyperglycemia in type 2 diabetes, 2015: a patient-centered approach: update to a position statement of the american diabetes association and the european association for the study of diabetes," *Diabetes Care*, vol. 38, no. 1, pp. 140–149, 2015.

[48] N. Sattar, A. Gaw, O. Scherbakova, I. Ford, D. S. J. O'Reilly, S. M. Haffner, C. Isles, P. W. Macfarlane, C. J. Packard, S. M. Cobbe, and J. Shepherd, "Metabolic syndrome with and without c-reactive protein as a predictor of coronary heart disease and diabetes in the west of scotland coronary prevention study," *Circulation*, vol. 108, no. 4, pp. 414–419, 2003.

[49] E. Ahlqvist, P. Storm, A. Käräjämäki, M. Martinell, M. Dorkhan, A. Carlsson, P. Vikman, R. B. Prasad, D. M. Aly, P. Almgren, Y. Wessman, N. Shaar, P. Spegel, H. Mulder, E. Lindholm, O. Melander, O. Hansson, U. Malmqvist, A. Lernmark, K. Lahti, T. Forsen,

T. T. Tuomi, A. H. Rosengreen, and L. Groop, "Novel subgroups of adult-onset diabetes and their association with outcomes: a data-driven cluster analysis of six variables," *The Lancet Diabetes & endocrinology*, vol. 6, no. 5, pp. 361–369, 2018.

[50] S. S. Choe, J. Y. Huh, I. J. Hwang, J. I. Kim, and J. B. Kim, "Adipose tissue remodeling: its role in energy metabolism and metabolic disorders," *Frontiers in Endocrinology*, vol. 7, p. 30, 2016.

[51] K. L. Spalding, E. Arner, P. O. Westermark, S. Bernard, B. A. Buchholz, O. Bergmann, L. Blomqvist, J. Hoffstedt, E. Näslund, T. Britton, H. Concha, M. Hassan, M. Ryden, J. Frisen, and P. Arner, "Dynamics of fat cell turnover in humans," *Nature*, vol. 453, no. 7196, pp. 783–787, 2008.

[52] E. Ravussin and S. R. Smith, "Increased fat intake, impaired fat oxidation, and failure of fat cell proliferation result in ectopic fat storage, insulin resistance, and type 2 diabetes mellitus," *Annals of the New York Academy of Sciences*, vol. 967, no. 1, pp. 363–378, 2002.

[53] S. L. Appleton, C. J. Seaborn, R. Visvanathan, C. L. Hill, T. K. Gill, A. W. Taylor, and R. J. Adams, "Diabetes and cardiovascular disease outcomes in the metabolically healthy obese phenotype: a cohort study," *Diabetes Care*, vol. 36, no. 8, pp. 2388–2394, 2013.

[54] T. McLaughlin, A. Sherman, P. Tsao, O. Gonzalez, G. Yee, C. Lamendola, G. Reaven, and S. Cushman, "Enhanced proportion of small adipose cells in insulin-resistant vs insulin-sensitive obese individuals implicates impaired adipogenesis," *Diabetologia*, vol. 50, no. 8, pp. 1707–1715, 2007.

[55] C. Weyer, J. Foley, C. Bogardus, P. Tataranni, and R. Pratley, "Enlarged subcutaneous abdominal adipocyte size, but not obesity itself, predicts type ii diabetes independent of insulin resistance," *Diabetologia*, vol. 43, no. 12, pp. 1498–1506, 2000.

[56] F. Bloch, "Nuclear induction," *Physical Review*, vol. 70, no. 7-8, p. 460, 1946.

[57] E. M. Purcell, H. C. Torrey, and R. V. Pound, "Resonance absorption by nuclear magnetic moments in a solid," *Physical Review*, vol. 69, no. 1-2, p. 37, 1946.

[58] Z.-P. Liang and P. C. Lauterbur, *Principles of magnetic resonance imaging: a signal processing perspective.* SPIE Optical Engineering Press, 2000.

[59] W. Gerlach and O. Stern, "Das magnetische moment des silberatoms," *Zeitschrift für Physik*, vol. 9, no. 1, pp. 353–355, 1922.

[60] P. Zeeman, "The effect of magnetisation on the nature of light emitted by a substance," *Nature*, vol. 55, no. 347, 1897.

[61] S. Goldstein, "Boltzmann's approach to statistical mechanics," in *Chance in Physics*, vol. 574, pp. 39–54, Springer, 2001.

[62] A. Abragam, *The principles of nuclear magnetism.* No. 32, Oxford university press, 1961.

[63] C. P. Slichter, *Principles of magnetic resonance*, vol. 1. Springer Science & Business Media, 2013.

[64] R. Damadian, "Tumor detection by nuclear magnetic resonance," *Science*, vol. 171, no. 3976, pp. 1151–1153, 1971.

[65] E. L. Hahn, "Nuclear induction due to free larmor precession," *Physical Review*, vol. 77, no. 2, p. 297, 1950.

[66] E. L. Hahn, "Spin echoes," *Physical Review*, vol. 80, no. 4, p. 580, 1950.

[67] P. A. Bottomley, "Spatial localization in nmr spectroscopy in vivo," *Annals of the New York Academy of Sciences*, vol. 508, no. 1, pp. 333–348, 1987.

[68] J. Frahm, K.-D. Merboldt, and W. Hänicke, "Localized proton spectroscopy using stimulated echoes," *Journal of Magnetic Resonance*, vol. 72, no. 3, pp. 502–508, 1987.

[69] P. A. Bottomley and J. R. Griffiths, *Handbook of magnetic resonance spectroscopy in vivo: MRS theory, practice and applications*. John Wiley & Sons, 2016.

[70] P. C. Lauterbur, "Image formation by induced local interactions: examples employing nuclear magnetic resonance," *Nature*, vol. 242, no. 5394, pp. 190–191, 1973.

[71] P. Mansfield, "Multi-planar image formation using nmr spin echoes," *Journal of Physics C: Solid State Physics*, vol. 10, no. 3, pp. 55–58, 1977.

[72] J. Hennig, A. Nauerth, and H. Friedburg, "Rare imaging: a fast imaging method for clinical mr," *Magnetic Resonance in Medicine*, vol. 3, no. 6, pp. 823–833, 1986.

[73] M. T. Vlaardingerbroek and J. A. Boer, *Magnetic resonance imaging: theory and practice*. Springer Science & Business Media, 2013.

[74] R. Hurwitz, S. R. Lane, R. Bell, and M. Brant-Zawadzki, "Acoustic analysis of gradient-coil noise in mr imaging.," *Radiology*, vol. 173, no. 2, pp. 545–548, 1989.

[75] D.-M. Koh and D. J. Collins, "Diffusion-weighted mri in the body: applications and challenges in oncology," *American Journal of Roentgenology*, vol. 188, no. 6, pp. 1622–1635, 2007.

[76] S. E. Maier, Y. Sun, and R. V. Mulkern, "Diffusion imaging of brain tumors," *NMR in Biomedicine*, vol. 23, no. 7, pp. 849–864, 2010.

[77] H. Johansen-Berg and T. E. Behrens, *Diffusion MRI: from quantitative measurement to in vivo neuroanatomy*. Academic Press, 2013.

[78] A. Fick, "Ueber diffusion," *Annalen der Physik*, vol. 170, no. 1, pp. 59–86, 1855.

[79] A. Einstein, "Über die von der molekularkinetischen theorie der wärme geforderte bewegung von in ruhenden flüssigkeiten suspendierten teilchen," *Annalen der physik*, vol. 4, 1905.

[80] E. O. Stejskal and J. E. Tanner, "Spin diffusion measurements: spin echoes in the presence of a time-dependent field gradient," *The journal of Chemical Physics*, vol. 42, no. 1, pp. 288–292, 1965.

[81] O. P. Simonetti, R. E. Wendt III, and J. L. Duerk, "Significance of the point of expansion in interpretation of gradient moments and motion sensitivity," *Journal of Magnetic Resonance Imaging*, vol. 1, no. 5, pp. 569–577, 1991.

[82] J. E. Tanner, "Use of the stimulated echo in nmr diffusion studies," *The Journal of Chemical Physics*, vol. 52, no. 5, pp. 2523–2526, 1970.

[83] B. Gross and R. Kosfeld, "Application of spin-echo method in measurement of auto-diffusion," *Messtechnik*, vol. 77, no. 7-8, p. 171, 1969.

[84] D. Le Bihan and E. Breton, "In vivo magnetic resonance imaging of diffusion," *Comptes Rendus des Seances de l'Academie des Sciences. Serie 2*, vol. 301, no. 15, pp. 1109–1112, 1985.

[85] D. Le Bihan, E. Breton, D. Lallemand, P. Grenier, E. Cabanis, and M. Laval-Jeantet, "Mr imaging of intravoxel incoherent motions: application to diffusion and perfusion in neurologic disorders.," *Radiology*, vol. 161, no. 2, pp. 401–407, 1986.

[86] J. Mattiello, P. J. Basser, and D. LeBihan, "Analytical expressions for the b matrix in nmr diffusion imaging and spectroscopy," *Journal of Magnetic Resonance, Series A*, vol. 108, no. 2, pp. 131–141, 1994.

[87] O. Dietrich, A. Biffar, A. Baur-Melnyk, and M. F. Reiser, "Technical aspects of mr diffusion imaging of the body," *European Journal of Radiology*, vol. 76, no. 3, pp. 314–322, 2010.

[88] D. K. Jones, *Diffusion mri*. Oxford University Press, 2010.

[89] S. Brockstedt, J. R. Moore, C. Thomsen, S. Holtås, and F. Ståhlberg, "High-resolution diffusion imaging using phase-corrected segmented echo-planar imaging," *Magnetic Resonance Imaging*, vol. 18, no. 6, pp. 649–657, 2000.

[90] S. Meiboom and D. Gill, "Modified spin-echo method for measuring nuclear relaxation times," *Review of Scientific Instruments*, vol. 29, no. 8, pp. 688–691, 1958.

[91] D. C. Alsop, "Phase insensitive preparation of single-shot rare: application to diffusion imaging in humans," *Magnetic Resonance in Medicine*, vol. 38, no. 4, pp. 527–533, 1997.

[92] B. Cervantes, A. T. Van, D. Weidlich, H. Kooijman, A. Hock, E. J. Rummeny, A. Gersing, J. S. Kirschke, and D. C. Karampinos, "Isotropic resolution diffusion tensor imaging of lumbosacral and sciatic nerves using a phase-corrected diffusion-prepared 3d turbo spin echo," *Magnetic Resonance in Medicine*, vol. 80, no. 2, pp. 609–618, 2018.

[93] I. Ronen and J. Valette, "Diffusion-weighted magnetic resonance spectroscopy," *EMagRes*, pp. 733–750, 2007.

[94] S. Ruschke, H. Kienberger, T. Baum, H. Kooijman, M. Settles, A. Haase, M. Rychlik, E. J. Rummeny, and D. C. Karampinos, "Diffusion-weighted stimulated echo acquisition mode (dw-steam) mr spectroscopy to measure fat unsaturation in regions with low proton-density fat fraction," *Magnetic Resonance in Medicine*, vol. 75, no. 1, pp. 32–41, 2016.

[95] C. Ahn and Z. Cho, "Analysis of the eddy-current induced artifacts and the temporal compensation in nuclear magnetic resonance imaging," *IEEE transactions on Medical Imaging*, vol. 10, no. 1, pp. 47–52, 1991.

[96] Y. Shen, D. J. Larkman, S. Counsell, I. M. Pu, D. Edwards, and J. V. Hajnal, "Correction of high-order eddy current induced geometric distortion in diffusion-weighted echo-planar images," *Magnetic Resonance in Medicine*, vol. 52, no. 5, pp. 1184–1189, 2004.

[97] A. T. Van, B. Cervantes, H. Kooijman, and D. C. Karampinos, "Analysis of phase error effects in multishot diffusion-prepared turbo spin echo imaging," *Quantitative imaging in Medicine and Surgery*, vol. 7, no. 2, p. 238, 2017.

[98] D. Malyarenko, C. J. Galbán, F. J. Londy, C. R. Meyer, T. D. Johnson, A. Rehemtulla, B. D. Ross, and T. L. Chenevert, "Multi-system repeatability and reproducibility of apparent diffusion coefficient measurement using an ice-water phantom," *Journal of Magnetic Resonance Imaging*, vol. 37, no. 5, pp. 1238–1246, 2013.

[99] D. I. Malyarenko, D. Newitt, L. J. Wilmes, A. Tudorica, K. G. Helmer, L. R. Arlinghaus, M. A. Jacobs, G. Jajamovich, B. Taouli, T. E. Yankeelov, W. Huang, and T. L. Chenevert, "Demonstration of nonlinearity bias in the measurement of the apparent diffusion coefficient in multicenter trials," *Magnetic Resonance in Medicine*, vol. 75, no. 3, pp. 1312–1323, 2016.

[100] D. I. Malyarenko and T. L. Chenevert, "Practical estimate of gradient nonlinearity for implementation of apparent diffusion coefficient bias correction," *Journal of Magnetic Resonance Imaging*, vol. 40, no. 6, pp. 1487–1495, 2014.

[101] P. T. Callaghan, *Principles of nuclear magnetic resonance microscopy*. Oxford University Press on Demand, 1993.

[102] D. G. Norris, "Implications of bulk motion for diffusion-weighted imaging experiments: effects, mechanisms, and solutions," *Journal of Magnetic Resonance Imaging*, vol. 13, no. 4, pp. 486–495, 2001.

[103] Y. Zur, E. Bosak, and N. Kaplan, "A new diffusion ssfp imaging technique," *Magnetic Resonance in Medicine*, vol. 37, no. 5, pp. 716–722, 1997.

[104] E. M. Haacke and G. W. Lenz, "Improving mr image quality in the presence of motion by using rephasing gradients," *American Journal of Roentgenology*, vol. 148, no. 6, pp. 1251–1258, 1987.

[105] S. Brockstedt, M. Borg, B. Geijer, R. Wirestam, C. Thomsen, S. Holtås, and F. Ståhlberg, "Triggering in quantitative diffusion imaging with single-shot epi," *Acta Radiologica*, vol. 40, no. 3, pp. 263–269, 1999.

[106] J. Hiltunen, R. Hari, V. Jousmäki, K. Müller, R. Sepponen, and R. Joensuu, "Quantification of mechanical vibration during diffusion tensor imaging at 3 t," *Neuroimage*, vol. 32, no. 1, pp. 93–103, 2006.

[107] D. Gallichan, M. D. Robson, A. Bartsch, and K. L. Miller, "Tremr: Table-resonance elastography with mr," *Magnetic Resonance in Medicine*, vol. 62, no. 3, pp. 815–821, 2009.

[108] D. Gallichan, J. Scholz, A. Bartsch, T. E. Behrens, M. D. Robson, and K. L. Miller, "Addressing a systematic vibration artifact in diffusion-weighted mri," *Human Brain Mapping*, vol. 31, no. 2, pp. 193–202, 2010.

[109] M. M. Berl, L. Walker, P. Modi, M. O. Irfanoglu, J. E. Sarlls, A. Nayak, and C. Pierpaoli, "Investigation of vibration-induced artifact in clinical diffusion-weighted imaging of pediatric subjects," *Human Brain Mapping*, vol. 36, no. 12, pp. 4745–4757, 2015.

[110] J. Tanner, "Self diffusion of water in frog muscle," *Biophysical Journal*, vol. 28, no. 1, pp. 107–116, 1979.

[111] P. P. Mitra, P. N. Sen, and L. M. Schwartz, "Short-time behavior of the diffusion coefficient as a geometrical probe of porous media," *Physical Review B*, vol. 47, no. 14, p. 8565, 1993.

[112] D. S. Novikov, J. H. Jensen, J. A. Helpern, and E. Fieremans, "Revealing mesoscopic structural universality with diffusion," *Proceedings of the National Academy of Sciences*, vol. 111, no. 14, pp. 5088–5093, 2014.

[113] D. E. Woessner, "Nmr spin-echo self-diffusion measurements on fluids undergoing restricted diffusion," *The Journal of Physical Chemistry*, vol. 67, no. 6, pp. 1365–1367, 1963.

[114] J. Murday and R. M. Cotts, "Self-diffusion coefficient of liquid lithium," *The Journal of Chemical Physics*, vol. 48, no. 11, pp. 4938–4945, 1968.

[115] C. Neuman, "Spin echo of spins diffusing in a bounded medium," *The Journal of Chemical Physics*, vol. 60, no. 11, pp. 4508–4511, 1974.

[116] E. Fordham, S. Gibbs, and L. Hall, "Partially restricted diffusion in a permeable sandstone: observations by stimulated echo pfg nmr," *Magnetic Resonance Imaging*, vol. 12, no. 2, pp. 279–284, 1994.

[117] M. Hurlimann, K. G. Helmer, L. Latour, and C. H. Sotak, "Restricted diffusion in sedimentary rocks. determination of surface-area-to-volume ratio and surface relaxivity," *Journal of Magnetic Resonance, Series A*, vol. 111, no. 2, pp. 169–178, 1994.

[118] L. L. Latour, P. P. Mitra, R. L. Kleinberg, and C. H. Sotak, "Time-dependent diffusion coefficient of fluids in porous media as a probe of surface-to-volume ratio," *Journal of Magnetic Resonance. Series A (Print)*, vol. 101, no. 3, pp. 342–346, 1993.

[119] D. S. Novikov and V. G. Kiselev, "Surface-to-volume ratio with oscillating gradients," *Journal of Magnetic Resonance*, vol. 210, no. 1, pp. 141–145, 2011.

[120] S. Portnoy, J. Flint, S. Blackband, and G. Stanisz, "Oscillating and pulsed gradient diffusion magnetic resonance microscopy over an extended b-value range: implications for the characterization of tissue microstructure," *Magnetic Resonance in Medicine*, vol. 69, no. 4, pp. 1131–1145, 2013.

[121] E. C. Parsons Jr, M. D. Does, and J. C. Gore, "Temporal diffusion spectroscopy: theory and implementation in restricted systems using oscillating gradients," *Magnetic Resonance in Medicine*, vol. 55, no. 1, pp. 75–84, 2006.

[122] T. Garasanin, T. Cosgrove, L. Marteaux, A. Kretschmer, A. Goodwin, and K. Zick, "Nmr self-diffusion studies on pdms oil-in-water emulsion," *Langmuir*, vol. 18, no. 26, pp. 10298–10304, 2002.

[123] U. Ferizi, T. Schneider, T. Witzel, L. L. Wald, H. Zhang, C. A. Wheeler-Kingshott, and D. C. Alexander, "White matter compartment models for in vivo diffusion mri at 300 mt/m," *NeuroImage*, vol. 118, pp. 468–483, 2015.

[124] D. C. Alexander, T. B. Dyrby, M. Nilsson, and H. Zhang, "Imaging brain microstructure with diffusion mri: practicality and applications," *NMR in Biomedicine*, vol. 32, no. 4, p. e3841, 2019.

[125] G. Hamilton, D. L. Smith Jr, M. Bydder, K. S. Nayak, and H. H. Hu, "Mr properties of brown and white adipose tissues," *Journal of Magnetic Resonance Imaging*, vol. 34, no. 2, pp. 468–473, 2011.

[126] A. Lehnert, J. Machann, G. Helms, C. D. Claussen, and F. Schick, "Diffusion characteristics of large molecules assessed by proton mrs on a whole-body mr system," *Magnetic Resonance Imaging*, vol. 22, no. 1, pp. 39–46, 2004.

[127] D. Weidlich, J. Honecker, O. Gmach, M. Wu, R. Burgkart, S. Ruschke, D. Franz, B. H. Menze, T. Skurk, H. Hauner, U. Kulozik, and D. C. Karampinos, "Measuring large lipid droplet sizes by probing restricted lipid diffusion effects with diffusion-weighted mrs at 3t," *Magnetic Resonance in Medicine*, vol. 81, no. 6, pp. 3427–3439, 2019.

[128] D. Weidlich, M. Zamskiy, M. Maeder, S. Ruschke, S. Marburg, and D. C. Karampinos, "Reduction of vibration-induced signal loss by matching mechanical vibrational states: Application in high b-value diffusion-weighted mrs," *Magnetic Resonance in Medicine*, vol. 84, no. 1, pp. 39–51, 2020.

[129] D. Weidlich, J. Honecker, C. Boehm, S. Ruschke, D. Junker, A. T. Van, M. R. Makowski, C. Holzapfel, M. Claussnitzer, H. Hauner, and D. C. Karampinos, "Lipid droplet–size mapping in human adipose tissue using a clinical 3t system," *Magnetic Resonance in Medicine*, vol. 86, pp. 1256–1270, 2021.

[130] P. Callaghan, K. Jolley, and R. Humphrey, "Diffusion of fat and water in cheese as studied by pulsed field gradient nuclear magnetic resonance," *Journal of Colloid and interface Science*, vol. 93, no. 2, pp. 521–529, 1983.

[131] H. Lahrech, S. Zoula, R. Farion, C. Rémy, and M. Décorps, "In vivo measurement of the size of lipid droplets in an intracerebral glioma in the rat," *Magnetic Resonance in Medicine*, vol. 45, no. 3, pp. 409–414, 2001.

[132] V. Brandejsky, R. Kreis, and C. Boesch, "Restricted or severely hindered diffusion of intramyocellular lipids in human skeletal muscle shown by in vivo proton mr spectroscopy," *Magnetic Resonance in Medicine*, vol. 67, no. 2, pp. 310–316, 2012.

[133] R. A. Hedeen and W. A. Edelstein, "Characterization and prediction of gradient acoustic noise in mr imagers," *Magnetic Resonance in Medicine*, vol. 37, no. 1, pp. 7–10, 1997.

[134] D. G. Tomasi and T. Ernst, "Echo planar imaging at 4 tesla with minimum acoustic noise," *Journal of Magnetic Resonance Imaging*, vol. 18, no. 1, pp. 128–130, 2003.

[135] A. Ogura, F. Maeda, A. Miyai, K. Hayashi, and T. Hongoh, "Effect of vibration caused by time-varying magnetic fields on diffusion-weighted mri," *Nihon Hoshasen Gijutsu Gakkai zasshi*, vol. 62, no. 4, pp. 565–569, 2006.

[136] S. Mohammadi, Z. Nagy, C. Hutton, O. Josephs, and N. Weiskopf, "Correction of vibration artifacts in dti using phase-encoding reversal (coviper)," *Magnetic Resonance in Medicine*, vol. 68, no. 3, pp. 882–889, 2012.

[137] Y. Assaf and O. Pasternak, "Diffusion tensor imaging (dti)-based white matter mapping in brain research: a review," *Journal of Molecular Neuroscience*, vol. 34, no. 1, pp. 51–61, 2008.

[138] S. Mori and P. C. Van Zijl, "Fiber tracking: principles and strategies–a technical review," *NMR in Biomedicine*, vol. 15, no. 7-8, pp. 468–480, 2002.

[139] B. Jeurissen, M. Descoteaux, S. Mori, and A. Leemans, "Diffusion mri fiber tractography of the brain," *NMR in Biomedicine*, vol. 32, no. 4, p. e3785, 2019.

[140] Y. Assaf, H. Johansen-Berg, and M. Thiebaut de Schotten, "The role of diffusion mri in neuroscience," *NMR in Biomedicine*, vol. 32, no. 4, p. e3762, 2019.

[141] N. Ohno, H. Kan, T. Miyati, T. Aoki, S. Ishida, and T. Gabata, "Water and lipid diffusion mri using chemical shift displacement-based separation of lipid tissue (split)," *Magnetic Resonance Imaging*, vol. 39, pp. 144–148, 2017.

[142] C. Cui, A. Shah, X. Wu, and M. Jacob, "A rapid 3d fat–water decomposition method using globally optimal surface estimation (r-goose)," *Magnetic Resonance in Medicine*, vol. 79, no. 4, pp. 2401–2407, 2018.

[143] C. Boehm, M. N. Diefenbach, M. R. Makowski, and D. C. Karampinos, "Improved body quantitative susceptibility mapping by using a variable-layer single-min-cut graph-cut for field-mapping," *Magnetic Resonance in Medicine*, vol. 85, pp. 1697–1712, 2020.

[144] A. Shah, M. D. Abámoff, and X. Wu, "Optimal surface segmentation with convex priors in irregularly sampled space," *Medical Image Analysis*, vol. 54, pp. 63–75, 2019.

[145] C. A. Clark, T. R. Barrick, M. M. Murphy, and B. A. Bell, "White matter fiber tracking in patients with space-occupying lesions of the brain: a new technique for neurosurgical planning?," *Neuroimage*, vol. 20, no. 3, pp. 1601–1608, 2003.

[146] K. Setsompop, R. Kimmlingen, E. Eberlein, T. Witzel, J. Cohen-Adad, J. A. McNab, B. Keil, M. D. Tisdall, P. Hoecht, P. Dietz, S. F. Cauley, V. Tountcheva, V. Matschl, V. H. Lenz, K. Heberlein, A. Potthast, H. Thein, J. Van Horn, A. Toga, F. Schmitt, D. Lehne, B. R. Rosen, V. Wedeen, and L. L. Wald, "Pushing the limits of in vivo diffusion mri for the human connectome project," *Neuroimage*, vol. 80, pp. 220–233, 2013.